New Astronomy 105 (2024) 102099

Contents lists available at ScienceDirect

New Astronomy

journal homepage: www.elsevier.com/locate/newast

The two roles of the SPH Kernel and dissipation on accretion disc modelling in semi-detached Low-Mass Close Binaries

G. Lanzafame

INAF Osservatorio Astrofisico di Catania, Via S. Sofia 78, Catania, 95123, Italy

ARTICLE INFO

MSC:
85-08:85A30

Keywords:
Accretion
Accretion discs
Stars: Binaries: Close
Physical data and processes: Hydrodynamics
Methods: Numerical
N-body simulations

ABSTRACT

This study addresses two aspects of the SPH technique. The first aspect regards the 3D (2D) numerical integration. The second aspect deals with the necessary damping for handling inviscid flow discontinuities. Accretion discs in Low-Mass Close Binaries (LMCBs) are a context pushing the limit of SPH codes since turbulence, shocks, and shear flows coexist. Thus, an LMCB with high mass-transfer from the inner Lagrangian point is considered. This choice is made for an in-depth understanding of the numerical and physical aspects related to pressure forces computed through SPH Kernel spatial gradients in high-speed collisional flows. In this regard, gas compressibility also plays a role. Firstly, we pay attention to the algebraic term $4\pi r^2$ coming from the cubic differential d^3r and affecting any 3D SPH integration. This is made through a comparison of physically inviscid SPH structures referring to the same LMCB and mass-transfer conditions. Then, a reformulation of the non-viscous damping is also considered by adopting a Lagrangian-free physical formulation. Inviscid accretion discs should develop a steady toroidal structure because radial transport mechanisms should be excluded by missing any radial shear flow damping. Therefore, thinner discs, also including a steady toroidal ring, identify that SPH inviscid modelling free of any incorrect pressure gradient excess among thick disc structures. This task is simplified since initial conditions deliberately favour thick discs. The physically viscous hydrodynamics of the disc is also addressed by adopting a Prandtl-like turbulent kinematic viscosity coefficient in the Navier–Stokes equations, distinguishing the roles of the bulk and shear viscosities.

1. Introduction

The Smooth Particle Hydrodynamics (SPH) framework is a well-known Free Lagrangian numerical technique adopted in the computational fluid dynamics (CFD) since the 2nd half of the 70s (Gingold and Monaghan, 1977, 1978, 1979a,b, 1980, 1981, 1982b, 1983; Wood, 1981, 1982; Lattanzio et al., 1985; Monaghan, 1985, 1992; Monaghan and Gingold, 1983; Monaghan and Lattanzio, 1985; Whitehurst, 1995).

In the original idea of Lucy (1977), the physical properties of interacting and overlapping Lagrangian fluid volumes are computed by interpolation integrals over a spatial domain within an assigned spatial Kernel in the CFD equations.

Various investigations have been carried out on how SPH fluid dynamics and flow structures behave according to the analytic formulation of the smooth radial profile of the interpolation Kernel (Gingold and Monaghan, 1982b; Fulk and Quinn, 1996; Liu et al., 2003; Omang et al., 2005; Busegnies et al., 2007; Cabezón et al., 2008, 2017; Lanzafame, 2010a, 2018; Dehnen and Aly, 2012; Valizadeh and Monaghan, 2015; Frontiere et al., 2017). Moreover, another fundamental aspect is how the dissipation is introduced in the SPH non-viscous CFD. Regarding this second topic, some papers deal with the non-viscous flow dynamics according to aspects related to different analytical expressions on the mathematical artificial dissipation (Balsara, 1995; Monaghan, 1997; Morris and Monaghan, 1997; Lanzafame, 2010b; Read and Hayfield, 2012; Taddei et al., 2017). Instead, some SPH codes have been written by using some Godunov schemes, specifically developed for better solving the Riemann problem in the CFD (Parshikov, 1999; Parshikov et al., 2000; Parshikov and Medin, 2002; Inutsuka, 2002; Imaeda and Inutsuka, 2002; Cha and Whitworth, 2003; Cha and Wood, 2016; Molteni and Bilello, 2003; Iwasaki and Inutsuka, 2011; Sugiura and Inutsuka, 2017). In other papers, even the simpler numerical dissipation, due to numerical truncation errors, has also been taken into account (Sawada et al., 1987; Deng et al., 2017). In this regard, even the larger numerical dissipation involved in implicit integration techniques also plays a role (Lanzafame, 2013).

This paper deals with both topics, for an in-depth understanding both of the 2D and 3D SPH numerical integrations and of the role of damping in the Euler equations context. The distinction of the inviscid damping with a strictly physical dissipation in the Navier–Stokes equations context is the second relevant topic also considered in this work. To this end, a comparative study is carried out by exploiting

E-mail address: Giuseppe.Lanzafame@inaf.it.

https://doi.org/10.1016/j.newast.2023.102099
Received 14 January 2023; Received in revised form 16 June 2023; Accepted 10 July 2023
Available online 14 July 2023

the accretion disc modelling in the semi-detached Low-Mass Close Binaries (LMCBs), whose primary white dwarf star is the only compact star and where the mass-transfer flows through the inner Lagrangian point L_1. An assigned arbitrary value to the specific heat ratio $\gamma = c_p c_V^{-1}$ is assumed for each gas dynamics modelling and results are also considered in the light of three different gas compressibilities. This study can be done because the disc structure and dynamics are features strictly imposed by the stellar masses and their mutual spatial radial separation within the primary star potential well.

However, any excessively dominant gravitational field hides any peculiarity coming from any inadequacy of the radial Kernel profiles, whatever is the gas compressibility. For this reason, a low-mass primary star is a much more appropriate choice, as long as the secondary star is a main sequence or a subgiant star. In the case of a close binary of two compact stars, pressure gradients could regain relevance only if the mass-transfer conditions justify perceptible thermal and kinetic energies against the gravitational energy at such very short radial distances.

Accretion discs fluid dynamics in an LMCB hardly stresses out the efficiency of SPH codes since turbulence, shocks, and shear flows coexist together with free-edge flows. Any correct inviscid accretion disc structure should include a steady toroidal ring set up by the initial kinematic conditions as it is described in Lubow and Shu (1975) where it is explicitly written: "*The velocity component of the incident stream resolved in the tangential direction of the simple periodic orbit at the point of their intersection must equal the speed of the simple periodic orbit at that point*". The higher the angular momentum at L_1, the greater the mean radius of the steady toroidal ring. The steady presence of such a peculiarity is also explicitly highlighted in some papers (Churazov et al., 2001; Díaz Trigo et al., 2006; Galis, 2007; Inoue, 2022) arguing the presence of a torus, an envelope or a mix of them in disc structures. However, any shear damping limits the development of steady toroidal structures, leading to disc structures through the activation of radial transport mechanisms.

The higher the mass-transfer rate, as well as the lower the gas compressibility, the thicker the accretion disc. Thus, low stellar masses and a high speed of mass-transfer are deliberately chosen because they better highlight the defects in the Kernel radial profile through high-speed flow collisions. Even the comparison of flow structures and dynamics through the adoption of different assigned gas compressibilities is useful for understanding the role of pressure forces strictly related to the spatial gradients of the Kernel radial profile. Thanks to such conditions, the thinner accretion discs, also including a steady toroidal structure, identify the SPH non-viscous modelling free of pressure force excesses at the assigned gas compressibility. In this regard, searching for the thinnest structure among 3D thick disc models is much easier than doing the same by trying to compare thin disc structures.

Usually, studies about the efficiency of interpolation Kernels are performed through numerical tests on 1D flow discontinuities or on 2D shear flows. In doing so, numerical solutions are compared with the analytical ones, calibrating several free parameters. On very short time intervals, these tests provide results in which all adopted Kernels are almost effective. Hence, it is also interesting to understand how SPH modelling works for far longer evolutionary times.

The entire disc evolution is spatially confined within a 3D environment. This makes it easier to check the efficiency of numerical codes for long evolutionary times. Instead, any 3D evolution of a progressive flow discontinuity implies the adoption of very large fluid spatial arrays involving greater computer resources and significant efforts for handling the boundary conditions. Moreover, the results of 2D or 3D numerical simulations do not always have a direct comparison with analytical solutions. In some cases a comparison is possible if self-similarity solutions exist, like the Sedov-Von Neumann–Taylor ones for inviscid blast waves (Sedov, 1946; Zel'dovich and Raizer, 1966), showing how even geometric aspects affect the analytical solutions. In other cases, only approximate solutions exist (Zel'dovich and Raizer, 1966) as long as any turbulence is excluded.

The comparison among Lagrangian-SPH-based codes with Eulerian grid-based ones is another intriguing topic in astrophysics as well as in cosmology. Whenever the comparison mainly concerns computational performances, an SPH N-body parallel version is often considered as in Fortin et al. (2011), where it is shown that both performances well compare with each other. Instead, whenever the comparison concerns the numerical solutions themselves, a discrepancy in conclusions is reported. In some cases (Vazza et al., 2011), consistent thermodynamic and kinematic differences are obtained in the more diluted fluid regions, while in other cases (Motl et al., 2017; Cabezón et al., 2018) the flow structures and dynamics compare with each other within 10 - 20%. In this regard, about the merger of degenerate binaries by mass-transfer from L_1, Motl et al. (2017) report one remarkable difference: SPH models yield higher mass-transfer rates and a consequent disc faster radial transport, despite the efforts to reproduce the same initial boundary conditions. However, an in-depth consideration is necessary. Such results highlight a problem since SPH and Eulerian grid-based disc structures compare with each other at the same mass-transfer rate, despite a higher SPH accretion rate. So, disc thicknesses also compare with each other, despite the SPH larger mass radial transport should imply thinner discs. Thus, free of any consideration about the flow damping, any incorrect excess of SPH pressure forces explains both the higher disc mass radial transport and the reduction of discrepancy in the disc thickness between SPH and Eulerian-grid models.

In this work, for the sake of simplicity, mathematical or physical proofs are postponed in dedicated Appendices. This choice makes the smooth reading of the article by non-specialists of the numerical technique here discussed. The Appendices, however, bring together the research of three previous publications (Lanzafame, 2010a,b, 2015), deepening essential aspects important for the in-depth understanding of this work. The body of the paper deals with the description and with the criticalities of the assumed initial and boundary conditions on the SPH accretion disc modelling, and with the comparison of disc models. It is also explained why, at the same gas compressibility, the thinner disc structures highlight the best 3D SPH modelling of accretion discs in the non-viscous ideal flow dynamics, as preliminarily highlighted in Lanzafame (2010a,b).

Disc modelling structures for different γ-values are compared to each other, also discussing their dynamics and thermodynamics as for the non-viscous Euler equations frame. Moreover, a non-viscous damping physically implemented within the Equation of State (EoS) (Lanzafame, 2010b) is also considered to obtain a non-viscous perfect gas steady toroidal ring within the gravitational potential well. The comparison of disc structures in the XSPH variant (Monaghan, 1992) is also shown in some cases in order to understand if some improvements occur. The whole disc modelling is also expanded in the Navier–Stokes physically viscous CFD in the light of Lanzafame (2015) results based on a formulation of the kinematic viscosity coefficient comparable to that of Prandtl (1925). Numerical and physical aspects are highlighted by distinguishing one from the other in the final conclusions.

2. Model parameters: initial and boundary conditions

The masses of the two companion stars and their spatial radial separation set the main features of the semi-detached binary. In such a model we set a primary compact white dwarf star mass M_1 and a secondary main sequence low-mass star mass M_2 of $1 M_\odot$ each, whilst their mutual radial distance $d_{12} = 10^6$ km. d_{12} is assumed as the normalization reference length $r_\circ$ to which all lengths refer. Hence, $d_{12} = 1$ in reality means $d_{12} r_\circ^{-1} = 1$, omitting $r_\circ$ for the sake of simplicity. Only the secondary star fills its Roche lobe. The mass-transfer flow velocity, around the inner Lagrangian point L_1, is set to $v_{inj} = 1.3\ 10^2$ km s^{-1}, while its local mass density and its local temperature are set as $\rho_{inj} = 10^{-14}$ g cm^{-3} and $T_{inj} = 10^4$ K. Such

ρ_{inj} and T_{inj} values correspond to mean values of ρ and T in solar-like star atmospheres (Priest, 1984; Stix, 1989), despite in reality they are unknown parameters at L_1.

The reference frame is centred on the primary compact star, whose rotational period, normalized to 2π in dimensionless units, corresponds to the orbital period of the binary system. Therefore, the gravitational force must also include the Coriolis and the centrifugal contributions. Any fluid autogravitation is neglected being the disc mass orders of magnitude smaller compared to the primary star mass in such astrophysical objects. This justifies why any primary mass increase, as well as any secondary mass decrease, are negligible for evolutionary times of the order of several orbital periods, being each orbital period of the order of ~5–10 h. Any reference frame on the centre of mass of the binary implies no centrifugal and Coriolis accelerations, at the cost of more complicated handling of the rotational kinematics of the primary's Roche lobe.

Supersonic kinematic conditions at L_1 are discussed in Lanzafame (2008, 2009) and Lanzafame et al. (2006), especially when active phases of LMCBs are considered. The assumed supersonic initial mass-transfer velocity v_{inj} could be even one order of magnitude smaller (Molteni et al., 1991; Lanzafame et al., 1992; Bisikalo et al., 2000; Boyarchuk et al., 2002). However, we aim to bring out the disc features allowing us to make significant choices from high-speed hard particle collisions both on the SPH integrations and on the flow damping mechanism. The initial velocity setting is however fully justified since the mass-density of the secondary star photosphere $\rho_2 \sim 10^{-9}$–10^{-6} g cm^{-3} while its gas velocity $v_2 \sim 10^{-2}$–1 km s^{-1} within the Roche lobe of the secondary normal or subgiant star, close to the L_1 point. These are typical values of a stellar photosphere in a macroturbulence regime of intermediate - low-mass stars (Priest, 1984; Stix, 1989). Hence, as a rough evaluation, $v_{inj} \sim v_2\rho_2\rho_1^{-1} = v_2\rho_2\rho_{inj}^{-1}$ (being $\rho_1 = \rho_{inj}$) within the compact primary's Roche lobe around L_1, considering the momentum conservation of an isothermal flow, free of any external force field. However, the mass-density ρ_1 around the L_1 point towards the compact primary's potential well is a real unknown. It could be of the order of $\rho_\circ$, but it could be even much larger. This result is also obtained (Lubow and Shu, 1975) either considering the restricted problem of three bodies in terms of the Jacobi constant or according to the Bernoulli's theorem being $v^2/2 + \Phi + \epsilon \log \rho = const$ along the same streamline, where ϵ is the thermal energy per unit mass and Φ is the gravitational field potential.

The assumed initial value T_{inj} of the mass-transfer flow temperature is a bit larger than the corresponding photospheric value for a solar mass main sequence star or a subgiant star of equal mass. This choice also takes into account the radiative heating of the secondary's photospheric surface due to the X-ray emission coming from the accretion disc. Instead, the choice of ρ_{inj}, being arbitrary, needs to be smaller than the mass-density on the photospheric surface of the secondary star ρ_2 by some orders of magnitude.

The assumed stellar masses and the initial kinematic and thermal conditions at L_1, involve a negative total energy per unit mass throughout around L_1 within the primary's gravitational potential well. In principle, this should ensure the development of consistent flow structures within the primary's gravitational potential well, well-bound, or not according to the chosen specific heat ratio γ.

As far as the geometric initial mass-transfer conditions are concerned, the compact primary's potential well is set initially empty and SPH particles are generated in assigned initial positions within a small conic volume. The vertex of the injection cone corresponds to the inner Lagrangian point L_1 position while its arbitrary spreading and height (length in $r_\circ$ units) are respectively of the order of 1 radiant and $3\ 10^{-2}$ throughout the accretion disc modelling. The assumed initial SPH spatial resolution length is set either as $h = 5\ 10^{-3}$ or as $h = 10^{-2}$ (in $r_\circ$ units), according to the integration–interpolation Kernel choice. Whenever a spatial variability of h is considered, the adaptive h values are recalculated for each particle from its native position. New atomic hydrogen SPH particles are created within such conical injection volume whenever their initial assigned native position is free from other neighbour particles around, within a sensitive creation domain whose radial extension corresponds to $5\ 10^{-3}$. This setting ensures the generation of a stream of injected particles as flowing from L_1, free of any significant flow discontinuity and mass-transfer rate fluctuations because of the flow kinematics controlled by the primary's gravitational field. Fluctuations dictated by the gas compressibility always exist, but they create greater flow discrepancies in the case of subsonic injection conditions in a gravitational field weak compared to pressure forces, which is a context very far from that we refer to.

Subsonic flows are usually more problematic to SPH concerning instabilities and mixing. Meaning that they usually serve better to make decisions regarding SPH implementations. However, the context of an accretion disc is different. The supersonic kinematic field is strictly imposed by the primary star gravitation whatever the kinematics of the mass-transfer flow, as long as the mass-transfer thermal conditions do not compromise any disc structure. This last peculiarity, also strongly affected by the assumed gas compressibility, is excluded for LMCBs like that here considered, since sonic and supersonic mass-transfer conditions are always considered (Molteni et al., 1991; Lanzafame et al., 1992; Meglicki et al., 1993; Murray, 1996; Bisikalo et al., 2000; Boyarchuk et al., 2002; Lanzafame et al., 2006; Lanzafame, 2008, 2009).

Intermediate spatial resolutions, where $h^{-1} \approx 10^2$–$2\ 10^2$, are a good compromise between a smaller h, involving a higher spatial resolution at the price of longer computational times, and a larger h leading to a physically meaningless low resolution. In the first case, the longer computational time is a numerical consequence of the explicit Friedrichs–Courant–Lewy condition (Courant et al., 1928; Monaghan, 1992) evaluating the explicit computational time-step. Moreover, each evolutionary step implies an integration–interpolation for each particle, each involving its neighbours. Free of any consideration on the flow kinematics and thermodynamics considered within the Friedrichs–Courant–Lewy condition, the larger are the particle total number N and the statistical mean of neighbours $\bar{n}_p$, the longer is the computational time. Hence, any model working with smaller h, involving a greater N, leads anyway to longer computational times in so far as $\bar{n}_p$ is statistically unchanged.

If variable smoothing length SPH techniques are considered, the number of neighbours directly affects the overall amplitude of the integration-interpolation domain. This strictly happens whenever the adaptive SPH (ASPH) technique is formulated by assuming an assigned number of neighbours. In this regard, a conflict comes out since the thin thickness at the disc's inner edge, together with its low density in a free fall accretion kinematics, make any excessive widening of h inadequate on the basis of too many neighbours. Hence, it is necessary to limit the desired number of neighbours avoiding high h values in order to resolve the disc thickness at the low density disc's inner edge. However, working with a great number of neighbours is the current numerical path to approximate the continuum limit. Therefore, a compromise is needed to get an acceptable number of neighbours, having at the same time a satisfactory spatial resolution at the disc's inner edge. Therefore, a number of 40 neighbours is assigned whenever ASPH disc models are considered. Such a number, largely used until a decade ago, is considered low today, compared to other astrophysical ASPH simulations.

Working with dimensionless physical quantities for both Euler and Navier–Stokes fluid dynamics equations, the following normalization factors are adopted: $M_\circ = M_1 + M_2$ for the masses, $r_\circ$ for the lengths, $v_\circ = [GM_\circ r_\circ^{-1}]^{1/2}$ for the velocity, $t_\circ = r_\circ v_\circ^{-1}$ for the time, so that the orbital period is normalized to 2π, $\rho_\circ = M_\circ r_\circ^{-3}$ for the mass-density, $\epsilon_\circ = v_\circ^2$ for the thermal energy per unit mass and $p_\circ = \rho_\circ\epsilon_\circ$ for the pressure. According to the equivalence $\mathcal{N}_\mathcal{A}\mathcal{K}_\mathcal{B}T_\circ = (\gamma-1)\epsilon_\circ$, where $\mathcal{N}_\mathcal{A}$ and $\mathcal{K}_\mathcal{B}$ are the Avogadro number and the Boltzmann constant, it is possible to determine the normalization temperature $T_\circ$.

In order to complete the boundary conditions, we set the geometric domain including the entire hydrodynamics as the spherical shell, centred on the primary compact star, whose outer edge is $R_{out} = 1$ and whose inner edge is $R_{in} = 10^{-2}$. In this regard, R_{out} is simply the known maximum possible length of the binary system. All SPH particles beyond R_{out} are considered lost in the outer space. Therefore, they are simply eliminated without any numerical involvement of other nearby particles due to the very low pressure gradients outside the primary Roche lobe. All SPH particles closer to the primary compact star than R_{in} are considered as accreted and consequently eliminated, as has also been done by other authors (Murray, 1998; Murray and Armitage, 1998). This involves a local discontinuity in the pressure gradients. However, this is the simplest way to handle the inner boundary conditions, suffering a local limited inaccuracy at distances within h - $2h$ because of the dominance of the gravitational forces at such short radial distances. Any slowdown to the accretion at the inner edge implies a waving of pressure gradients and even an interruption of any accretion. Of course, the boundary condition setting could also include an arbitrary smaller subtraction of particles from such an atmospheric shell at the disc's inner edge. However, this would imply the imposition of an arbitrary accretion rate onto the primary star depending on many physical variables, an aspect that is well beyond the scope of this paper. Notice that being $R_{in} = 10^{-2} r_{\circ} = 10^4$ km, it is comparable with the real radius of a white dwarf star, even though both stellar components are represented as single points with an associated gravitational field.

3. SPH non-viscous disc modelling in LMCBs: how interpolating Kernels and dissipation affect the flow structure

In its original form, the smoothing length h of SPH modelling is assigned from the beginning once for all throughout the numerical simulation. Instead, in the ASPH modelling, any integration-interpolation domain expands or contracts according to an arbitrary criterion of spatial smoothing length variability. However, although solving some problems regarding the accuracy of the numerical integration by counting more neighbours, ASPH modelling suffers from other kinds of inaccuracies (Appendix C.3). Despite the numerical difficulties (Appendix A.2), SPH modelling, whose h is constant, still holds a significant role for an in-depth understanding of discrepancies in the numerical solutions of flow structure and dynamics, especially in non-viscous ideal accretion discs. To this end, among the many Kernel formulations, we pay attention to three Kernel formulation:s $W_{3,ij}$, $W_{1,ij}$ and $W_{erf,ij}$ (Eqs. (A.22), (A.23) and (A.26) respectively). The SPH here working with $W_{3,ij}$, $W_{1,ij}$ compact profiles is both adaptive and non-adaptive. Instead, the spatial resolution length h is always assigned and constant for the SPH Gaussian-based $W_{erf,ij}$ Kernel, while the spatial radial extension of its integration–interpolation is theoretically unlimited. In this case the spatial integration-interpolation is performed up to a radial extension of $4h$ where the value of the 1D Gaussian Kernel is very small compared to its peak value (Appendix A.2).

Assigning established thermal, kinematic, and geometric initial conditions, as well as the stellar masses and their mutual spatial eparation, the main physical feature affecting the flow structure is the specific heat ratio γ within the EoS (Eq. (A.4)). The larger γ, the lower the compressibility. $\gamma = 5/3$ typically refers to a statistically neutral monoatomic gas in adiabatic conditions. However, smaller γ-values, involving radiative losses, are often adopted for monoatomic gases excluding any explicit gas-radiation interaction (Molteni et al., 1991; Lanzafame et al., 1992; Meglicki et al., 1993; Hayasaki and Okazaki, 2004). A $\gamma = 1$ ideally means an isothermal gas configuration. The smaller γ, the higher the gas radiative losses. The attribution of a gas compressibility regime has a relative meaning since the gas compressibility is also strongly affected by the gravitational of the field primary star as well as by the gas chemical composition. A gravitational field far dominant compared to pressure forces indeed easily provides a well-bound SPH flow structure, even at the largest γ-values. This occurs either because of a more massive, compact primary star (e.g. a black hole) (Lanzafame and Belvedere, 2005), or whenever two close compact stars are considered (Motl et al., 2017). In the 2nd case, it happens because of the much shorter $r_{\circ}$, as long as the assumed mass-transfer conditions do not deliberately disadvantage the gravitational field against other forces. However, a far dominant gravitational force field, compared to other forces, would inevitably prevent any analysis of results provided by the adopted algorithms, both on the SPH interpolation and on the flow dissipation, hiding any evidence. This, a fortiori, occurs considering a greater compressibility fluid dynamics determined by lower γ-values. Hence, although more aspects play a role in the gas compressibility, from here onwards we will identify gas compressibility only according to the assigned value of γ for the sake of simplicity.

With the above chosen stellar masses (Section 2), the results in non-viscous conditions show diluted and statistically insignificant disc structures everywhere, whenever low compressibility conditions are taken into account. This happens for γ-values significantly greater than 1, and specifically for $\gamma = 5/3$. Therefore, any non-viscous low compressibility disc structure for $\gamma = 5/3$ is excluded in this Section for the assumed initial conditions, orienting the entire discussion only for smaller values of the specific heat ratio.

3.1. Modelling of SPH inviscid medium compressibility flows

Whenever $\gamma \sim 5/3$ and a mean molecular weight $\overline{\mu} = 1$, any SPH model of non-viscous accretion disc 3D structure is not statistically significant in the LMCB here considered. Therefore, unavoidably, intermediate compressibility conditions are important because they better reveal any defect in the Kernel radial profile through the role of pressure gradients as soon as a statistically significant 3D disc structure begins to form. However, under such deliberately intended conditions, the total number of disc particles cannot be as high as in a high compressibility regime, especially if a variable smoothing length is considered.

In this Subsection, as an example of intermediate compressibility, we assume $\overline{\mu}^{-1}(\gamma - 1) \sim 0.1 - 0.2$ and specifically $\overline{\mu} = 1$ and $\gamma = 1.1$. Assigning such a medium size gas compressibility, Fig. 1 shows the first consistent differences on the 3D accretion disc structures concerning the mass-density ρ in a linear scale of 16 arbitrary colours. In this picture, xy disc structures are shown at time $t = 100$, using either $W_{3,ij}$ (top panels) or $W_{1,ij}$ (bottom panels), and adopting either a constant spatial resolution length (left-side panels) or an adaptive approach ensuring a constant number of neighbours (right-side panels), as discussed in (Appendix C.2). While disc structures for $\gamma = 1.1$ are bound within the primary's gravitational potential well when h is constant, this does not occur if working with that adaptive criterion ensuring a statistical number of 40 neighbours.

Whatever the smoothing variable length criterion, higher numbers of neighbours involving a far larger adaptive h, especially on disc surfaces, is a condition that we do not take into account. On disc surfaces, the variable smoothing lengths are indeed statistically larger than in the disc bulk. This is the consequence of the persistence in counting the same number of neighbours on that part of the disc corresponding to a boundary beyond which there is the empty space. Thus, different radial transport mechanisms exist between the surface-edge disc regions and the disc bulk that are ignited by any h-dependence of the artificial viscosity damping. This involves an arbitrary unphysical ever increasing difference on the radial transport mechanism in the two disc regions as the value of variable h increases by setting higher numbers of neighbours.

It should be clear from here onward that the colour maps shown in the panels for this kind of figure do not strictly have the same linear colour scale whenever the minimum and the maximum scale values, shown at the top-right of each panel, are different.

Notice that using a constant $h = 5\ 10^{-3}$ adopting $W_{3,ij}$, and $h = 10^{-2}$ adopting $W_{1,ij}$, it equals the full radial extension of the SPH integration-interpolation to 10^{-2} with each other (Eqs. (A.22) and (A.23)) at the

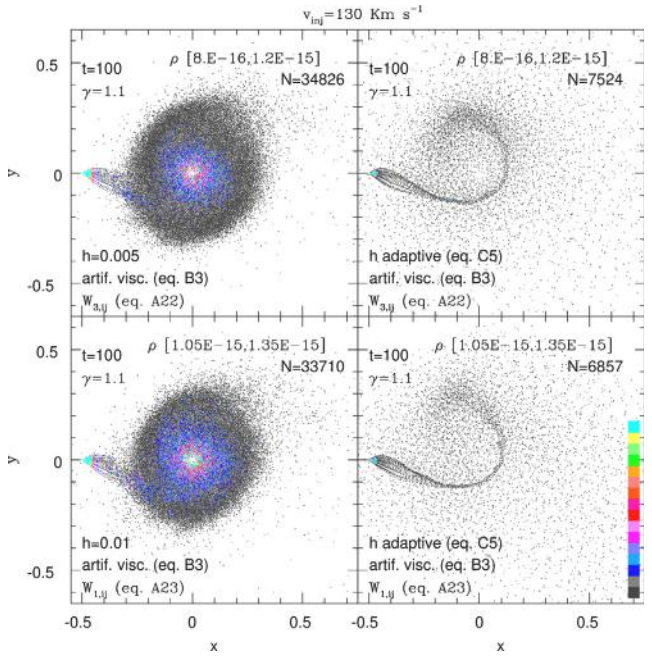

Fig. 1. xy scatter plots in a linear scale of 16 colours of 3D SPH (left-side panels) and ASPH (right-side panels) non-viscous accretion disc models for $W_{3,ij}$ (top panels) and $W_{1,ij}$ Kernels (bottom panels). Colours refer to the dimensionless mass-density ρ. Data identifying the modelling are also reported with references to the Appendices, together with the dimensionless lower and upper ρ values of the colour bar, within the square brackets: $[\rho_{min}, \rho_{max}]$ at the top of each panel. Dots in dark grey (bottom of the colour bar) refer to values of $\rho \leq \rho_{min}$. Dots in cyan(top of the colour bar) refer to values of $\rho \geq \rho_{max}$. As for ρ_{min} and ρ_{max}, the computer exponential notation is used instead of the scientific exponential notation. All N particles are also reported in each panel. v_{inj} is reported on top of the entire figure. Numerical values alongside the colour bar are not reported for practical reasons. The ρ values within to the nth colour of the colour bar are computed as $\rho_n = \rho_{min} + (n-2)(\rho_{max} - \rho_{min})/14$ and $\rho_{n+1} = \rho_{min} + (n-1)(\rho_{max} - \rho_{min})/14$, $n = 2, 3, \ldots, 15$.

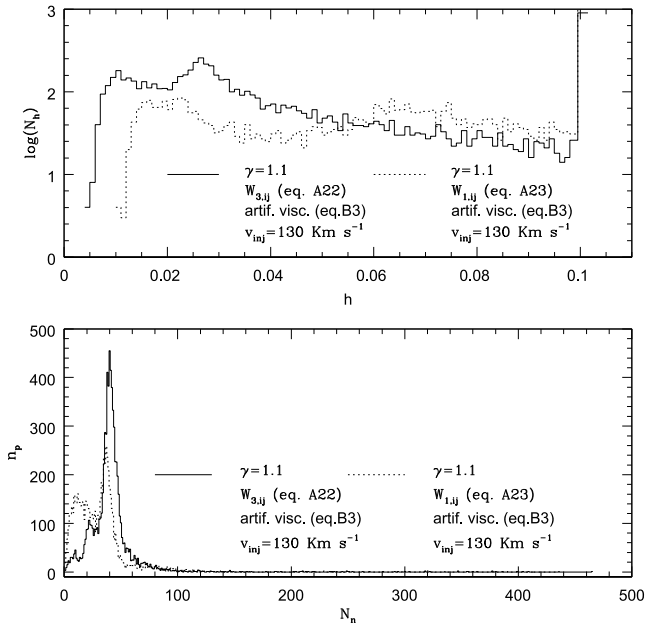

Fig. 2. Histograms showing, for the two ASPH models of Fig. 1, the statistical distribution of particles relative to each variable h (top) and the statistical distribution of particles n_p relative to their companions N_n (bottom).

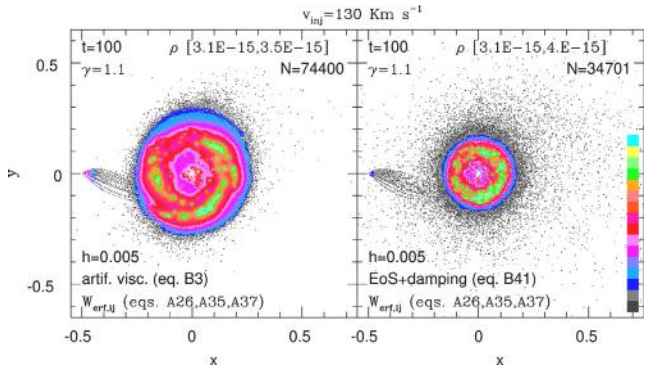

Fig. 3. xy scatter plots in a linear scale of 16 colours of 3D SPH non-viscous accretion disc models for $W_{erf,ij}$. Colours refer to the dimensionless mass-density ρ. Data identifying the SPH modelling are also reported with references to the Appendices, together with the dimensionless lower and upper ρ values of the colour bar, within the square brackets: $[\rho_{min}, \rho_{max}]$ at the top of each panel. Dots in dark grey (bottom of the colour bar) refer to values of $\rho \leq \rho_{min}$. Dots in cyan(top of the colour bar) refer to values of $\rho \geq \rho_{max}$. As for ρ_{min} and ρ_{max}, the computer exponential notation is used instead of the scientific exponential notation. All N particles are also reported in each panel. v_{inj} is reported on top of the entire figure. Numerical values alongside the colour bar are not reported for practical reasons. The ρ values within to the nth colour of the colour bar are computed as $\rho_n = \rho_{min} + (n-2)(\rho_{max} - \rho_{min})/14$ and $\rho_{n+1} = \rho_{min} + (n-1)(\rho_{max} - \rho_{min})/14$, $n = 2, 3, \ldots, 15$.

cost of a different involvement of the artificial viscosity, as expressed by Eq. (B.3). This is a choice we prefer compared to the one that ensures the same artificial viscosity involvement, working with the same h, since different integration-interpolation spatial extensions involve very different numbers of disc particles. In this regard, the study favours the comparison between results obtained from the two different radial profiles of the Kernels when the numbers of neighbours are comparable whenever the smoothing length h is assigned. Thus, this is done when the overall radial extent of the Kernels is the same, as well as the number of neighbours are statistically comparable. By assuming the same assigned value of h, it would be possible to obtain comparable radial transport mechanisms reaching an eightfold number of total particles within the gravitational potential well for the model working with W_1 Kernel and $h = 5\ 10^{-3}$. The time costs of conducting this analysis discourage this path. Based on a comparable radial transport mechanism, which should in principle be physically ruled out due to lack of viscosity, a comparison of inviscid disc models is meaningless. Moreover, different computational errors are also involved working with very different smoothing lengths, as discussed by Vaughan et al. (2008), Vaughan (2009) and Zhu et al. (2015). However, in this work ASPH disc models are also involved which render meaningless those disc models based on radial transport mechanisms that are comparable on the basis of the same smoothing length h. Artificial viscosity is indeed considered of capital importance in the evolution and stability of discs. While, as long there are enough neighbours, the results should be less sensitive to their total number. However, in so far as we are discussing physically non-viscous ideal gas dynamics, the role of any damping should be marginal (better if it is excluded at all) for uniform shear flows, whatever is h. This aspect should be categorical for flow evolutions over a long evolutionary time. In this aspect, the problem is to understand how compatible the artificial viscosity formulation is with a Free Lagrangian shear flow description, with the only exception of flow compressions. This is confirmed by the fact that since the beginning of the 90s (Meglicki et al., 1993), up to recent years (Motl et al., 2017; Taddei et al., 2017; Cabezón et al., 2018), the regulation of artificial viscosity is a difficulty mitigated, but still unsolved, especially for ASPH techniques.

In order to understand how many neighbours are statistically around, histograms in Fig. 2 show, as far as the two adaptive disc models are concerned, the distribution of how many particles N_h

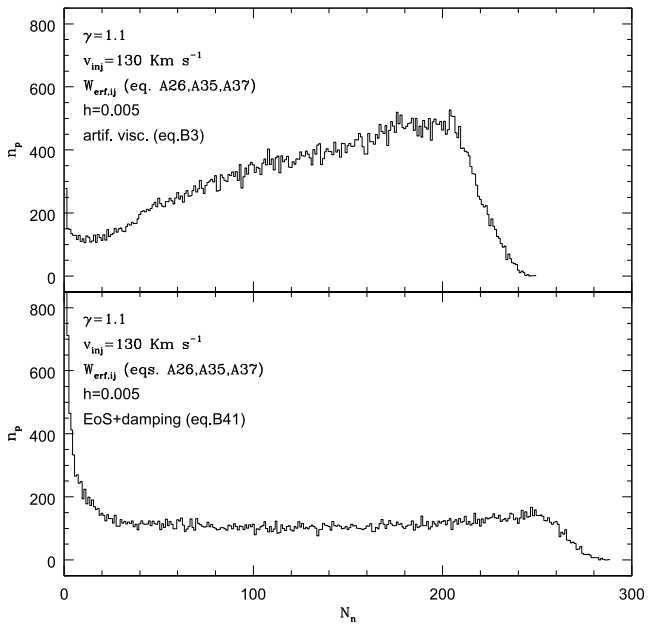

Fig. 4. Histograms showing, for the two SPH $W_{erf,ij}$ models of Fig. 3, the distribution of particles n_p relative to their companions N_n within the radial interpolation extension $4h$.

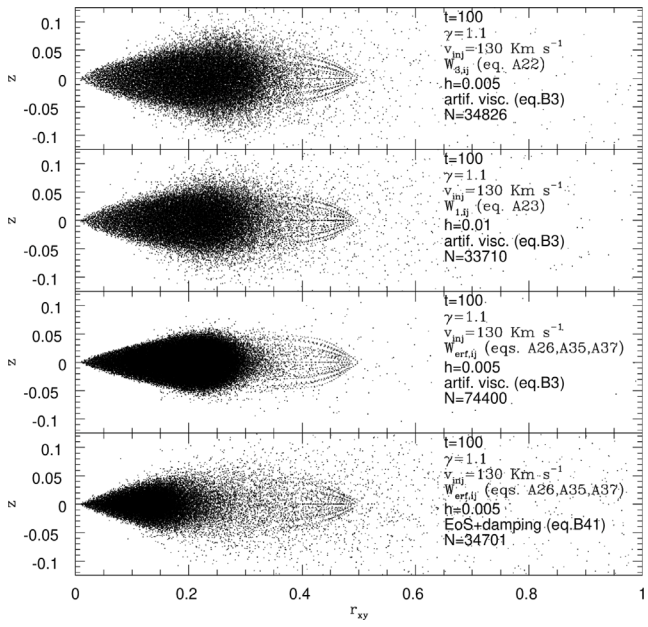

Fig. 5. (r_{xy}, z) plots for the most significant models of Figs. 1 and 3. All disc modelling data are reported for each panel.

refer to each h (top) within a small interval. Fig. 2 also shows, the distribution of particles n_p relative to their companions N_n (bottom). This second picture, in particular, shows how effective is Eq. (C.5) in statistical terms. Instead, as regards the number of neighbours for the two non-adaptive disc structures on the left of Fig. 1 (here not shown), N_n is roughly of the order of a 12–15 in the disc steady configuration. These numbers are not assigned from the beginning. Such low numbers allow only the understanding of some general features, excluding those capillary aspects of the flow structures. Whatever are the statistical fluctuations providing some secondary peaks on n_p at the bottom of Fig. 2, it is essential to note that their numbers are of the order of a few hundreds and, therefore, negligible compared to the total number of the disc particles ($N \sim 6\ 10^3$–$7\ 10^3$). The few n_p particles having high number of neighbours N_n shown at the bottom of Fig. 2, are due to the statistical variability of h which is deliberately truncated at $h = 0.1$ avoiding its excessive increase. However, this does not involve that the n_p statistical distribution is bimodal.

Fig. 3 instead displays at time $t = 100$ the xy accretion discs structures working with $W_{erf,ij}$. The linear scale of 16 colours refers to ρ. All the indications regarding the normalization of integration and the dissipation considered in the Euler equations (Appendices A and B) are also reported in each panel. In this figure, the left panel refers to the simplest use of $W_{erf,ij}$ to which the refinements of Eqs. ((A.37) and (A.39)) are also adopted, aiming to get a better consistency of numerical solutions. Instead, in the right panel, a reformulation of dissipation within the EoS (Eq. (B.41)) is also considered instead of the currently adopted artificial viscosity (Eq. (B.3)).

Any disc structure relative either to the simplest SPH use of $W_{erf,ij}$ or to its XSPH (Eqs. (A.18) and (A.19)) application, whose algorithm is shown at the end of (Appendix A.1) is not shown in this Subsection, as their differences with disc structures shown in Fig. 3 are irrelevant.

Even though ASPH disc models collect a statistically significant number of companions, pressure forces of the many farther neighbours that are near the edge of the integration-interpolation domain, incorrectly move away disc particles from each other. Such pressure force excess prevents any disc formation despite the negative total energy of particles generated around L_1. Such an excess in the $-\nabla p$ term comes out from the incorrect higher spatial derivatives in the radial distribution of $-\nabla W_{3,ij}$ and $-\nabla W_{1,ij}$ as shown in Figs. A.40 and A.41, preventing any bound flow structure within the gravitational potential well. This misbehaviour is enhanced under adaptive conditions due to the significant role of pressure forces of the many farther SPH neighbours, being the gravitational field of the primary star slightly prevailing. Furthermore, the different behaviour of pressure forces in adaptive conditions is also detected by the large pushing action of particles of the injected particle stream, leading to an intense stream crushing as shown in the two right panels of Fig. 1.

Despite the negative total energy of the flow at L_1, what is clear from Figs. 1–3 is that the ASPH disc structures are heavily the worst compared to both discs whose h is constant and whose particles have around much fewer neighbours. Such a result cannot be improved by further increasing the assigned arbitrary number of neighbours by expanding h. Therefore, the root of SPH difficulties in 2D and 3D modelling is elsewhere, as it is shown in this first comparison. In fact, although $W_{erf,ij}$ works with an unpopular 1D Gaussian-based Kernel, the normalization obtained through $(4\pi r^2)^{-1}$ compensates any modification of the radial profile of the integral function coming from $d^3\mathbf{r}$. Thus, the main root of 2D and 3D pairing instability of the closest neighbours, together with pressure gradient excesses of the many farther neighbours (Appendix A.2), are due to the 2D and 3D differential vectors involving multiplicative radial terms in 2D and in 3D SPH integrations. Hence, the imposition of more neighbours in ASPH makes worse such deficiency together with a damping excess, which are hidden, whatever is γ, whenever a far dominant gravitational field is considered.

Being the spatial resolution length h constant, and being the radial extension of the $W_{erf,ij}$ Kernel unlimited, we performed SPH integrations up to a radial extension of $4h$. This choice is motivated because any numerical deviation from condition of Eq. (A.21) is negligible for $0 \le r_{ij} \le 4h$, as discussed in Appendix A.2. In fact, assuming $h = 1$, the "complementary error function" $erfc(4) \sim 10^{-9}$ (Eq. (A.33)) as long as a statistically significant number of neighbours exists. Since the statistical number of neighbours is satisfactory, as shown in Fig. 4, such an SPH integration-interpolation process is meaningful. The hundreds of particles having a few neighbours within $4h$, shown at the bottom panel of Fig. 4, are particles populating the outflowing external diluted

halo to which we pay no attention since they do not interact with the disc structure.

The left panel of Fig. 3 shows a disc's radial extension and shape not very different compared to those shown on the left of Fig. 1. Hence, the outer limit of disc's radial extension, physically determined by the tidal truncation radius, is reached well before $t = 100$ working with the same γ in intermediate compressibility conditions. Moreover, as long as the viscous radial transport is activated by the artificial viscosity (Eq. (B.3)), with $\alpha_* = 1$ and $\beta_* = 2$, it is unclear if it is the first cause of the disc's radial stretching in these disc modelling, despite the three analytical Kernel formulations. The disc's radial stretching for the model working with $W_{erf,ij}$ showed a consistently slower radial progression than the others. However, this result can also be justified in terms of smaller pressure forces of the many farther companions for $W_{erf,ij}$, instead than in terms of viscous transport, despite their connection. Such a slower radial spreading, working with $W_{erf,ij}$ was also detected in Lanzafame (2010a) simulating the radial spreading of an isothermal, pressure-free annulus ring. Such a slower radial transport on the non-viscous disc fluid dynamics somehow meets the need to reduce the excess of the mass-transfer rates and the consequent disc faster radial dynamic evolution for SPH disc modelling, as reported by Motl et al. (2017).

Tidal torques in accretion discs of close binaries were originally studied by Papaloizou and Pringle (1977). They used a linear perturbation method for a tidally perturbed flow in the accretion disc by decomposing the tidal perturbation potential into Fourier components. They found that tidal torque is a rapidly increasing function of the cylindrical radial coordinate r_{xy} as $\propto r_{xy}^5$. According to a different approach, Zhang and Chen (1992) solved the linear tidal perturbation equation by adopting a direct numerical integration method. Instead, Ichikawa and Osaki (1994) calculated tidal torques both according to a linear perturbation method and to a non-linear method based on single periodic particle orbits in the primary Roche lobe influenced by the binary gravitational potential. All these calculations were performed considering non-collisional fluid dynamics models, that is involving negligible pressure and viscosity forces. In particular, tidal effects (i.e. tidal dissipation and tidal torque) are generally small in accretion discs, except beyond or near the tidal truncation radius, which is given by the largest periodic particle orbit that does not intersect the inner periodic orbit in the disc:

$$\frac{r_{xy}}{d_{12}}\Big|_{t.t.r.} = \left(\frac{2\pi}{c\omega_{orb}} f\right)^5, \tag{1}$$

where ω_{orb} is the orbital angular velocity, f is the tidal torque, both having dimensions of s^{-1} and $c\omega_{orb} \approx 0.2$–$15$ (Ichikawa and Osaki, 1994). This means that the tidal truncation radius generally ranges from $\approx 0.42f$ to $\approx 31.42f$. According to Paczynsky (1977), Papaloizou and Pringle (1977), Ichikawa and Osaki (1992) and Ichikawa and Osaki (1994), the accretion disc should be tidally truncated very close to the tidal truncation radius in a steady state. Once the disc radially expands up to the tidal truncation radius, the tidal torque should prevent the disc from expanding further. Extra angular momentum transported towards the disc's outer edge should be redistributed to the orbital motion of the binary. This is the only theoretically known relationship as far as the tidal truncation radius is concerned. Looking at the left panels of Figs. 1 and 3 it seems that $(r_{xy})_{t.t.r.} \approx 0.3$ (hereinafter r_{xy} instead of $r_{xy}d_{12}^{-1}$) for our binary system, at least in non-viscous conditions. Such a value, at time $t = 100$, is far larger than that shown in Lanzafame (2003) for $t = 22$ and $\gamma = 1.01$. Thus, spiral patterns and spiral shocks in the radial flow are collisionally due mainly to the angular momentum and energy conditions from L_1, together with a marginal support due to the secondary's tidal forces, whenever the disc's radial extension reaches or stretches farther that radial limit. Instead, below $(r_{xy})_{t.t.r.}$, tidal effects on the disc structure and dynamics are negligible especially for low compressibility flows, so that low and, somehow, intermediate compressibility disc structures should be free of any spiral pattern at the innermost radial distances.

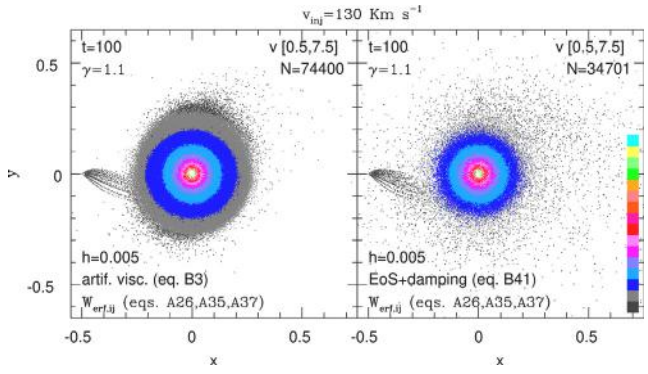

Fig. 6. xy scatter plots in a linear scale of 16 colours of 3D SPH non-viscous accretion disc models of Fig. 3. Colours refer to the dimensionless total velocity v. Data identifying the SPH modelling are also reported with references to the Appendices, together with the dimensionless lower and upper v values of the colour bar, within the square brackets: $[v_{min}, v_{max}]$ on top of each panel. Dots in dark grey (bottom of the colour bar) refer to values of $v \le v_{min}$. Dots in cyan (top of the colour bar) refer to values of $v \ge v_{max}$. All N particles are also reported in each panel. v_{inj} is reported on top of the entire figure. Numerical values alongside the colour bar are not reported for practical reasons. The v values within to the nth colour of the colour bar are computed as $v_n = v_{min} + (n-2)(v_{max} - v_{min})/14$ and $v_{n+1} = v_{min} + (n-1)(v_{max} - v_{min})/14$, $n = 2, 3, \ldots, 15$.

The left panel of Fig. 3 shows weak but clear evidence of spiral pattern structures, better enhanced in the arbitrary linear scale of 16 colours we considered. Some ρ inhomogeneities along the spiral patterns also appear, which are a peculiarity detected within the disc bulk since the initial settlement of the toroidal flow during the first phases of disc formation.

As far as the disc structure on the right panel of Fig. 3 is concerned, the adoption of a physical dissipation within the EoS (Eq. (B.41)) for ideal gases activates a dissipation working only whenever local flow compressions are effective. Any artificial viscosity (Eq. (B.3)) working for every approach of single particles in binary particle collisions is excluded. This unavoidably reduces the overall disc's radial spreading, preventing any collective outward radial transport mechanism, since a statistical Keplerian kinematics involves very low $\nabla \cdot \mathbf{v}$ values except for disc edges and the injected flow stream. Such a smaller disc structure on the right-side of Fig. 3 is obtained by assigning a value to $\mathcal{K}$ of Eqs. ((B.38) and (B.41)) right just for enabling the formation of a statistical significant disc structure. This short numerical experiment empirically led to a value of $\mathcal{K} \approx 2\ 10^3$ just in half of the orbital period. Of course, being the radial stretching of this disc structure shorter than $(r_{xy})_{t.t.r.}$, any spiral pattern development in the mass-density is inhibited. This is shown in the same picture highlighting clear residual toroidal flow turbulence appearing as a trace of the toroidal ring characterizing the initial evolutionary phases of the flow around the primary compact star (Lubow and Shu, 1975). This leads to the further conclusion that any damping activated according to a criterion involving compressions through $\nabla \cdot \mathbf{v} < 0$ shows a character of turbulence in physically inviscid fluids, even excluding any real viscosity.

Fig. 5 shows (r_{xy}, z) plots of the most significant disc modelling of Figs. 1 and 3. These plots further contribute to the understanding of how differently the $W_{erf,ij}$ Kernel works and how much different the radial transport for ideal gases is when it is activated by Eq. (B.41) for dissipation instead of Eq. (B.3). No significant discrepancies exist on the disc angular thickness, except the presence of a low-density particle envelope on disc surfaces for $W_{3,ij}$ and $W_{1,ij}$ disc models, together with a consistent outflow of particles from the disc's outer edge. This detail shows how strong is the repulsive action of pressure forces due to the excess of spatial gradients of the many farther neighbour within the $W_{3,ij}$ and $W_{1,ij}$ integration domains. Free of any pressure force excess on the tail of the radial distribution of neighbours for

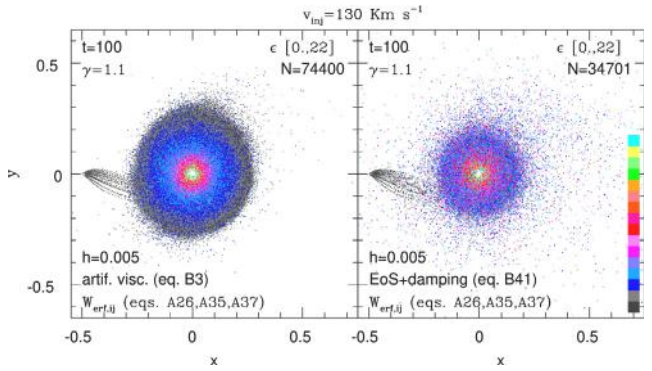

Fig. 7. xy scatter plots in a linear scale of 16 colours of 3D SPH non-viscous accretion disc models of Fig. 3. Colours refer to the dimensionless thermal energy per unit mass ϵ. Data identifying the SPH modelling are also reported with references to the Appendices, together with the dimensionless lower and upper ϵ values of the colour bar, within the square brackets: $[\epsilon_{min}, \epsilon_{max}]$ on top of each panel. Dots in dark grey (bottom of the colour bar) refer to values of $\epsilon \leq \epsilon_{min}$. Dots in cyan (top of the colour bar) refer to values of $\epsilon \geq \epsilon_{max}$. All N particles are also reported in each panel. v_{inj} is reported on top of the entire figure. Numerical values alongside the colour bar are not reported for practical reasons. The ϵ values within to the nth colour of the colour bar are computed as $\epsilon_n = \epsilon_{min} + (n-2)(\epsilon_{max} - \epsilon_{min})/14$ and $\epsilon_{n+1} = \epsilon_{min} + (n-1)(\epsilon_{max} - \epsilon_{min})/14$, $n = 2, 3, \ldots, 15$.

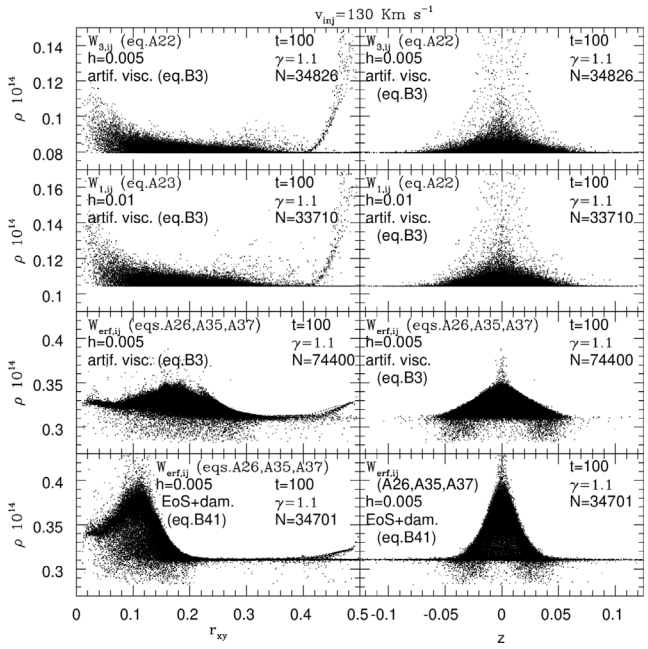

Fig. 8. r_{xy} radial and z vertical distributions of dimensionless values of (ρ 10^{14}) for the most significant accretion disc models of Figs. 1 and 3. In each panel some modelling data are reported, together with references (in the Appendices) regarding both the numerical normalization and the dissipation. v_{inj} is reported on top of the entire figure.

$W_{erf,ij}$, any outflow of particles from the disc's outer edge is almost negligible, even adopting the same formulation (Eq. (B.3)) for the artificial viscosity contribution (Lanzafame, 2010a). This is shown in the 3rd panel from top to bottom. Instead, a strong outflow exists for the modelling adopting $W_{erf,ij}$ and whose dissipation is ruled by Eq. (B.41) at the disc's outer edge, as it is shown at the bottom panel. This outflow of particles is due to the positive increase of $-\nabla \cdot \mathbf{v}$ occurring whenever strong local compressions occur. Such compressions exist especially around the impact region between the disc's outer edge and the gas stream gas coming from L_1, although even the disc's inner edge cannot be excluded.

Figs. 6 and 7 show the same disc models of Fig. 3 in a linear scale of 16 colours representation for the total velocity v and ϵ. An undoubted radial gradient of speed unites the disc models, as shown in Fig. 6. Indeed, radial distributions of speed comparable with each other also characterize the disc models where $W_{3,ij}$ and $W_{1,ij}$ Kernels are adopted, which are not shown for the sake of practicality. This demonstrates how much the kinematics of the disc is controlled by the gravitational forces compared to pressure and dissipative ones, even for low-mass stars of the binary system. Instead, although a radial distribution along the orbital plane of ϵ exists in Fig. 7 throughout disc models, the overlap of a hot component also appears especially for the disc model on the right panel of the picture. Such a hot component comes out because of the wide opening of the high-speed inflow leading to a stream flow shearing on disc surfaces at short radial distances r_{xy}. In fact, despite the angular thicknesses are comparable throughout the disc models, the shorter radial extension of the disc model working with $W_{erf,ij}$ and Eq. (B.41) determines a smaller outer edge thickness. In particular, particles whose kinematics deviates from the Keplerian one on disc surfaces show a specific thermal energy ϵ significantly larger as a consequence of abrupt $\nabla \cdot \mathbf{v}$ variations when adopting Eq. (B.41).

The adoption of damping through EoS (Eq. (B.41)) instead of artificial viscosity provides an unusual picture. Disc structures are small, symmetrical, surrounded by a chaotic flow of outflowing gas and characterized by a density accumulation in the disc bulk. This is, however, explained by the search for a physically non-viscous disc model. Any collisional Lagrangian damping mechanism like the artificial viscosity, working like a real physical viscosity in shear flows (Okazaki et al., 2002), provides a radial transport of mass and momentum, does not match the assertion of the absence of a physical viscosity. So that, disc structures on the right panels of Figs. 3, 6, and 7, while unusual, are closer to a non-viscous physical reality than to a viscous one. Thus, according to Okazaki et al. (2002), artificial viscosity in a Lagrangian approach, like any other dissipation, activated by particle collisions would never have produced a truly inviscid disc structure because a dissipation suitable for the solution of the Riemann problem is not suitable for simulating shear flows.

An in-depth inspection of the structures and dynamics of disc models can be made by looking at Figs. 8–10 showing the radial and the vertical distributions of ρ, ϵ and v. In the radial distribution plots on the left of each figure, such physical properties are reported as a function of r_{xy}. In the vertical distribution plots on the right of each figure, they are reported as a function of z. Descriptions of panels within these pictures proceed from top to bottom.

Fig. 8 shows the two spatial distributions of the mass-density ρ relative to disc models working with either $W_{3,ij}$ or $W_{1,ij}$ Kernels and constant h values in the two pairs of panels from the top. Within the primary's gravitational potential well, any memory of the initial torus is missing since the radial distribution of ρ is rather flat throughout the two discs. A component of increasing ρ values is also shown, towards decreasing r_{xy} and $|z|$ values, for the same two models. Instead, by adopting $W_{erf,ij}$, the clear evidence of a peak on the radial distribution of the mass-density ρ is related to the presence of a residual toroidal structure, and it is essential both on its radial and on its vertical distributions shown in the 3rd couple of panels. Another mass-density profile, always increasing as $r_{xy} \to 0$, is also shown, whose values do not exceed the torus mass-density peak. Another important peculiarity shown in this picture is that disc models adopting $W_{erf,ij}$ are thinner than those adopting $W_{3,ij}$ and $W_{1,ij}$ Kernels, as shown in the panels on the right-side referring to the vertical disc distributions and as previously widely discussed as for Fig. 5. This peculiarity clearly emerges from the presence of low density surface flows for high $|z|$ values in disc models working with $W_{3,ij}$ and $W_{1,ij}$ Kernels rather than$W_{erf,ij}$ (third pair of panels). The 4th couple of panels, left and right, of Fig. 8 shows the radial and the vertical distribution of ρ when $W_{erf,ij}$ is adopted together with a reformulation of dissipation within the EoS (Eq. (B.41)) instead of artificial viscosity (Eq. (B.3)). In this case,

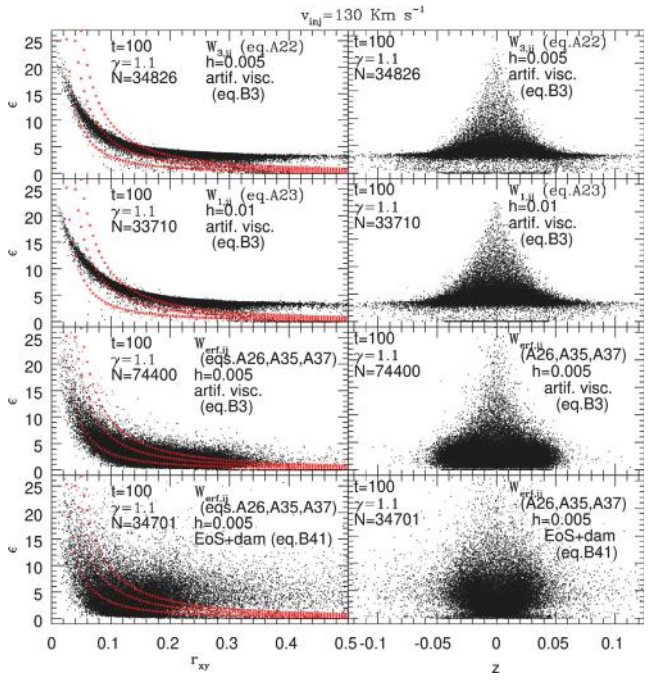

Fig. 9. r_{xy} radial and z vertical distributions of dimensionless values of ϵ for the most significant accretion disc models of Figs. 1 and 7. In each panel some modelling data are reported, together with references (in the Appendices) regarding both the numerical normalization and the dissipation. v_{inj} is reported on top of the entire figure. In the left-side panels, regarding the radial distribution, some profiles in red are also shown, each relative to a $\epsilon \approx S r_{xy}^{-3/2}$ profile, whose $S = 0.1$, 0.2 and 0.3.

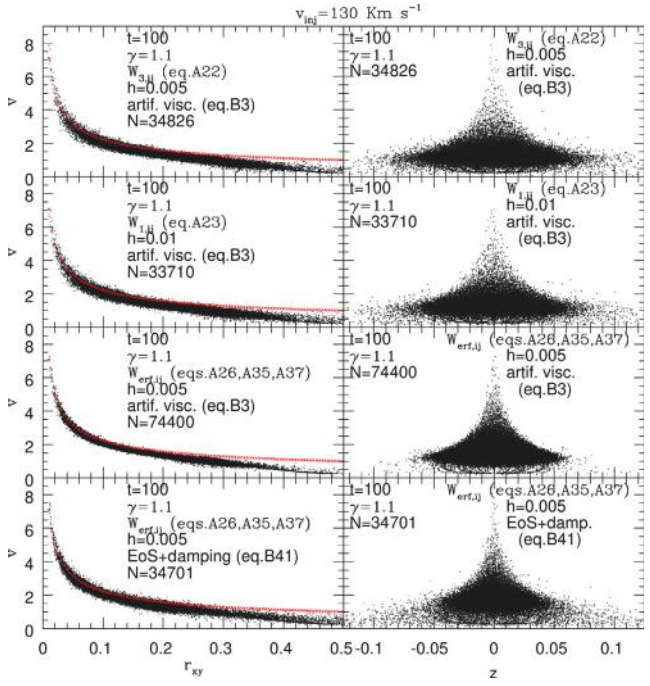

Fig. 10. r_{xy} radial and z vertical distributions of dimensionless values of the total velocity v for the most significant accretion disc models of Figs. 1 and 6. In each panel some modelling data are reported, together with references (in the Appendices) regarding both the numerical normalization and the dissipation. v_{inj} is reported on top of the entire figure. In the left-side panels, regarding the radial distribution, some profiles in red are also shown, each relative to the Keplerian kinematics profile.

the toroidal mass-density peak still holds its radial position, without any significant outward radial stretching. Hence, any formation of spirals following the disc viscous radial stretching, whenever the radial disc extension exceeds the tidal truncation radius, is inhibited. At the same time, an extended halo of particles outflowing far from the disc, undoubtedly shows how quickly the disc structure and dynamics get a steady-state configuration in this case, because free of any significant radial transport.

As regards the specific thermal energy ϵ, the two radial distributions on the top-left concerning the $W_{3,ij}$ and the $W_{1,ij}$ disc modelling and a constant h, are strictly comparable with each other. The same conclusion can also be reached by comparing their respective vertical distributions on the top-right. This is important, even though the larger h for the disc model adopting the $W_{1,ij}$ Kernel, should involve a more effective artificial viscosity and, consequently, a larger particle dissipative heating which is perceptible only from $r_{xy} \sim 0.1$ inwards. This result shows that such dissipative heating should need a higher particle collisional rate, which means a larger particle number density for both models to better highlight such discrepancies even at longer radial distances. A peculiarity throughout the disc structures is the presence of a hot subkeplerian sliding shearing flow on disc surfaces. The superficial sliding of subkeplerian flows coming from the injected stream is described in Lanzafame et al. (1992) for the accretion disc model of SS-Cyg, whose sonic mass-transfer conditions around L_1 provided a thinner disc thickness as a consequence of the 10 times slower kinematics at L_1. For this reason, the "cold over disc stream" was still holding the initial values of ϵ from L_1, as described in that paper. A glimmer of a colder component also exists throughout the last two radial disc distributions of Fig. 9. This is possible because, looking also at Fig. 5, the shorter the disc's radial extension, the thinner the disc's outer edge thickness, especially if working with $W_{erf,ij}$. Such a peculiarity is particularly evident if the adoption of $W_{erf,ij}$ is combined with the adoption of Eq. (B.41) for the non-viscous damping, instead of Eq. (B.3). The shearing on disc surfaces of such sliding subkeplerian flows is the only cause of consistent heating due to the dissipation working with $\nabla \cdot \mathbf{v} < 0$ of Eq. (B.41) of a fraction of the subkeplerian sliding flow. This is better visible in the two vertical distributions at the bottom-right of Fig. 9. According to this scenario, the reduction of the disc radius, occurring when adopting $W_{erf,ij}$ together with Eq. (B.41), involves both hot and cold flow components and scattered particles throughout the disc, as shown in the couple of panels at the bottom of the picture. All panels on the left also report the theoretical radial distributions of ϵ for three different values of $\approx S r_{xy}^{-3/2}$. These are the radial distributions of ϵ dealing with the so-called disc standard model proposed by Shakura (1973) and Shakura and Sunyaev (1973) corresponding to a non-collisional very thin disc model around a black hole. These panels clearly show that, whenever a cold particle component exists, a value $S \approx 0.1 - 0.2$ well agrees with the radial distribution of ϵ. Instead, $S \approx 0.2$ is a good fitting value without the cold particle component, exception for the innermost disc regions.

Both the radial distributions of the total velocity v, as well as the vertical ones are shown in Fig. 10 in pairs of panels (left–right) for the same disc models, as in Figs. 8 and 9. The Keplerian velocity radial profile is in good agreement throughout the disc models, as shown in the left-side panels, except for the subkeplerian regions on disc surfaces. This is an aspect that unites all disc models since the populations of subkeplerian particles are relevant everywhere. Such subkeplerian particle populations are also found in the outer disc regions because they are still conserving a memory of their initial kinematic conditions and because they are under the influence of the gravitational field of the secondary star. It also appears that in models working with $W_{erf,ij}$ and with artificial viscosity (Eq. (B.3)), any local deviation from the strictly Keplerian profile, is smaller than that relative to the other disc models, because free of pressure gradient excesses along the radial profile of the Kernel spatial derivative. This further confirms that the choice of $W_{erf,ij}$ is more than satisfactory. The large deviations from the Keplerian profile occurring when working with Eq. (B.41) are due to the statistical local increase of $-\nabla \cdot \mathbf{v} > 0$, as shown in the two panels

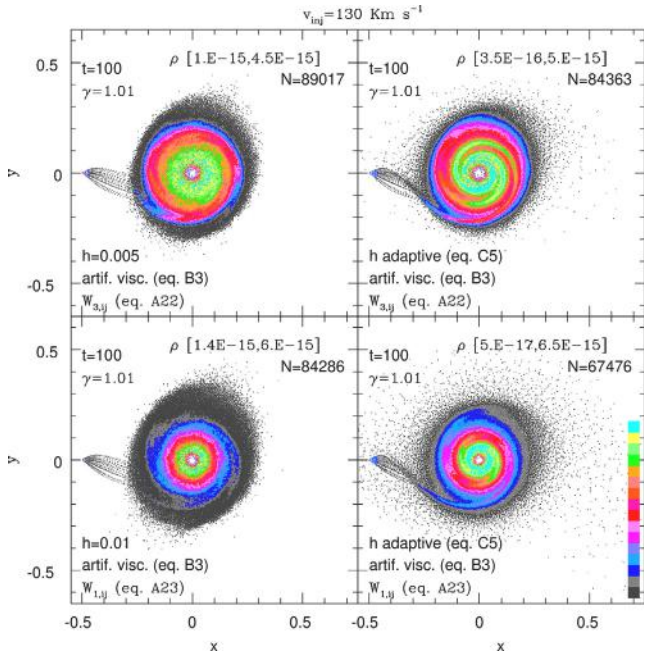

Fig. 11. xy scatter plots in a linear scale of 16 colours of 3D SPH (left-side panels) and ASPH (right-side panels) non-viscous accretion disc models for $W_{3,ij}$ (top panels) and $W_{1,ij}$ Kernels (bottom panels). Colours refer to the dimensionless mass-density ρ. Data identifying the modelling are also reported with references to the Appendices, together with the dimensionless lower and upper ρ values of the colour bar, within the square brackets: $[\rho_{min}, \rho_{max}]$ at the top of each panel. Dots in dark grey (bottom of the colour bar) refer to values of $\rho \leq \rho_{min}$. Dots in cyan(top of the colour bar) refer to values of $\rho \geq \rho_{max}$. As for ρ_{min} and ρ_{max}, the computer exponential notation is used instead of the scientific exponential notation. All N particles are also reported in each panel. v_{inj} is reported on top of the entire figure. Numerical values alongside the colour bar are not reported for practical reasons. The ρ values within to the nth colour of the colour bar are computed as $\rho_n = \rho_{min} + (n-2)(\rho_{max} - \rho_{min})/14$ and $\rho_{n+1} = \rho_{min} + (n-1)(\rho_{max} - \rho_{min})/14$, $n = 2, 3, \ldots, 15$.

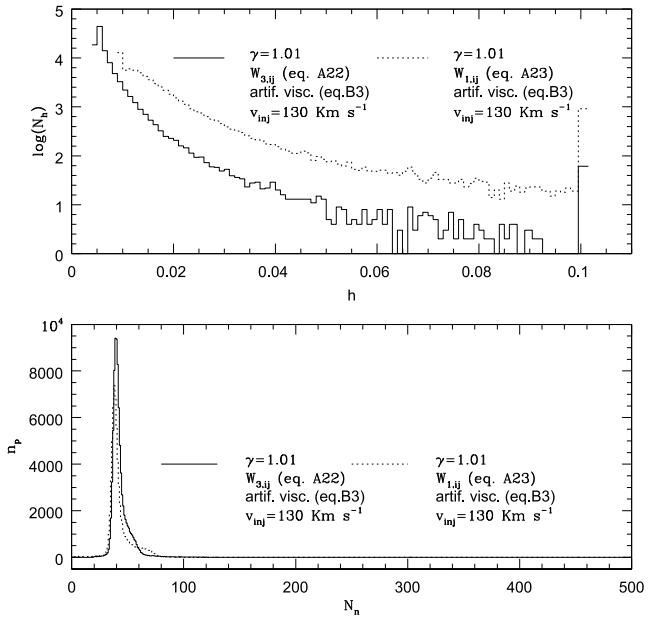

Fig. 12. Histograms showing, for the two ASPH models of Fig. 11, the statistical distribution of particles relative to each h (top) and the statistical distribution of particles n_p relative to their companions N_n (bottom).

at the bottom. Such circumstances originate scattered particles from the disc surfaces, as also shown in the vertical distribution.

A noteworthy final consideration as far as the spatial distributions are concerned is needed. Because of the collisional fluctuations in the compressibility conditions discussed, any fitting of the spatial distribution of physical properties could show fewer peculiarities than in higher compressibility, even though it is relevant how the stronger pressure forces enhance some flow behaviours.

3.2. Modelling of SPH non-viscous high compressibility flows

In the limit of isothermal flow structures, a ratio of specific heats γ as close as possible to 1 is assigned. In that limit, it is assumed that all the heating coming from the conversion of mechanical energy into heat is irradiated towards the outer space.

In this context we performed 3D SPH simulations working with $\gamma = 1.01$ and $\overline{\mu} = 1$, still adopting $W_{3,ij}$, $W_{1,ij}$ and $W_{erf,ij}$ Kernels with the same criteria for h as in Section 3.1. All conclusions, written in that Subsection, which explain differences in the disc structures, should benefit of statistically more significant flows and structures, despite the smaller pressure forces reduce all discrepancies. All the defects affecting $W_{3,ij}$ and $W_{1,ij}$ Kernels do in fact still exist, although any still existing pressure force inaccuracy is much weaker than the gravitational forces.

Fig. 11 shows the xy plots of disc structures of the mass-density distributions of both $W_{3,ij}$ (top panels) and $W_{1,ij}$ (bottom panels) in a linear scale of 16 colours. The spatial resolution length is assigned and invariable for the two panels on the left. Instead, it is adaptive for the two panels on the right, still working with Eq. (C.5) and still assigning an arbitrary number of 40 neighbours.

As far as the two adaptive disc models are concerned, histograms in Fig. 12 show the distribution of how many particles N_h refer to each variable smoothing length h (top). At the same time Fig. 12 also displays the distribution of particles n_p relative to their companions N_n (bottom) showing how effective is Eq. (C.5) in statistical terms.

As regards the two disc models whose constant smoothing lengths are $h = 5\ 10^{-3}$ and $h = 10^{-2}$ (on the left of Fig. 11), $N_n \approx 25$–30 (not shown for the sake of practicality). This is statistically the number of neighbours around throughout such two disc models. Such numbers still have little statistical meaning in the 3D SPH modelling. However, such disc models are anyway useful for understanding the flow structures.

Three details are evident since the first glance of Figs. 11 and 12. The first detail is that, despite the smaller number of neighbours, both h-constant disc models show a radial extension greater than that referring to both adaptive models. In ASPH models, the larger radial transport mechanism activated by the increase of the variable smoothing length h, should correctly lead to an increase of the disc's radial extension. However, the radial transport alone is not the only cause of the disc's radial stretching. Whenever a pressure force excess exists, a consequent accretion rate excess also exists. This is the consequence of the combined action of artificial viscosity radial transport and pressure force excesses due to the many farther companions distributed on the tail of the Kernel radial profiles Figs. A.40 and A.41, affecting especially the two ASPH disc models. The consequent higher accretion rate disadvantages the disc's radial extension by subtracting more mass from the disc's inner edge, excessively depleting the whole disc structure from within. The entire disc radius and the total number of disc particles are accordingly reduced as a result of the rearrangement of disc structure caused by the greater emptying from the inner edge. Such two inadequacies mostly affect the models whose spatial resolution length h is statistically larger. This is also confirmed by looking at the top panel of Fig. 12 displaying how large is the population of particles whose $h > 10^{-2}$. Instead, no remarkable variations on the disc's outer edge outflow are recorded in adaptive conditions. This aspect highlights the heavy dependence of the adaptive SPH modelling on the arbitrariness of choosing the assigned number of neighbours.

The second detail deals with the injected flow stream for the two adaptive disc models on the right of Fig. 11, whose morphology is

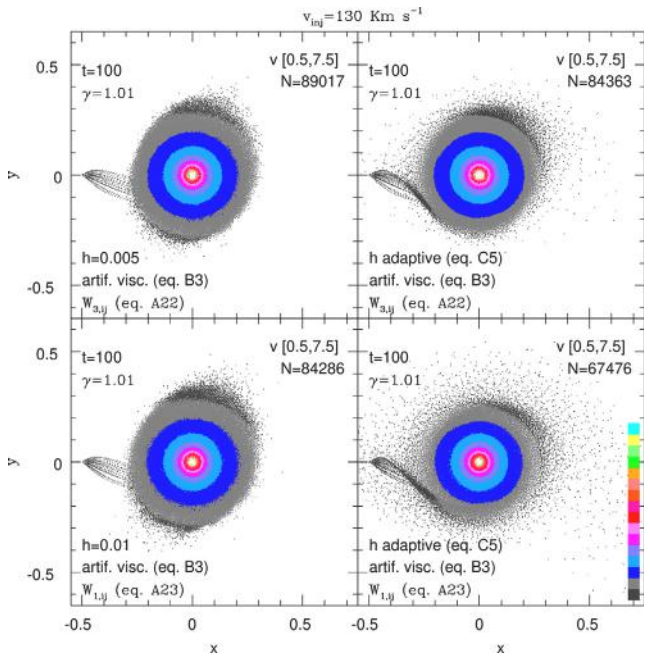

Fig. 13. xy scatter plots in a linear scale of 16 colours of non-viscous accretion disc models of Fig. 11. Colours refer to the dimensionless total velocity v. Data identifying the SPH modelling are also reported with references to the Appendices, together with the dimensionless lower and upper v values of the colour bar, within the square brackets: $[\mathrm{v}_{min}, \mathrm{v}_{max}]$ on top of each panel. Dots in dark grey (bottom of the colour bar) refer to values of $\mathrm{v} \leq \mathrm{v}_{min}$. Dots in cyan (top of the colour bar) refer to values of $\mathrm{v} \geq \mathrm{v}_{max}$. All N particles are also reported in each panel. v_{inj} is reported on top of the entire figure. Numerical values alongside the colour bar are not reported for practical reasons. The v values within to the nth colour of the colour bar are computed as $\mathrm{v}_n = \mathrm{v}_{min} + (n-2)(\mathrm{v}_{max} - \mathrm{v}_{min})/14$ and $\mathrm{v}_{n+1} = \mathrm{v}_{min} + (n-1)(\mathrm{v}_{max} - \mathrm{v}_{min})/14$, $n = 2, 3, \ldots, 15$.

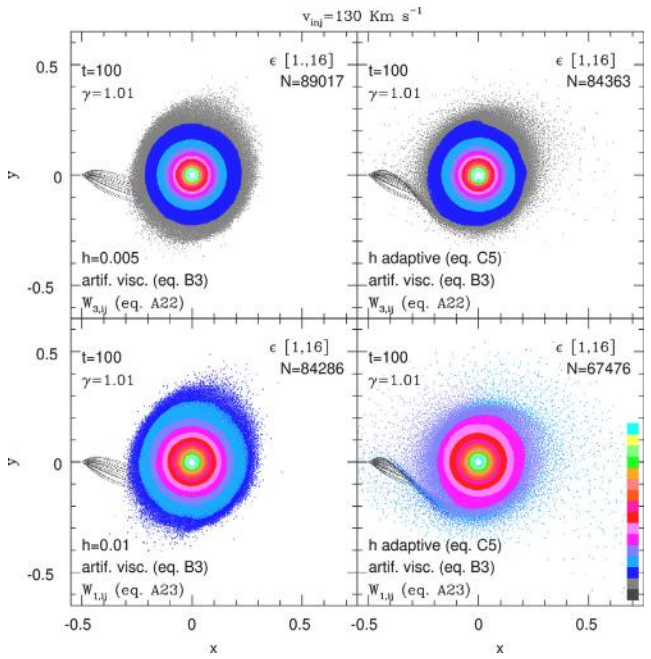

Fig. 14. xy scatter plots in a linear scale of 16 colours of non-viscous accretion disc models of Fig. 11. Colours refer to the dimensionless thermal energy per unit mass ϵ. Data identifying the SPH modelling are also reported with references to the Appendices, together with the dimensionless lower and upper ϵ values of the colour bar, within the square brackets: $[\epsilon_{min}, \epsilon_{max}]$ on top of each panel. Dots in dark grey (bottom of the colour bar) refer to values of $\epsilon \leq \epsilon_{min}$. Dots in cyan (top of the colour bar) refer to values of $\epsilon \geq \epsilon_{max}$. All N particles are also reported in each panel. v_{inj} is reported on top of the entire figure. Numerical values alongside the colour bar are not reported for practical reasons. The ϵ values within to the nth colour of the colour bar are computed as $\epsilon_n = \epsilon_{min} + (n-2)(\epsilon_{max} - \epsilon_{min})/14$ and $\epsilon_{n+1} = \epsilon_{min} + (n-1)(\epsilon_{max} - \epsilon_{min})/14$, $n = 2, 3, \ldots, 15$.

strongly affected by collisions with the disc's outer edge. This peculiarity has not a physical origin due to pressure forces exerted against a low-density flow colliding with a denser fluid in isothermal conditions. Densities of stream gas and disc's outer edge are indeed both comparable to each other as clearly shown in Fig. 11. However, the collisional momentum exchange between the two flows always occurs throughout the SPH models. But it is far more effective whenever a widening of the spatial resolution length involves far larger dissipations in ASPH models in diluted expanding flows due to the need to collect the assigned number of companions, as also mentioned in Section 3.1. Hence, the morphology of the injected stream is a consequence of the artificial damping related to the h variability. Despite the initial conditions of injection being identical as much as possible, this is inevitably an uncontrollable variable. Different local collimations of the incoming particle flow are involved, together with a larger momentum loss of the stream particles heavily interacting with disc's outer particles.

The third detail regards the better development of mass-density spiral structures, especially in those adaptive disc models which are radially shorter. Even though in adaptive conditions, the number of 40 SPH assigned companions is statistically not so much greater than the 25–30 companions evaluated for the two models working with the same $W_{3,ij}$ and $W_{1,ij}$ Kernels and whose spatial resolution is constant. However, the development of spirals should favour the more radially stretched discs instead of the smaller ones on the tidal truncation radius basis due to secondary star tidal torques (Paczynsky, 1977; Papaloizou and Pringle, 1977; Ichikawa and Osaki, 1992, 1994). Therefore, it is unclear if the counting of only ≈10 more ASPH neighbours could improve so much the integration-interpolation result allowing a better development of the mass-density spirals despite the shorter ASPH disc's radial extension. This opposite stronger evidence should, instead, be related to the discussed evidence regarding the different shapes and collimation of the injected flow in adaptive conditions because even the injection conditions affect the development of spirals.

In an in-depth glance, it is noteworthy to ascertain that a consistent halo of scattered particles towards the outer space exists for the adaptive model working with $W_{1,ij}$, as shown at the bottom-right panel of Fig. 11. In such disc adaptive model, h is statistically the largest, as shown in Fig. 12. Therefore, the scattered halo cannot be attributed to the stronger radial transport activated by the artificial viscosity depending on h (Eq. (B.3)) since a viscous radial transport generates a collective uniform particle flow at the disc's outer edge. Instead, such a scattered halo is due to the greater repulsive action of pressure forces of the many farther neighbours because of the spatial gradients of $W_{1,ij}$ Kernel in Figs. A.40 and A.41. This confirms (Appendix A.2) that, even for the lower γ-values and despite the contemporary appearance of the welcome spirals, the radial profiles of the Kernel and its spatial derivatives incorrectly affect any SPH integrations within the analytic integrals (Eqs. (A.6), and (A.12)) without the analytical compensation $(2\pi r)^{-1}$ in 2D and $(4\pi r^2)^{-1}$ in 3D in the continuum limit (Lanzafame, 2010a, 2018). Without such correction (Appendix A.2), any spurious contribution in the $-\nabla p$, coming from the many farther companions around, leads to scattered particles compromising the disc tightness for gravitational fields slightly prevailing against pressure forces.

The xy plots of the v total velocity distribution in Fig. 13 show no significant differences. This result is expected since the relevance of the gravitational contribution in the momentum equation (Eq. (A.2)) is better highlighted working with lower γ-values. Instead, the evidence of pressure force excesses is shown in the two panels at the bottom of Fig. 14 where larger values of ϵ appear, especially working with $W_{1,ij}$. The ϵ radial profiles in all four disc model xy plots shown in the picture are regular throughout, but those relative to $W_{1,ij}$ are higher.

In adaptive conditions, the increase of the variable smoothing length h could be either physical, because of a flow pressure gradient, or

it could be arbitrary because dictated by the need to count more neighbours. Any increase of the particle spatial resolution length h also leads to an increase of artificial viscosity, involving an excess in the viscous radial transport. A way of regulating this mechanism is its reformulation through a multiplicative term (Balsara, 1995; Monaghan, 1997; Morris and Monaghan, 1997; Read and Hayfield, 2012; Taddei et al., 2017), where the two strategical paths of Eqs. (B.3)–(B.9) can also be mixed. This should also lead to a decrease of both the accretion and the ejection rates from the disc edges, which is the only deficiency of SPH disc modelling claimed by Motl et al. (2017).

According to such suggestions, Fig. 15 displays the xy mass-density maps for four ASPH disc models when using $W_{3,ij}$ (top panels) and using $W_{1,ij}$ Kernels (bottom panels). Artificial viscosity, still expressed by Eq. (B.3), is regulated either by Eqs. ((B.5) and (B.6)) (left-side panels) or by Eqs. ((B.7) - (B.9)) (right-side panels). The outcome does not show significant differences compared to those of the right-side panels of Fig. 11 both on disc structures and on the total number of particles dealing with accretion and ejection rates. This result is the consequence of the fact that in adaptive conditions any significant increase of the variable smoothing length subracts relevance to both softening terms of artificial viscosity as compressions prevail on vorticity. Moreover, the algebra itself of Eqs. (B.3)–(B.9) shows that any relevant increase of h disfavours any correction on the artificial viscosity. More significant results on the mass radial transport can be obtained by tuning the free parameters in Eq. (B.6) or in Eqs. ((B.7) and (B.8)). But this is a topic that is not covered here because the handling of SPH artificial viscosity, also bypassed working with free viscosity Riemann solver algorithms (Parshikov, 1999; Parshikov et al., 2000; Parshikov and Medin, 2002; Inutsuka, 2002; Imaeda and Inutsuka, 2002; Cha and Whitworth, 2003; Cha and Wood, 2016; Molteni and Bilello, 2003; Iwasaki and Inutsuka, 2011; Sugiura and Inutsuka, 2017), is not the root of the main 2D and 3D SPH deficiencies.

A comparison is made between these high compressibility disc models with those working with $W_{erf,ij}$, also considering the refinements of Eqs. ((A.37) and (A.39)) and the flow damping of Eq. (B.41), as it is explained in Section 3.1. The adoption of $W_{erf,ij}$ induces a much slower mass and angular momentum disc's radial transport (Lanzafame, 2010a) despite working with the same artificial viscosity criteria (Eq. (B.3)) adopted for the modelling working with $W_{3,ij}$ and $W_{1,ij}$. Such a reduced radial transport occurs because of the smaller $|\nabla p|$ of the many farther neighbour particles in the numerical summation characterizing the spatial integral (Eq. (A.13)). Therefore, plots of discs working with $W_{erf,ij}$ (with and without SPH refinements), whose damping is attributed to the artificial viscosity formulation, are shown at time 150 instead of 100 since their radial dynamical evolution is slower. In doing so, such disc structures are more comparable with previous non-viscous high compressibility SPH disc models here shown. A slower radial dynamical evolution implies a higher total number of disc particles working with $W_{erf,ij}$ (as it is shown in the two left panels of Fig. 16) and also smaller accretion and ejection rates from disc edges in so far as the mass-transfer rates are comparable. Discs shown in the two left panels of Fig. 16 have a global profile of the outer edge that is more regular and symmetrical than previous disc models and they are free of any spiral pattern in the mass-density distribution up to a time $t \sim 100$. From $t \sim 100$ onwards, they develop less pronounced mass-density spirals (here shown at $t \sim 150$) because of the better cylindrical symmetry. Thus, in both disc modelling on the left of the picture, the goal of getting the tidal truncation radius extension (Paczynsky, 1977; Papaloizou and Pringle, 1977; Ichikawa and Osaki, 1992, 1994) and the consequent development of spiral pattern profiles need an evolutionary time extension involving a much longer computational effort, which can double, if not triple. The further adoption of Eq. (B.41), excluding any artificial viscosity, contributes to the killing of any spiral pattern profile whose kinematics, being non-Keplerian, activates that dissipation mechanism working with $\nabla \cdot \mathbf{v} < 0$ (Eq. (B.38)), still using $\mathcal{K} \approx 2\ 10^3$. This dissipative term effectively keeps the disc to even

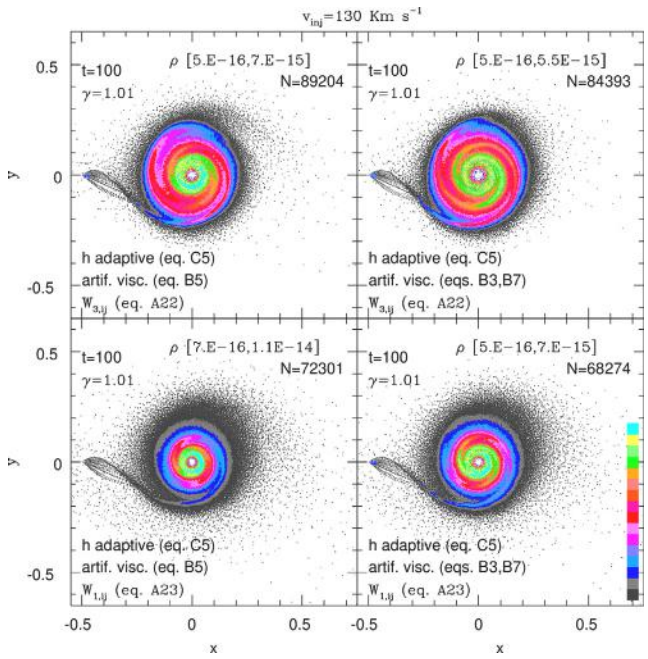

Fig. 15. xy scatter plots in a linear scale of 16 colours of 3D ASPH non-viscous accretion disc models for $W_{3,ij}$ (top panels) and $W_{1,ij}$ Kernels (bottom panels). Colours refer to the dimensionless mass-density ρ. Data identifying the modelling are also reported with references to the Appendices, together with the dimensionless lower and upper ρ values of the colour bar, within the square brackets: $[\rho_{min}, \rho_{max}]$ on top of each panel. Dots in dark grey (bottom of the colour bar) refer to values of $\rho \leq \rho_{min}$. Dots in cyan(top of the colour bar) refer to values of $\rho \geq \rho_{max}$. As for ρ_{min} and ρ_{max}, the computer exponential notation is used instead of the scientific exponential notation. All N particles are also reported in each panel. v_{inj} is reported on top of the entire figure. Numerical values alongside the colour bar are not reported for practical reasons. The ρ values within to the nth colour of the colour bar are computed as $\rho_n = \rho_{min} + (n-2)(\rho_{max} - \rho_{min})/14$ and $\rho_{n+1} = \rho_{min} + (n-1)(\rho_{max} - \rho_{min})/14$, $n = 2, 3, \ldots, 15$.

more Keplerian kinematics, preventing the overall radial extension of the disc's outer edge. Therefore, any external disc expansion, exposed to the gravitational field of the secondary star, is excluded. This can be seen in the two panels on the right of Fig. 16, also showing no relevant differences when working in the XSPH approach. Working with Eq. (B.41), according to the parameters here chosen, the disc's outer edge is permanently hinged in its radial extension showing no outward radial stretching. Particles coming from L_1 are either ejected outwards by collision, or they are enveloped within the torus Keplerian kinematics. This is shown in the two right panels of the picture where only a tenuous outer edge envelope of particles is allowed around the main particle torus.

As regards the particle neighbours statistics, Fig. 17 shows that all integrations are fully significant throughout the four disc models working with $W_{erf,ij}$ up to $4h$ since any integration works with hundreds–thousands of companions. This involves a clear cost of a far longer computational time than the SPH modelling working with $W_{3,ij}$ and $W_{1,ij}$, of the order of 5 times, as long as the total numbers of disc particles are comparable. Throughout the disc models working with $W_{erf,ij}$, in Fig. 17 the little population of particles with a low number of neighbours around within $4h$ refers to either outflowing particles far from the disc or to stream particles. Therefore they are not important as for the disc structure and dynamics.

(r_{xy}, z) plots of the disc modelling of Fig. 11 and the most significant ones of Fig. 16 are shown in Fig. 18. How differently the $W_{erf,ij}$ Kernel works against the other two formulations (either adaptive or not) is undoubtedly displayed. It is also evident how different the radial mass and angular momentum transport is, activated by the two different formulations of dissipation (Eqs. (B.3) and (B.41)) for ideal

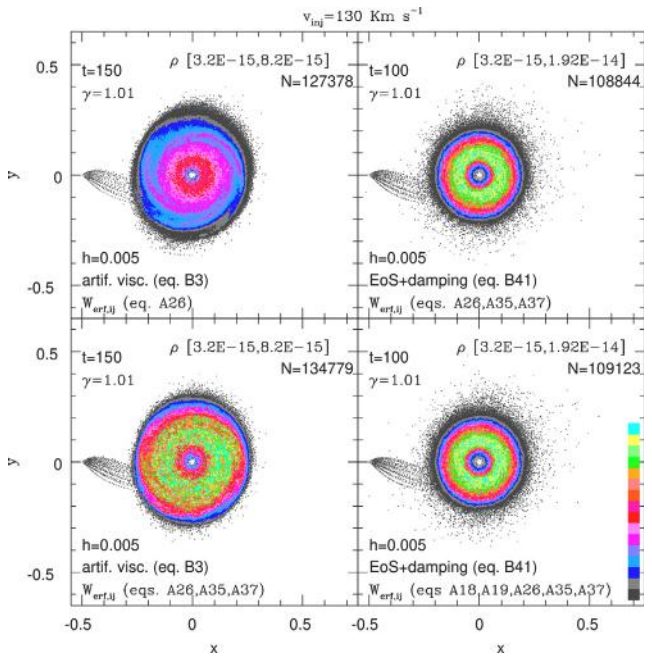

Fig. 16. xy scatter plots in a linear scale of 16 colours of 3D SPH non-viscous accretion disc models for $W_{erf,ij}$. Colours refer to the dimensionless mass-density ρ. Data identifying the SPH modelling are also reported with references to the Appendices, together with the dimensionless lower and upper ρ values of the colour bar, within the square brackets: $[\rho_{min}, \rho_{max}]$ at the top of each panel. Dots in dark grey (bottom of the colour bar) refer to values of $\rho \leq \rho_{min}$. Dots in cyan(top of the colour bar) refer to values of $\rho \geq \rho_{max}$. As for ρ_{min} and ρ_{max}, the computer exponential notation is used instead of the scientific exponential notation. All N particles are also reported in each panel. v_{inj} is reported on top of the entire figure. Numerical values alongside the colour bar are not reported for practical reasons. The ρ values within to the nth colour of the colour bar are computed as $\rho_n = \rho_{min}+(n-2)(\rho_{max}-\rho_{min})/14$ and $\rho_{n+1} = \rho_{min}+(n-1)(\rho_{max}-\rho_{min})/14$, $n = 2, 3, \ldots, 15$.

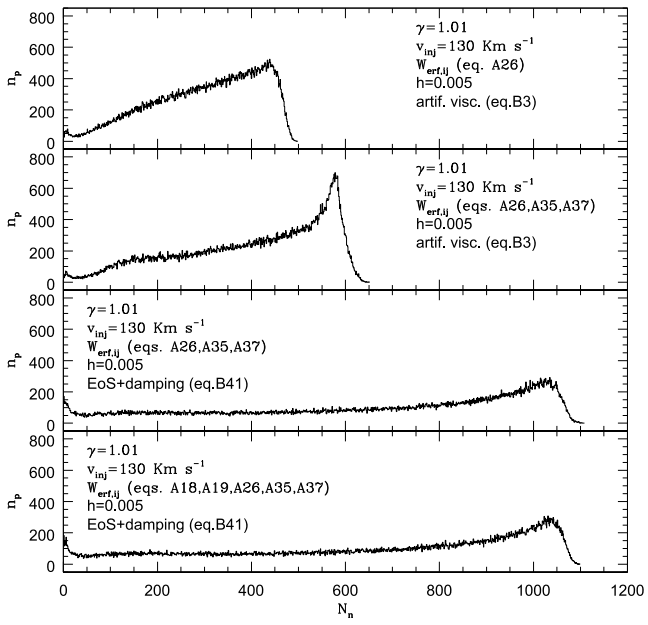

Fig. 17. Histograms showing, for the four SPH $W_{erf,ij}$ models of Fig. 16, the distribution of particles n_p relative to their companions N_n within the radial interpolation extension $4h$.

gases. Although a relationship exists between disc thickness and the rate of mass-transfer, the incorrect pressure forces of the many farther neighbours, emphasized by the increase of h for ASPH models, make discs even too thick. The adoption of low γ-values always allows the development of ideal gas disc structures in an LMCB by reducing the role of repulsive pressure forces. However, the most subtle structures are those of a disc modelling working with $W_{erf,ij}$, which are thinner being free of such shortcomings, even at high mass-transfer rates. Moreover, ideal gas non-viscous discs, deliberately showing slow mass and angular momentum radial transport, can be obtained whenever working with a dissipation ignited by a physical non-viscous damping as discussed in Eq. (B.41).

Figs. 19 and 20 show the xy distributions of the total velocity v and of the thermal energy per unit mass ϵ for the same four disc models of Fig. 16 in a representation of a linear scale of 16 colour. Being $\gamma = 1.01$ lower than that assumed in the previous Subsection, the common radial gradient of speed unites all four models, as also previously shown in Fig. 6. Together with Fig. 13, this is a clear indication that, whatever is γ, the disc kinematics is always controlled by the LMCB primary's gravitational field so that all models converge towards a common structure whatever is the working Kernel – either adaptive or not – as $\gamma \rightarrow 1$.

In non-viscous conditions, the only balance is between gravitational forces and pressure forces as long as the pressure forces have at least a minimum of concreteness. Otherwise, in the SPH framework, the comparison of the Kernel capability in simulating a dissipative radial transport in the non-viscous fluid dynamics is useless because of a too small $\gamma \rightarrow 1$, drastically preventing any role played by the Kernel profile. In such a limit, no pressure involves no gradient pressure and no dissipations at the same time. The radial distribution of ϵ still shows an undoubted envelope component of particles hotter than disc particles at the same r_{xy}, especially for those two disc models on the right panels of the picture by adopting Eq. (B.41) as a mechanism for dissipations. High gas compressibility conditions inevitably lead to thinner disc structures than in lower compressibility. Thus, such envelope particles mainly come from a fraction of the injected flow stream because of the wide opening of the injected flow due to the high speed of mass-transfer from L_1. Therefore, the injected stream particles even rain onto the surfaces of a thin disc, up to short radial distances, involving significant negative values of $\nabla \cdot \mathbf{v}$. The shorter r_{xy}, the harder the particle collisions. Thus, such an overheating is explained by hard collisions, whose dissipation within Eq. (B.41) is undoubtedly significant.

The radial and the vertical distributions of ρ, ϵ and of the total velocity v are essential plots useful in understanding the disc structures obtained by the assumed SPH modelling. Fig. 21 shows the mass-density distributions related to discs of Figs. 11. The presence of the already discussed external halo of particles is further highlighted, detected as an additional contribution tightly close to the inflow flux from L_1. Moreover, the two panels dealing with the ρ radial distributions of the two adaptive disc models also show some external ridge-shaped structures characterizing the spiral-shaped flows at the bottom-left of the picture.

Another peculiarity shown at the two bottom-left panels for the ASPH models is that the lowest values of mass-density in the two spatial distributions are smaller than those relative to their respective models working with the same SPH Kernel and a constant h value. This result is due to the increase of h for low concentration particles for adaptive disc models, as previously shown statistically in Fig. 12, involving a smaller h^{-3} (Eqs. (A.22) and (A.23)). Anyway, the profiles of the radial and vertical distributions of the mass-density for adaptive models compare to those obtained working with a constant h in their general aspects. Their radial undulations are comparable to each other. This result is dictated by two key factors. The first one is the role of a dominant gravitational field in subtracting particles at such very short radial distances, imposing the same decreasing mass-density radial profile. The second one is the pressure forces behaviour, dictated by the Kernel radial profile, having a weak dependence on the statistical number of

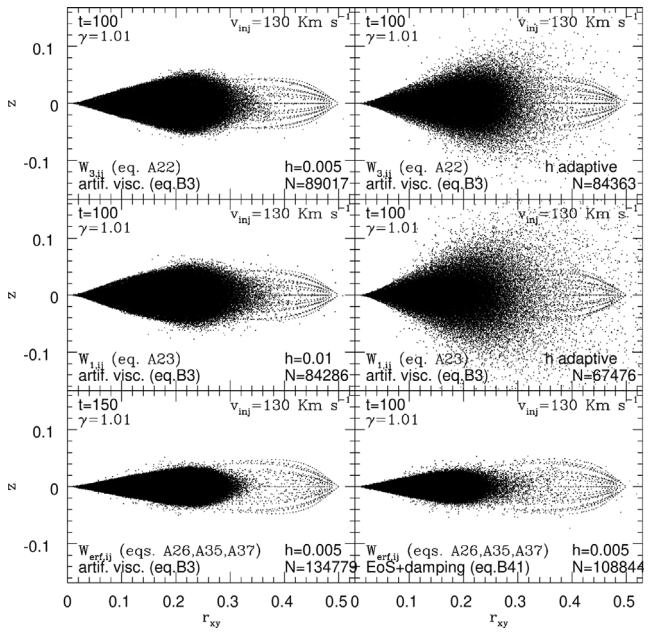

Fig. 18. (r_{xy}, z) plots of disc models of Figs. 11 and of SPH models of 16 working with refinements of Eqs. ((A.37) and (A.39)). All disc modelling data are reported for each panel.

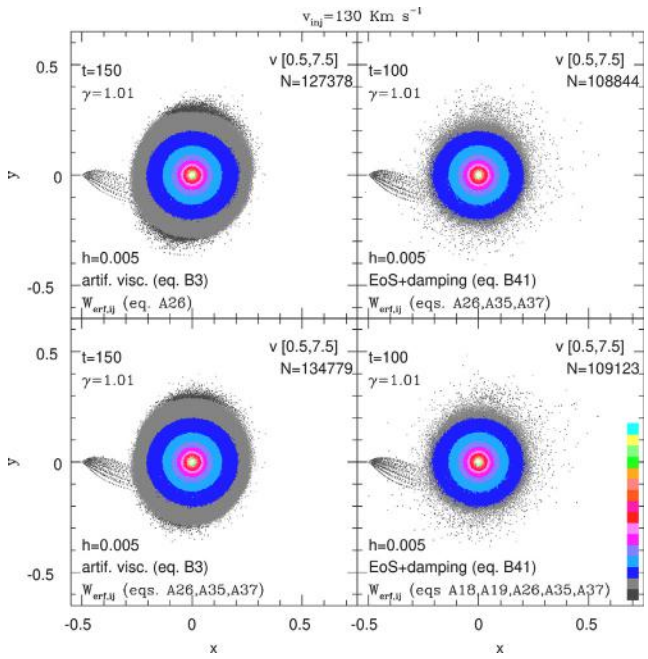

Fig. 19. xy scatter plots in a linear scale of 16 colours of 3D SPH non-viscous accretion disc models of Fig. 16. Colours refer to the dimensionless total velocity v. Data identifying the SPH modelling are also reported with references to the Appendices, together with the dimensionless lower and upper v values of the colour bar, within the square brackets: $[\mathrm{v}_{min}, \mathrm{v}_{max}]$ on top of each panel. Dots in dark grey (bottom of the colour bar) refer to values of $\mathrm{v} \leq \mathrm{v}_{min}$. Dots in cyan (top of the colour bar) refer to values of $\mathrm{v} \geq \mathrm{v}_{max}$. All N particles are also reported in each panel. v_{inj} is reported on top of the entire figure. Numerical values alongside the colour bar are not reported for practical reasons. The v values within to the nth colour of the colour bar are computed as $\mathrm{v}_n = \mathrm{v}_{min} + (n-2)(\mathrm{v}_{max} - \mathrm{v}_{min})/14$ and $\mathrm{v}_{n+1} = \mathrm{v}_{min} + (n-1)(\mathrm{v}_{max} - \mathrm{v}_{min})/14$, $n = 2, 3, \ldots, 15$.

neighbours from a certain threshold onwards. This second factor is better highlighted as soon as the mass and angular momentum radial transport, dictated by the artificial viscosity, drags the mass-density peak towards shorter radial distances.

However, statistically higher ρ values characterize the thicker adaptive disc models with the same Kernel radial profile, despite their smaller total number of particles, within shorter but comparable disc's radial extensions. This means that for both adaptive disc models the particle spatial distributions are far from being uniform. Moreover, the halo particles found in Figs. 11 and 18 are the tenuous components of a much more consistent envelope surrounding the denser spiral patterns of ρ previously shown in Fig. 11. As far as the main radial profiles of ρ are concerned, the two mass-density peaks for $W_{1,ij}$ are both more flattened towards shorter radial distances than those for $W_{3,ij}$. This is a consequence of a more effective action of artificial viscosity due to a larger h: $h = 10^{-2}$ for $W_{1,ij}$ against $h = 5\ 10^{-3}$ for $W_{3,ij}$ and statistically shown in Fig. 12 for their adaptive variants.

Fig. 22 shows the ρ radial and the vertical spatial distributions of inviscid SPH disc modelling, working with $W_{erf,ij}$ for the most significant models of Fig. 16. In intermediate γ-value regime (Section 3.1), the SPH refinements of Eqs. ((A.37) and (A.39)) involve numerical modifications within larger collisional statistical fluctuations. This means that they do not involve appreciable modifications in the disc structure. Instead, working in a low γ-value regime, the same SPH refinements of the above-mentioned equations fully come out. In fact, the mass-density distributions of Fig. 22 for $W_{erf,ij}$ show perceptible differences with each other depending on whether Eqs. ((A.37) and (A.39)) are used or not.

The first two spatial distributions, shown on top panels of Fig. 22, are overall comparable with those shown in Fig. 21, especially for those related to $W_{3,ij}$. Instead, the two panels in the middle of Fig. 22 show quantitative and qualitative differences, although the total numbers of particles of the two discs are comparable to each other at $t = 150$. This means that some differences exist between the two disc structures, despite the two rates of accretion onto the primary compact star being strictly comparable. Such differences in the mass-density distributions come out from a perceptible correction in the continuity and the energy equations through the $\nabla \cdot \mathbf{v}$ terms. Instead, they are scarcely affecting the momentum equations because of the relevance of the gravitational field. So, such differences come out only in high compressibility conditions in the spatial distribution profiles of ρ and ϵ, not in those regarding v.

What is clear, looking at the two panels in the middle of Fig. 22, is that the overall higher mass-density and the disc thinning, both consequent to the adopted compressibility conditions, make the emerging of ρ spiral patterns a bit more difficult, as also confirmed in Fig. 16. What is also important in the two panels at the bottom of Fig. 22 is that the adoption of Eq. (B.41), excluding artificial viscosity (Eq. (B.3)), leads to a non-viscous disc structure which is smaller, thinner, and characterized by a massive steady torus in the bulk. Such a massive torus is surrounded, in turn, by another toroidal envelope having lower ρ values. This structure, here shown at $t = 100$, exists permanently throughout the entire simulation in which, apart from a steady accumulation of the toroidal structure, no other interesting features come out. Thus, a disc structure as planned for strictly non-viscous accretion discs, as described in Lubow and Shu (1975), came out at last.

Figs. 23 and 24 show the radial and the vertical distributions of ϵ for the same disc models of Figs. 21 and 22, respectively. Instead, Figs. 25 and 26 show the radial and the vertical distributions of the total velocity v, of such disc models in the same order. The radial distributions of v are in very good agreement with a strictly Keplerian kinematics only within short radial distances for $r_{xy} \leq 0.1$–0.2. The radial region at $r_{xy} \sim 0.2$ is a small transition zone between shorter radial distances, where a Keplerian kinematics prevails, and longer radial distances where the gravitational field of the secondary star leads to a subkeplerian kinematics. The vertical distributions on the right side show low-velocity components throughout, especially around the disc surfaces at large $|z|$. This suggests that the shearing of subkeplerian flows of the disc superficial components affects even the kinematics

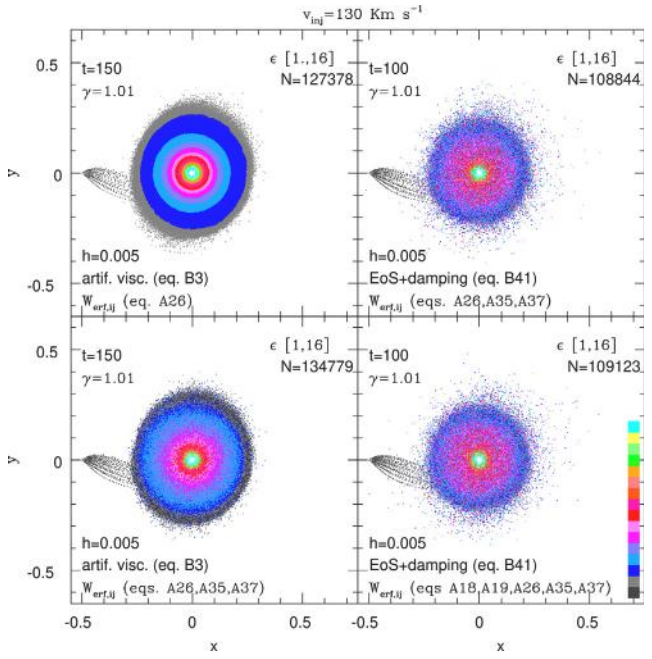

Fig. 20. xy scatter plots in a linear scale of 16 colours of 3D SPH non-viscous accretion disc models of Fig. 16. Colours refer to the dimensionless thermal energy per unit mass ϵ. Data identifying the SPH modelling are also reported with references to the Appendices, together with the dimensionless lower and upper ϵ values of the colour bar, within the square brackets: $[\epsilon_{min}, \epsilon_{max}]$ on top of each panel. Dots in dark grey (bottom of the colour bar) refer to values of $\epsilon \leq \epsilon_{min}$. Dots in cyan (top of the colour bar) refer to values of $\epsilon \geq \epsilon_{max}$. All N particles are also reported in each panel. v_{inj} is reported on top of the entire figure. Numerical values alongside the colour bar are not reported for practical reasons. The ϵ values within to the nth colour of the colour bar are computed as $\epsilon_n = \epsilon_{min} + (n-2)(\epsilon_{max} - \epsilon_{min})/14$ and $\epsilon_{n+1} = \epsilon_{min} + (n-1)(\epsilon_{max} - \epsilon_{min})/14$, $n = 2, 3, \ldots, 15$.

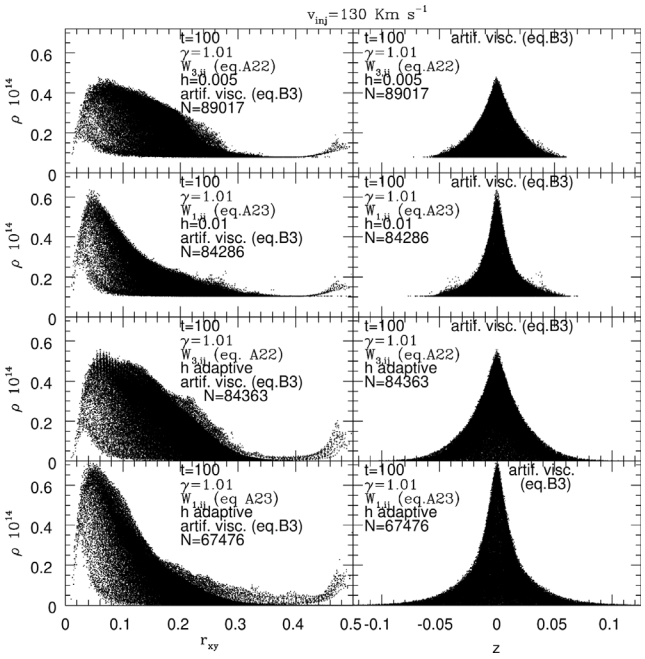

Fig. 21. r_{xy} radial and z vertical distributions of dimensionless values of ρ 10^{14} for accretion disc models of Fig. 11. In each panel some modelling data are reported, together with references (in the Appendices) regarding the dissipation. v_{inj} is reported on top of the entire figure.

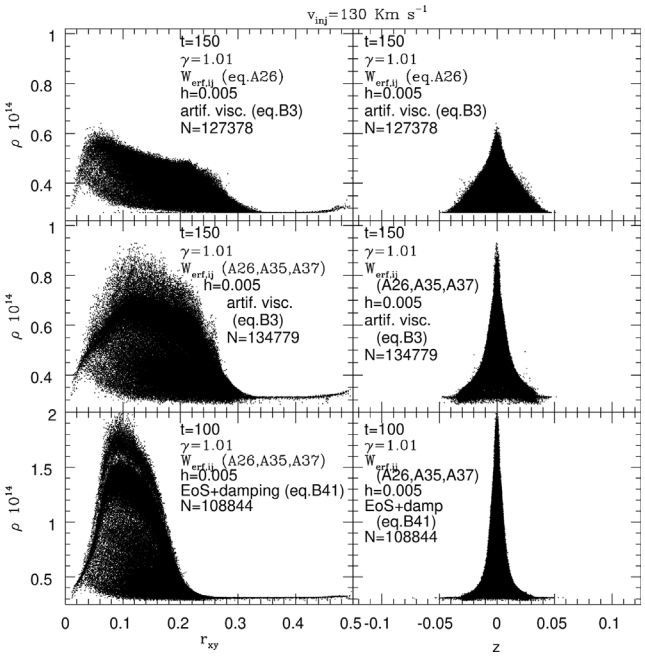

Fig. 22. r_{xy} radial and z vertical distributions of dimensionless values of ρ 10^{14} for the most significant accretion disc models of Fig. 16. In each panel some modelling data are reported, together with references (in the Appendices) regarding both the numerical normalization and the dissipation. v_{inj} is reported on top of the entire figure.

of underlying disc's layers immediately above and below the orbital plane at $z \approx 0$ whenever high compressibility conditions are adopted. Instead, at shorter radial distances, the stronger gravitational field of the primary compact star regains its leading role imposing Keplerian kinematics, quenching any damping activated by a $\nabla \cdot \mathbf{v} < 0$. Therefore a standard model profile is no longer strictly fitted. If this is inconsistently minimal for the higher γ-values and is not decisive, it stands out more clearly by looking at Figs. 23 and 24. Moreover, looking at Fig. 23 from $r_{xy} \approx 0.1$ inwards, the disc model working with $W_{1,ij}$ and $h = 10^{-2}$ shows a greater heating than that working with $W_{3,ij}$ and $h = 5\ 10^{-3}$, due to the larger artificial viscosity because of the larger h. The same result comes out by looking at the plots referring to the two adaptive disc models. Being the particle number density larger than those relative to the $\gamma = 1.1$ models discussed in Section 3.1 and, consequently, being their collisional rate higher, now such overheating stands out more clearly.

With the simpler adoption of $W_{erf,ij}$, without any numerical refinement, and with the adoption of artificial viscosity, both the spatial distributions of ϵ (top panels) do not show relevant features compared to those working with the other two Kernels, with the only exception of a disc thickness reduction. Instead, some heating appears on the disc surfaces for the disc model working with $W_{erf,ij}$, in which a refinement of SPH is applied according to Eqs. ((A.37) and (A.39)) (middle panels). This comes out by looking not only at the ϵ radial profile fluctuations but also at the two symmetrical bumps appearing on the right panel regarding its vertical distribution in the middle of Fig. 24. Another important detail shown in the same two panels in the middle of Fig. 24 is that a thermal discrepancy exists in the populations of particles at the same spatial coordinates. This shows that in conditions of high speed of mass-transfer, the component of disc particles on the orbital plane at $z \approx 0$ still keeps its ϵ radial profile. At the same time, collisions of cold stream particles of the wide flow coming from L_1 (due to high-speed injection), with particles on disc surfaces, determine some sort of vertical stratification of ϵ. Some superficial heating indeed appears together with colder disc stream particles, whilst the disc particles at the lowest $|z|$ are not involved. This peculiarity does not appreciably come out in lower compressibility conditions because of the greater

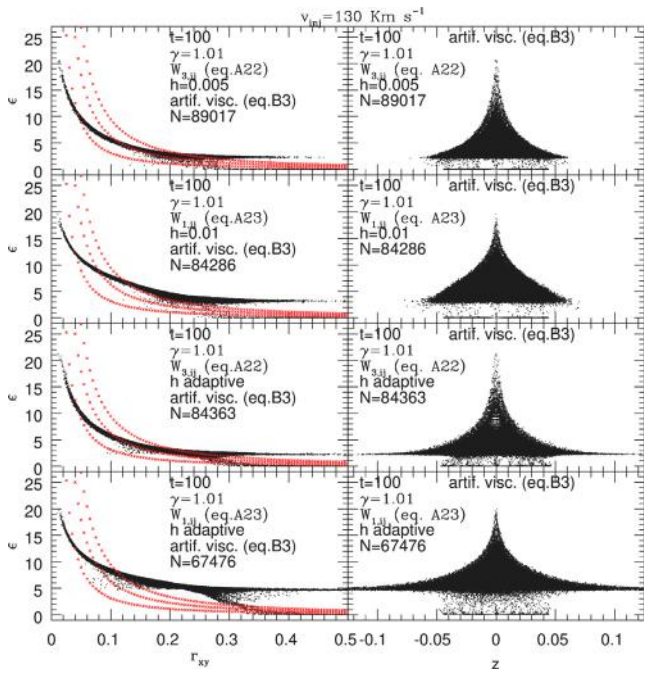

Fig. 23. r_{xy} radial and z vertical distributions of dimensionless values of ϵ for the accretion disc models of Fig. 14. In each panel some modelling data are reported, together with references (in the Appendices) regarding both the numerical normalization and the dissipation. v_{inj} is reported on top of the entire figure. In the left-side panels, regarding the radial distribution, some profiles in red are also shown for comparison, each relative to a $\epsilon \approx S r_{xy}^{-3/2}$ profile, whose $S = 0.1$, 0.2 and 0.3.

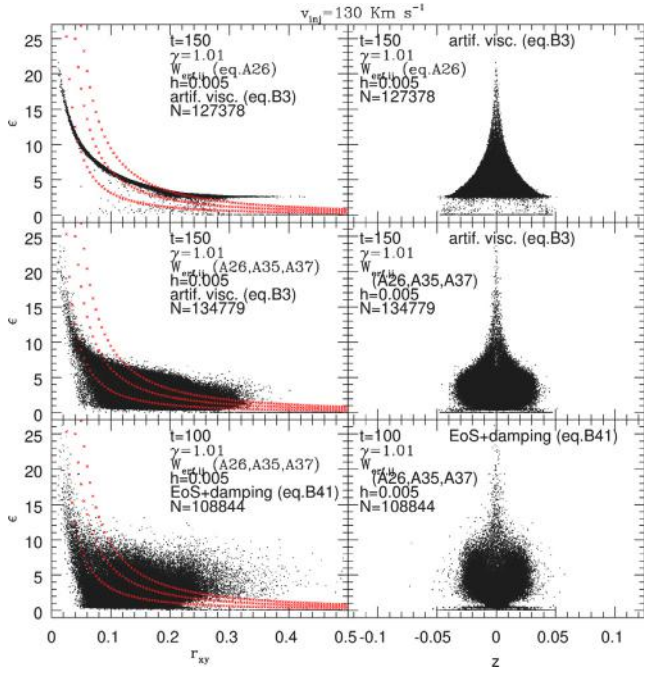

Fig. 24. r_{xy} radial and z vertical distributions of dimensionless values of ϵ for the most significant accretion disc models of Fig. 20. In each panel some modelling data are reported, together with references (in the Appendices) regarding both the numerical normalization and the dissipation. v_{inj} is reported on top of the entire figure. In the left-side panels, regarding the radial distribution, some profiles in red are also shown for comparison, each relative to a $\epsilon \approx S r_{xy}^{-3/2}$ profile, whose $S = 0.1$, 0.2 and 0.3.

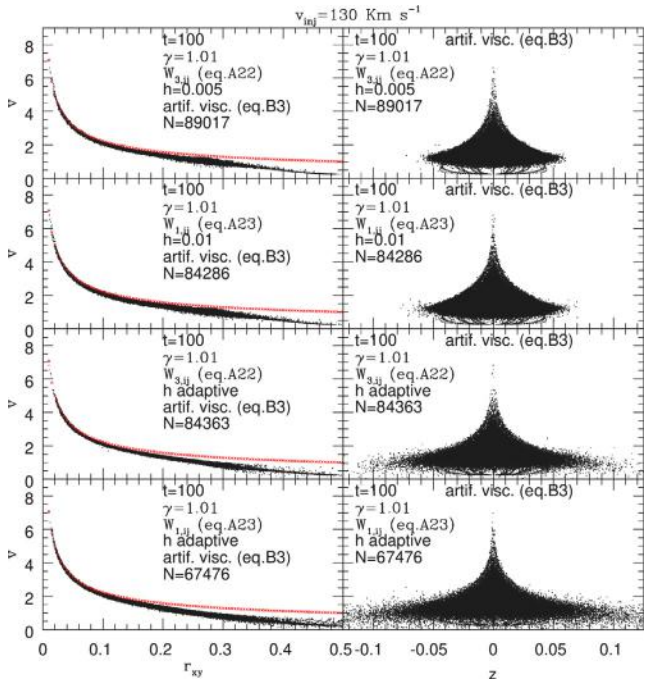

Fig. 25. r_{xy} radial and z vertical distributions of dimensionless values of v for accretion disc models of Fig. 13. In each panel some modelling data are reported, together with references (in the Appendices) regarding both the numerical normalization and the dissipation. v_{inj} is reported on top of the entire figure. In the left-side panels, regarding the radial distribution, some profiles in red are also shown for comparison, each relative to the Keplerian kinematics profile.

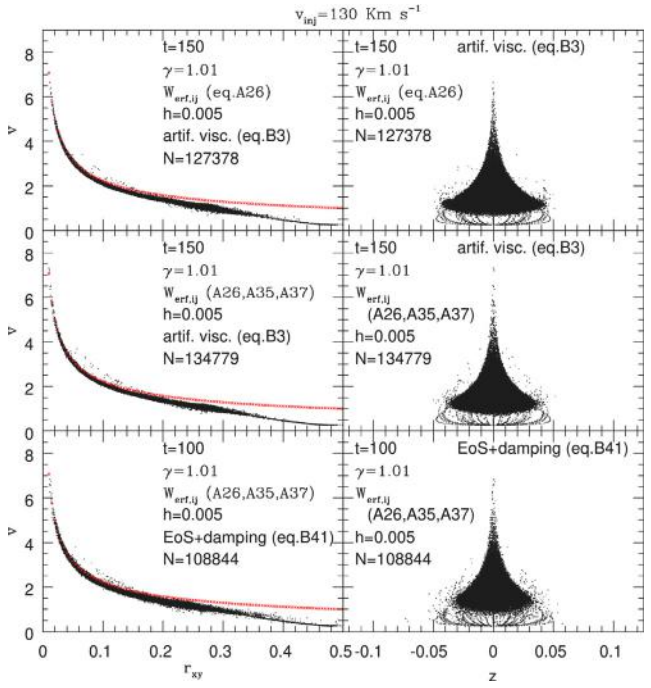

Fig. 26. r_{xy} radial and z vertical distributions of dimensionless values of v for the most significant accretion disc models of Fig. 19. In each panel some modelling data are reported, together with references (in the Appendices) regarding both the numerical normalization and the dissipation. v_{inj} is reported on top of the entire figure. In the left-side panels, regarding the radial distribution, some profiles in red are also shown for comparison, each relative to the Keplerian kinematics profile.

disc thickness preventing such a huge rain of stream flow particles onto the disc surfaces, even working with $W_{erf,ij}$. Therefore, such a vertical stratification of ϵ has only a geometric reason within a collisional frame. This scenario further characterizes the spatial profiles of disc models working with $W_{erf,ij}$, using Eqs. ((A.37) and (A.39)) and also adopting Eq. (B.41) instead of artificial viscosity, shown at the bottom panels of Fig. 24. Thus, disc models working with $W_{3,ij}$ and $W_{1,ij}$ show a radial profile not strictly fitting a Keplerian profile. Instead, disc model working with $W_{erf,ij}$ and Eqs. ((A.37) and (A.39)) and the damping of Eq. (B.41), have a radial profile where the thermal vertical structure shows collisional discrepancies from the mere non-collisional standard model profile. Throughout such ϵ radial profiles, a disc standard model profile for $S \sim 0.1 - 0.2$ could still be attributed, but for statistical purposes only.

Undoubtedly, any collisional modelling of shear flows inevitably leads to local heating and, consequently, to a subkeplerian disc kinematics. This means that the local thermal energy could be comparable to or even greater than that relative to the $z \approx 0$ areas along the vertical column z in high mass-transfer conditions. This unavoidably implies that high rates of mass-transfer could play a fundamental role in the vertical distribution of specific thermal energy.

3.3. Steady toroidal accretion discs in close binaries

The first indications of the existence of a steady toroidal ring in the non-viscous accretion discs are reported by Lubow and Shu (1975) and Frank et al. (2002) in their conceptual accretion disc modelling. Inoue (2021) recently proposed a non-collisional disc modelling for Low-Mass X-ray Binaries (LMXRB), characterized by an accretion flow along the disc middle plane coming from a steady toroidal ring, together with another colder and subkeplerian flow, enveloping the first. Unfortunately, that non-collisional modelling, is also free of any dependence on the mass-transfer rate from L_1, affecting the disc thickness. Even other authors (Churazov et al., 2001; Díaz Trigo et al., 2006; Galis, 2007; Inoue, 2022) highlighted that their observational study converges towards a disc, a torus or an envelope or a mix of them.

Notwithstanding the vertical heating and the cold component characterize our results, especially for the vertical and the radial distributions of ϵ, this overall and complex picture is consistent with conclusions drawn in this paper, even considering that the disc SPH models are fully collisional.

4. SPH turbulent viscous disc modelling in LMCBs: the two roles of the bulk and shear viscosities

As for the viscous 3D accretion disc modelling in the LMCBs, it is worth noting that all disc features discussed using Eq. (D.14) in Lanzafame (2015) were comparable to those obtained working with Eq. (D.9) (Shakura, 1973; Shakura and Sunyaev, 1973). That comparison were limited to the mere shear viscosity counterpart for the sake of simplicity, still working with $W_{3,ij}$, $h = 5\ 10^{-3}$ and adopting the artificial viscosity (Eq. (B.3)). Instead, the disc modelling discussed in this Section works with $W_{erf,ij}$, together with the numerical refinements of Eqs. ((A.37) and (A.39)) and the non-viscous damping of Eq. (B.41). Hence, artificial viscosity is no longer used. Moreover, Eq. (D.13) is adopted instead of Eq. (D.14) for the 3D Navier–Stokes viscous fluid dynamics, even activating the bulk viscosity coming from the term ζ in Eq. (A.14). The smoothing length $h = 5\ 10^{-3}$ is unchanged. In doing so, a formulation of viscosity comparable to that of Prandtl (1925) is used in 3D, deliberately distancing from any formulation like that of Shakura (1973) and Shakura and Sunyaev (1973). This choice is significant since Eq. (D.9) should be strictly adopted in Keplerian kinematic conditions either for 2D discs or 3D thin discs in hydrostatic vertical equilibrium conditions.

The first task is to empirically find the lowest $\mathcal{M}$ value in Eq. (D.13) able to develop a statistically significant and bound accretion disc

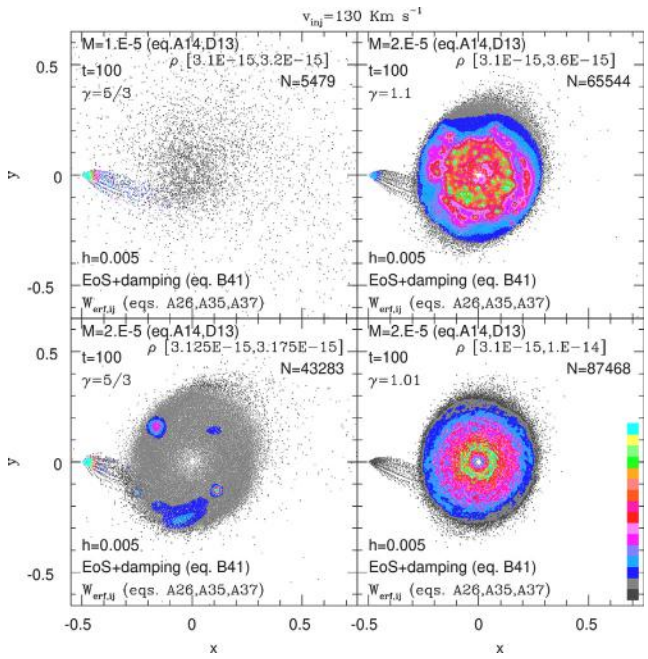

Fig. 27. xy scatter plots in a linear scale of 16 colours of 3D SPH viscous accretion disc models for $W_{erf,ij}$. Colours refer to the dimensionless mass-density ρ. Data identifying the SPH modelling are also reported with references to the Appendices, together with the dimensionless lower and upper ρ values of the colour bar: $[\rho_{min}, \rho_{max}]$ at the top of each panel. Dots in dark grey (bottom of the colour bar) refer to values of $\rho \leq \rho_{min}$. Dots in cyan(top of the colour bar) refer to values of $\rho \geq \rho_{max}$. As for ρ_{min} and ρ_{max}, the computer exponential notation is used instead of the scientific exponential notation. All N particles are also reported in each panel. v_{inj} is reported on top of the entire figure. Numerical values alongside the colour bar are not reported for practical reasons. The ρ values within to the nth colour of the colour bar are computed as $\rho_n = \rho_{min} + (n-2)(\rho_{max} - \rho_{min})/14$ and $\rho_{n+1} = \rho_{min} + (n-1)(\rho_{max} - \rho_{min})/14$, $n = 2, 3, \ldots, 15$.

structure within the primary's gravitational potential well for $\gamma = 5/3$. In doing so, any lower γ-value will always ensure the development of a statistically significant disc structure around the low-mass primary star here considered. Such a value corresponds to $\mathcal{M} \approx 2 \cdot 10^{-5}$, obtained in less than half orbital period of flow evolution from time $t = 0$ through dedicated tests. Larger values for $\mathcal{M}$ lead to unrealistic nonlinear viscous heating since $\nu \propto \epsilon^{1/2}$ (Eq. (D.13)), while the bulk viscosity could be significant in some circumstances because it is a function of $\nabla \cdot \mathbf{v}$. Certainly, any stronger gravitational field of the primary star will involve larger $\mathcal{M}$ values.

Fig. 27 shows xy plots of the physically viscous accretion disc of the semi-detached LMCB discussed in Section 2. The linear scale of 16 colours refers to the ρ mass-density distribution. Three gas compressibilities are considered, dictated by the γ-value: $\gamma = 5/3$ (left panels), $\gamma = 1.1$ (top-right panel) and $\gamma = 1.01$ (bottom-right panel). $\mathcal{M} = 10^{-5}$ (at the top-left panel) is a value still too small to allow to the gravitational and physically viscous forces the development of a statistically populated accretion disc against pressure forces for $\gamma = 5/3$, as described in Frank et al. (2002) (caption of Fig. 5.21, pag 143). For this reason, the disc viscous structure looks like as physically inviscid. Instead a value of $\mathcal{M} = 2\ 10^{-5}$ is enough to develop a statistically significant $\gamma = 5/3$ low compressibility disc structure, as shown looking at the bottom-left panel in the same picture.

For $\mathcal{M} = 2\ 10^{-5}$, the accretion disc structures show three very different behaviours according to the assumed value of γ. This is an aspect that is evident for LMCBs, where the roles of stellar masses, their mutual spatial radial separation, and γ are significant. Accretion disc flows indeed converge towards high compressibility structures by assuming an ever-increasing relevance to the primary star gravitation.

The accretion disc mass-density structure shown at the bottom-left panel for $\gamma = 5/3$ would be homogeneous overall, perhaps with a

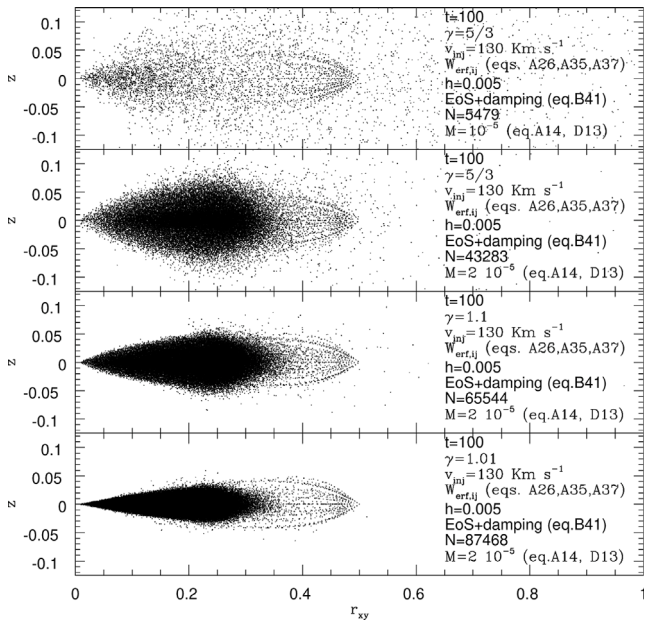

Fig. 28. (r_{xy}, z) plots for models of Fig. 27. All disc modelling data are reported for each panel.

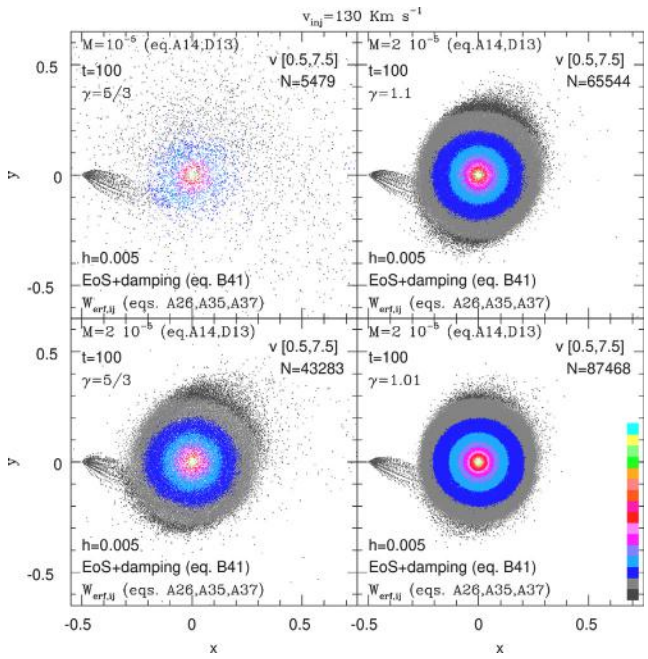

Fig. 29. xy scatter plots in a linear scale of 16 colours of 3D SPH non-viscous accretion disc models of Fig. 27. Colours refer to the dimensionless total velocity v. Data identifying the SPH modelling are also reported with references to the Appendices, together with the dimensionless lower and upper v values of the colour bar, within the square brackets: $[\mathrm{v}_{min}, \mathrm{v}_{max}]$ on top of each panel. Dots in dark grey (bottom of the colour bar) refer to values of $\mathrm{v} \leq \mathrm{v}_{min}$. Dots in cyan (top of the colour bar) refer to values of $\mathrm{v} \geq \mathrm{v}_{max}$. All N particles are also reported in each panel. v_{inj} is reported on top of the entire figure. Numerical values alongside the colour bar are not reported for practical reasons. The v values within to the nth colour of the colour bar are computed as $\mathrm{v}_n = \mathrm{v}_{min} + (n-2)(\mathrm{v}_{max} - \mathrm{v}_{min})/14$ and $\mathrm{v}_{n+1} = \mathrm{v}_{min} + (n-1)(\mathrm{v}_{max} - \mathrm{v}_{min})/14$, $n = 2, 3, \ldots, 15$.

glimmer of spirals, considering only shear viscous forces (Lanzafame et al., 2006; Lanzafame, 2008) inducing a subkeplerian radial velocity component. However, dissipative terms also working with $\nabla \cdot \mathbf{v}$ in the EoS (Eq. (B.41)) and in the bulk viscosity, kill any non-Keplerian kinematics, according to the physical relevance numerically assigned to their coefficients. In this paper the physical relevance of the bulk viscosity terms is comparable to that of the shear viscosity terms, being $\mathcal{M} = 2\ 10^{-5}$ for both. The greater the bulk viscosity, the stronger the formation of clumps wherever a stochastic number density increase makes the viscous forces stronger through the heating due to a local higher collisional rate in low compressibility conditions, even though any autogravitation is excluded. This occurs mainly in the outer disc areas where a lower temperature and higher discrepancies of the local flow speed make viscous forces significant compared to pressure forces and gravitation. In this regard, it is useful to point out that $\nu \propto \epsilon^{1/2}$ (according to Eq. (D.13)) whilst $p \propto (\gamma - 1)\epsilon$, although their spatial derivatives must be considered in a complex nonlinear scenario. Such a meticulous confrontation of forces is due to the low compressibility pressure forces activating greater spatial variations of the velocity and consequently activating stronger viscous forces especially if a bulk viscosity is considered. Then, the further viscous heating nonlinearly increases the specific thermal energy, and so on. This implies that in the innermost disc areas pressure forces prevail on the viscous ones not only because of the high temperature, but also thanks to the gravitational force imposing the Keplerian kinematics and consequently quenching the bulk viscosity activated by $\nabla \cdot \mathbf{v}$. However, the combination of gravitational and shear viscous forces limits any relevant outward flow expansion. Instead, in the colder outer disc areas, viscous forces could be significant against pressure forces. From the observational point of view, there is no clear evidence of the existence of these bound structures within accretion discs in LMCBs, probably because $\gamma = 5/3$ does not correspond to the best choice since the high emissivity of these accretion discs decreases its value. However, it is noteworthy that in other contexts, like star-forming regions of low-mass stars, where a high γ could be reasonable, the formation of solar-like planetary systems is a known reality.

The top-right panel of Fig. 27 shows the xy map of the mass-density ρ in its appropriate linear scale of 16 colours when adopting $\gamma = 1.1$. In this situation of intermediate γ-values, large turbulent flow structures exist since both the gravitational and the viscous forces better keep together large structures against the repulsive action of pressure forces. In this situation, any shadow resembling the toroidal ring characterizing the non-viscous accretion disc structure is missing, and random mass-density peaks are visible in the middle of the disc bulk. This is the most complicated disc structure because of the lack of a clear prevalence between viscous and pressure forces. It is intermediate between a high compressibility disc structure characterized by large radial shell structures, and a uniform low compressibility disc structure, even including some clumps in the disc bulk. This means that the lower the flow compressibility, the farther the flow clumps from the central star. However, this topic should need an in-depth study by using more γ-values within the range of intermediate-low compressibilities as long as the compact primary is a low-mass star.

The bottom-right panel of the same figure shows the xy map of ρ in its most appropriate linear scale of 16 colours when adopting $\gamma = 1.01$. Despite the lack of any trace of a steady toroidal ring in its native position throughout the disc dynamic evolution, a global structure showing mass-density shells appears. The decrease of ρ values close to the primary star towards $r_{xy} \to 0$ could have two interpretations. The first one is that it is due to the physically viscous transport of accreting particles, acting together with the voiding action due to the dominant gravitational attraction at short radial distances. The second one is that the ρ-peak at short distances is a toroidal ring, pulled there by the viscous mass radial transport. The two interpretations do not exclude each other. Another relevant aspect is that each mass-density shell is far from being uniform since smaller stretched clumps appear. In this case, despite the intermediate spatial resolution, it is shown the shear stripping of angular momentum forces on contiguous fluid portions along the azimuthal direction against the shear viscous forces. In such a force balance, bulk viscous forces are excluded because of the prevailing Keplerian kinematics at such short radial distances.

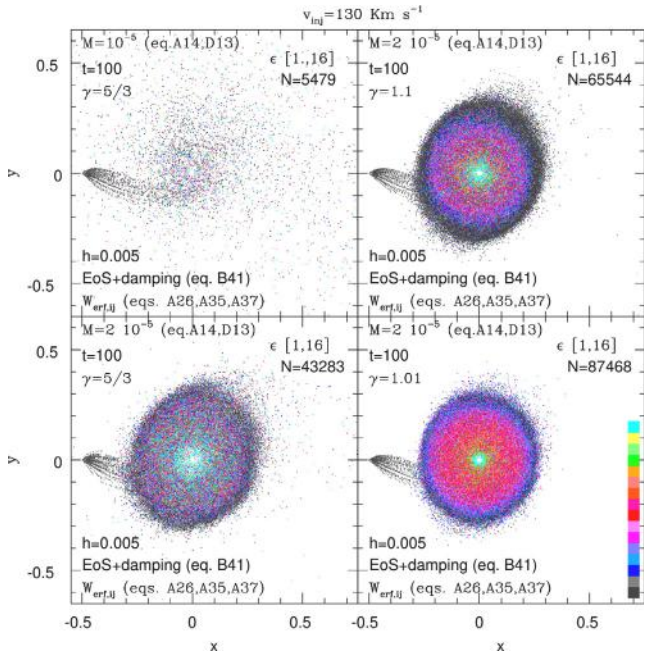

Fig. 30. xy scatter plots in a linear scale of 16 colours of 3D SPH non-viscous accretion disc models of Fig. 27. Colours refer to the dimensionless thermal energy per unit mass ϵ. Data identifying the SPH modelling are also reported with references to the Appendices, together with the dimensionless lower and upper ϵ values of the colour bar, within the square brackets: $[\epsilon_{min}, \epsilon_{max}]$ on top of each panel. Dots in dark grey (bottom of the colour bar) refer to values of $\epsilon \leq \epsilon_{min}$. Dots in cyan (top of the colour bar) refer to values of $\epsilon \geq \epsilon_{max}$. All N particles are also reported in each panel. v_{inj} is reported on top of the entire figure. Numerical values alongside the colour bar are not reported for practical reasons. The ϵ values within to the nth colour of the colour bar are computed as $\epsilon_n = \epsilon_{min} + (n-2)(\epsilon_{max} - \epsilon_{min})/14$ and $\epsilon_{n+1} = \epsilon_{min} + (n-1)(\epsilon_{max} - \epsilon_{min})/14$, $n = 2, 3, \ldots, 15$.

Therefore, the conclusion coming out from the three compressibility viscous modelling is the following. Given that the gravitational field is dominant at short radial distances, viscous forces are effective throughout the disc as a radial transport mechanism engine whatever the flow compressibilities. The gravitational field dictates prevailing Keplerian kinematics killing any physical property activated by $\nabla \cdot \mathbf{v}$, excluding the disc's inner edge where free fall kinematics is considered. However, while shear viscous forces work everywhere, bulk viscous forces are effective only in the strictly non-Keplerian disc's outer areas or wherever is a flow compression or rarefaction in the velocity field. The balance between pressure forces against viscous forces favours one or the other according to the combination of gas compressibility and temperature in a mathematically and physically nonlinear frame of cause and effect around a low-mass star. Such a combination favours the formation of viscous flow clumps in some circumstances. Such flow clumps occur mainly because of the role of the bulk viscosity and the lower the gas compressibility, the longer their radial distance. As a consequence, increasing the gas compressibility by assigning ever-smaller γ-values, disc structures show smaller and smaller clumps at ever-shorter radial distances. In the disc's innermost areas, the shear viscous forces compete against the ever-more dominating angular momentum forces trying to impose rigid rotational kinematics against a Keplerian one. Instead, viscous and gravitational forces compete against pressure forces in the colder outer disc regions providing large uniform circular flows, under permission of the external boundary conditions.

Unfortunately, in intermediate spatial resolutions, it is impossible to clarify if swirling kinematics exists within flow clumps, targeting them as turbulent eddies interacting with the angular momentum transport, as claimed by Kley et al. (1993) in protostellar discs.

The representation of the four viscous discs of Fig. 27 in the cylindrical coordinate (r_{xy}, z) is shown in Fig. 28. At time $t = 100$ the radial extensions of the three discs working with $\mathcal{M} = 2\ 10^{-5}$ are comparable with each other. This means that $t = 100$ is a time long enough to ensure the maximum radial extension of discs. Of course, such a maximum extension is achieved first by the $\gamma = 5/3$ flow because of its lower compressibility. The disc angular thickness for $\gamma = 5/3$, as shown in the second panel, is almost double compared to the other two viscous discs shown in the other two panels below adopting the same $\mathcal{M} = 2 \cdot 10^{-5}$. Instead, any attribution regarding a disc angular thickness amplitude is improper for $\gamma = 5/3$ with $\mathcal{M} = 10^{-5}$. This means that $\mathcal{M} \approx 2\ 10^{-5}$ is suitable to obtaining physical viscous forces not prevailing over gravitational and pressure forces, but significant to allow a flow turbulence. In this regard, it is always useful to remember that the ability to develop turbulence depends on the ratio of forces between the viscous forces and the other forces. Whenever viscous forces strongly prevail, no turbulence is developed. However, if viscous forces are negligible against pressure forces, any free-edge flow expands without limit as long as the gravitational field is weak. Among these, the pressure forces explicitly depend on the compressibility of the gas and therefore depend on the choice made on γ. This detail also come out by looking at the angular openings of $\gamma = 1.1$ and $\gamma = 1.01$ viscous discs which are comparable to those non-viscous of Figs. 5 and 18 working with the same interpolation Kernel. The further viscous thinning is, indeed, very tiny. It is worth noting that the particle spatial distribution is much more diluted at the larger $|z|$ values, and this is a detail emerging especially for the higher γ model, as it happened for the intermediate compressibility non-viscous disc models. This implies that viscous forces are not prevailing on the gas pressure forces, still confirming the success of the assumed choices in avoiding an excessive action of viscosity.

The xy scatter plot maps of the total velocity v and of the specific thermal energy ϵ are shown in Figs. 29 and 30, respectively. It is worth noting that the radial distributions of v in these xy maps are statistically comparable to each other and are also comparable with those referring to the previous non-viscous modelling. This conclusion is supported by the fact that not only the colour distributions are strictly comparable to each other, but also that the minimum and maximum values of v referring to the colour scale on each panel are the same. However, what is also interesting is that such radial profiles are not significantly affected whatever the mass-density distributions. This means that, being ρ uniform or not, axisymmetric or not, the additional viscous radial transport implies significant but small variations on v whose Keplerian–subkeplerian kinematics is controlled by the gravitational field. As for the second picture, regarding the xy maps of the specific thermal energy ϵ, a radial gradient basis is visible, especially for the lower γ-values, mainly characterizing the low $|z|$ locations on the disc orbital plane. To such disc orbital plane component, a second component also exists, whose ϵ values can be relevant. Of course, since these pictures refer to the entire population of particles, their vertical stratification cannot be distinguished, as seen from the top along the z axis.

The inspection of the radial and the vertical distributions of ρ, ϵ, and v allows a further understanding of how the adopted turbulent physical viscosity works, in its shear and bulk components. Such plots are respectively shown in Figs. 31–33, also showing the spatial distributions obtained for $\gamma = 5/3$, whose non-viscous counterparts are not displayed because of their irrelevance. Therefore, comparisons to the non-viscous counterparts will be made referring to Figs. 8, 9 and 10 as far as $\gamma = 1.1$ is concerned and to Figs. 22, 24 and 26 as for $\gamma = 1.01$.

The two top panels in Fig. 31 refer to the mass-density spatial distributions of the low compressibility viscous disc model whose $\gamma = 5/3$. A rather flat distribution of low ρ values is detected throughout such disc model, both at small and at large radial distances r_{xy}, as well as at high $|z|$. This, of course, is the main feature of the low compressibility disc modelling whenever the z component of the gravitational field does not strongly prevail on pressure forces. Mass-density clumps are identified by ρ-peaks around $r_{xy} \approx 0.18$ - 0.3 together with some mass-density ridges. Since these features are missing in the vertical distribution, this

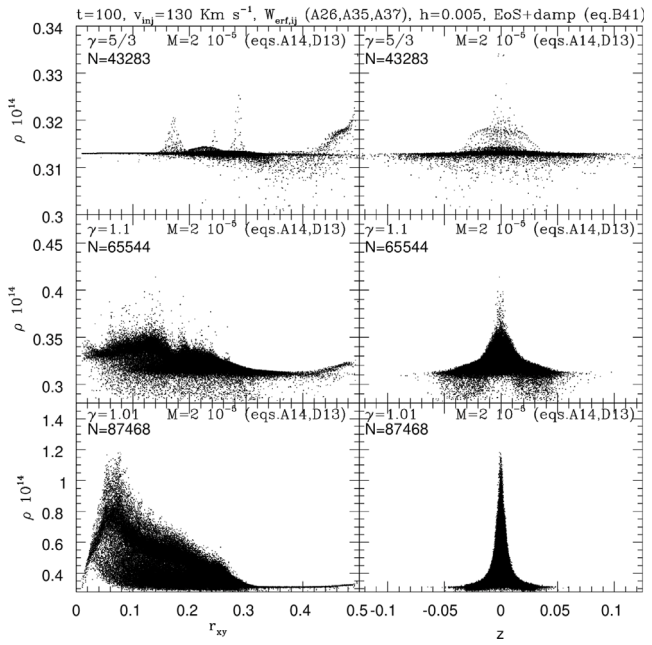

Fig. 31. r_{xy} radial and z vertical distributions of dimensionless values of ρ 10^{14} for the most significant accretion disc models of Fig. 27. In each panel some modelling data are reported, together with references (in the Appendices) regarding both the numerical normalization and the dissipation. Other common modelling data are reported on top of the entire figure.

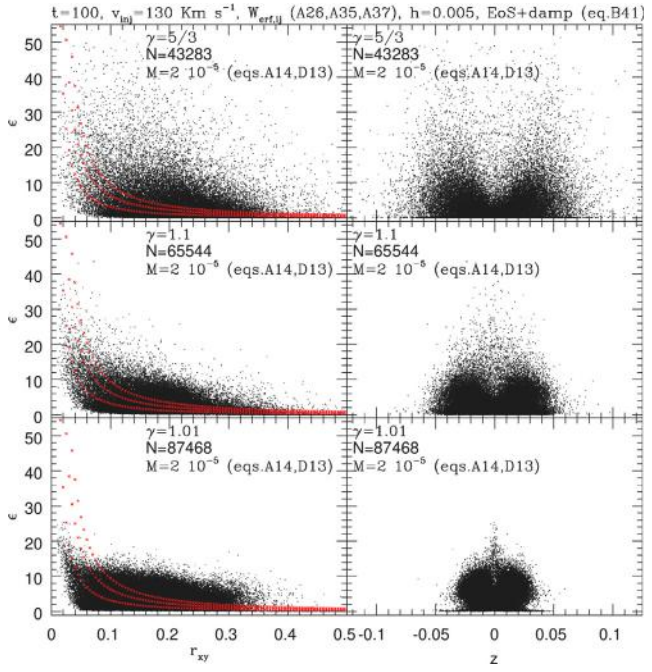

Fig. 32. r_{xy} radial and z vertical distributions of dimensionless values of ϵ for the most significant accretion disc models of Fig. 30. In each panel some modelling data are reported, together with references (in the Appendices) regarding both the numerical normalization and the dissipation. Other common modelling data are reported on top of the entire figure.

means that such clumps are arranged in mirror symmetry concerning the xy orbital plane. The panels in the middle show the ρ spatial distributions of $\gamma = 1.1$ viscous modelling, whose general aspects compare to those shown in the 3rd couple of panels of Fig. 8, referring to the SPH non-viscous counterpart working with artificial viscosity

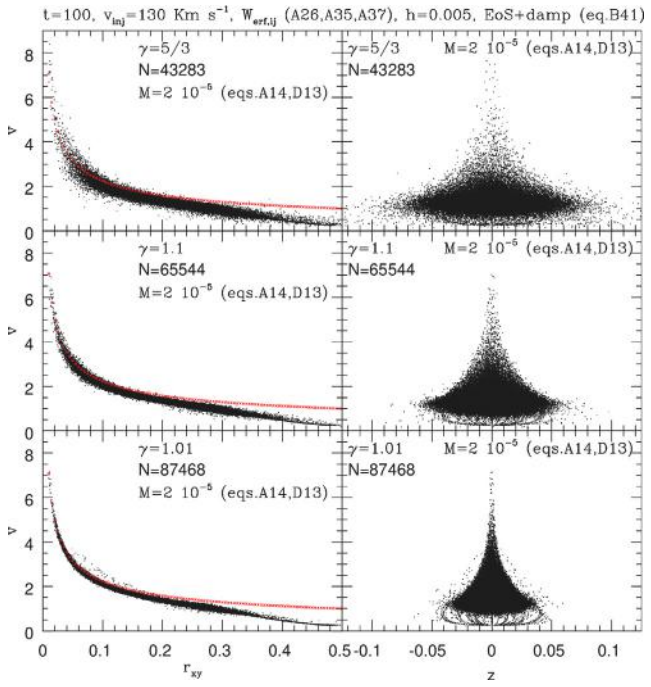

Fig. 33. r_{xy} radial and z vertical distributions of dimensionless values of v for the most significant accretion disc models of Fig. 29. In each panel some modelling data are reported, together with references (in the Appendices) regarding both the numerical normalization and the dissipation. Other common modelling data are reported on top of the entire figure.

(Eq. (B.3)). This means that any particle approaching, as the mechanism activating artificial viscosity for the handling of shocks, works for the non-viscous fluid dynamics both as a bulk and as a shear real viscous damping (Okazaki et al., 2002). This suggests that it is improper the attribution of an SPH non-viscous modelling to fluid dynamics including the Lagrangian formulation of artificial damping which is also excessive whenever h increases. For the intermediate compressibility viscous disc model, any turbulent aspect, shown in the top-left panel of Fig. 27, is not visible as for the ρ vertical distribution. This means that any existing turbulence shows mirror symmetry concerning the xy orbital plane, and it is buried within the ρ vertical distribution with the main radial profile since the ρ local increases materialize in narrow and sparsely dense peaks. Such narrow ρ-peaks exist in mirror symmetry concerning the xy orbital plane whatever is z throughout the intermediate compressibility viscous disc model. The simultaneous presence of low values in the ρ spatial distributions occurs for reasons of mass conservation, regarding particles on disc surfaces. This is a clear evidence of saturation of the filling of low $|z|$ disc regions, a result strongly affected by the mass-transfer rate at L_1. The two panels at the bottom of the same picture show the spatial distributions concerning the $\gamma = 1.01$ high compressibility viscous disc model. These profiles display excellent mirror symmetry concerning the xy orbital plane. They also show a glimmer of overall turbulence in the disc's outer radial regions, together with a main ρ radial profile in the innermost regions surmounted by a subtle distribution of particles whose mass-density is larger. This latter peculiarity refers to the small stretched clumps shown in the xy mass-density map at the bottom-right panel of Fig. 27. This tiny distribution of larger ρ particles and the underlying main mass-density peak highlights the presence of a toroidal ring pulled at shorter radial distances by the physically viscous mass radial transport. However, it is also worth noting that at very short radial distances any high compressibility mass-density peak stands out. In fact, the physically viscous transport of accreting and the dominant gravitation at very short distances favour any strong inward decrease of ρ in high compressibility flows.

This Section ends by reporting the plots of the radial and the vertical distributions of ϵ and of the total velocity v for the viscous accretion discs models regarding the three gas compressibility regimes. This is shown in the three pairs of panels in Figs. 32 and 33. In the panels dedicated to the radial distributions of ϵ three theoretical profiles are also reported regarding standard model profile $\epsilon \approx S r_{xy}^{-3/2}$, whose $S = 0.1$, 0.2 and 0.3. Instead, in the radial distribution panels for v, the strictly Keplerian profile is also reported. The collisions among SPH particles naturally lead to a fluctuation in the radial distributions. The lower the gas compressibility, the larger the fluctuations throughout all the radial distributions. The radial distributions of v appreciably fit the Keplerian profile from $r_{xy} \approx 0.05$ inwards according to the relevance of the shear viscous forces against the ever-more prevailing gravitational forces, without any relevance coming from the gas compressibility. In this regard, any damping activated by mechanisms involving $\nabla \cdot \mathbf{v}$ are ineffective for $r_{xy} < 0.1$ - 0.15. Instead, the ϵ radial profiles better fit an $S \approx 0.3$ for $\gamma = 5/3$ and an $S \approx 0.2$ for the other two gas compressibility models. This result for ϵ is a consequence of the relevance of disc thickness for $\gamma = 5/3$, where a halo of hot and cold scattered particles exists. Such a halo is also shown by the vertical distribution profiles on the right-side of Fig. 32, contributing to high and low ϵ values leading to two vertical bumps in mirror symmetry concerning the xy orbital plane $z = 0$. The two bumps approach each other more and more as much as the disc reduces its thickness the lower is the assigned γ. The viscous heating of the cores of the two bumps, shown on the right panels of Fig. 32, are almost independent on γ, which means that the gas compressibility scarcely affects the viscous heating, as ruled by Eq. (D.13) through its kinematic and thermal components. As a consequence, the entire thermodynamics, discussed for the non-viscous modelling is only enhanced by the additional role of viscosity without involving the $z \approx 0$ disc areas. The comparison among the spatial distributions of v, especially in their vertical aspect, shows a tiny viscous slowdown of the subkeplerian total velocity of particles on disc surfaces. This peculiarity comes out by comparing the slopes of the vertical distributions compared to those relative to the inviscid disc modelling at the bottom of Figs. 10 and 26. This demonstrates that whatever is the disc gas compressibility, the adopted physical viscosity correctly works, activating the radial transport mechanism at the expense of the angular kinematics in the conversion of mechanical energy into heat. However, this happens without any massive quantitative variation in the overall kinematics.

5. Discussion and conclusions

5.1. Numerical aspects

From the numerical point of view, the adoption of $W_{erf,ij}$ with $h \approx 5\ 10^{-3}$ exploits a statistically significant number of companions for the SPH numerical integrations, even at the free edges, expanding the integration domain up to at least $4h$. Compact profile Kernel formulations could work even beyond $h = 2\ 10^{-2}$. However, in this case the involved misbehaviour is twofold. The first deficiency still remains if such Kernels do not take into account of the role played by $d^3\mathbf{r}$ and $d^2\mathbf{r}$ in the 3D and 2D spatial integrations respectively in the continuum limit. In 3D and 2D integrals in the continuum limit, the $4\pi r^2$ and $2\pi r$ terms coming from the SPH numerical density n in the SPH summations are indeed responsible for remarkable SPH inconsistencies (Appendix A.2). To be clearer, the summation of Eq. (A.7) in the continuum limit, restricted only to the particle numerical density, leads to the appearance of the $2\pi r$ and $4\pi r^2$ terms in 2D and in 3D respectively as

$$\sum_{j=1}^{N} n_j^{-1} \xrightarrow[N\to\infty]{} \begin{cases} \int_D d^2\mathbf{r} = \int d(\pi r^2) = \int 2\pi r dr \\ \int_D d^3\mathbf{r} = \int d(\frac{4}{3}\pi r^3) = \int 4\pi r^2 dr \end{cases} \quad (2)$$

Neglecting such terms leads to increasingly pressure excesses in the Kernel gradient calculations the greater the number of neighbours provided by any radial increase of the integration domain. The second shortcoming is that of managing the higher artificial viscosity damping in low SPH resolution flows, especially for variable smoothing h in flow expansion models, at the cost of much longer computational time. However, in doing so, other error sources exist whenever working with large h values regarding the angular spatial distribution of neighbours (Vaughan et al., 2008; Vaughan, 2009; Zhu et al., 2015). The 3D ASPH disc modelling in semi-detached LMCBs, highlights such shortcomings in the integration assuming a number of ∼40 companions. Any greater number of neighbours worsen such shortcomings due to their ever-increasing statistical distribution near the upper edge of the integration as h increases. Low compressibility conditions better highlights such shortcomings as the role played by the spatial gradient of the Kernel increases. This means that these problems are attenuated if a low number of neighbours of ∼25–30 affect high compressibility conditions, but they are hidden whatever are h and gas compressibility whenever a dominant gravitational field exists. Over the years, the assigned arbitrary number of neighbours has steadily grown in ASPH techniques at the cost of much longer computational times. Nowadays it is around 150 - 200 for ASPH working with $W_{3,ij}$ and even 300 for ASPH working with $W_{1,ij}$ motivated by the use of Wendland Kernels and their pairing resistance. This effort is made in the belief of reducing as much as possible the discrepancies arising from the comparison between ASPH hydrodynamics and other numerical techniques. In doing so, the problems of the ASPH are believed to come from inaccuracies in the numerical integration by providing structures as close as possible to the best discretization of the continuum, even accepting all the consequences of artificial viscosity coming from the statistical increase of h. Theoretically, an ever-larger number of neighbours should ensure a better convergence towards the continuum limit and also a better consistency of results. However, the simple summation of Eq. (A.21) in reality is a rough formulation of an analytical integral. Therefore, numerical fluctuations prevail without an asymptotic mathematical convergence from a certain number of contributions onwards in the summation, even working in double precision. Moreover, a uniform spatial distribution of neighbours is the best for the convergence of SPH integration results, since even their spatial distribution affects the numerical results involving the h spatial extension (Vaughan et al., 2008; Vaughan, 2009; Zhu et al., 2015). But flow uniformity is a condition that cannot be imposed on the flow evolution.

Most of these inconsistencies are resolved simply multiplying a 1D Kernel analytical formulation by $(4\pi r^2)^{-1}$ in 3D ($(2\pi r)^{-1}$ in 2D). This task is now accomplished in a wider comparison of models than in Lanzafame (2010a). Of course, the choice of a 1D Gaussian Kernel is arbitrary, but it is the one that has the most solid physical basis. The excessive abuse of 1D formulations of the Kernel only entails a relentless search for non-physical numerical solutions suitable for numerical modelling aimed at targeted problems, but lacking an overall physical meaning. Gaussian-based Kernels without a compact support are considered poorly efficient for two reasons. The first reason is dictated by the desire to extend any integration within spatially finite domains. The second reason concerns computational accuracy. Any assumed arbitrary greater number of neighbours is indeed mainly intended for better accuracy of the SPH numerical integrations. Both difficulties come out whenever the integration using $W_{erf,ij}$ involves neighbours within $2h$–$3h$, disappearing if the integration is carried out at least up to $4h$ because $erfc(4) \sim 10^{-9}$(Appendix A.2). Moreover, it is noteworthy that in Monaghan (1992), it is explicitly written that: "*if you want to find a physical interpretation of an SPH equation, it is always best to assume the Kernel is a Gaussian*". Although some time has passed, this warning highlights at least one reason why SPH problems persist despite further Kernel analytical formulations have been proposed. That sentence talks about the physical interpretation of the equations. It means that to understand what the interpolations do, the adoption of a

Gaussian Kernel to express the analytical and theoretical behaviour is the way to go. Of course, it does not say that this is the only way to go in production calculations, and it has been proven in many publications that the problems that SPH had in the past are related to other topics, such as pairing-resistance or gradient accuracy, and not to the use of Kernels with compact support. Tests performed in Appendix A.2 show that there is a range for which truncated Kernels have a similar partition of unity than Kernels with compact support. Whilst, any evaluation of the error in the gradients evaluation is unnecessary. The spatial gradients of the 1D compact support Kernels are in fact exactly zero at the interpolation range limit. Similarly, the $\nabla W_{erf,ij}$ 1D Kernel spatial gradient has a very small value at limit of the interpolation range $4h$, depending on the interpolation spatial extent. Any diverging $\nabla W_{erf,ij}$ is excluded at the truncation outer edge of the interpolation distance. The $\nabla W_{erf,ij}$ function is indeed still differentiable being a single value function even at the truncation outer edge $r_{ij} = 4h$, free of any discontinuity. Therefore, the truncation of its radial dominion of integration does not involve discontinuities (as removable, jump or essential discontinuities).

Typical tests about non-viscous 1D shock tubes, blast waves and 2D viscous radial transport are shown in Lanzafame (2010a) where the Gaussian approach of SPH built up on the error function (Eq. (A.27)) provides results which compare very well with the analytical ones, with the advantage to solve the free-edge difficulties. Moreover, 2D and 3D results are free of any particle pairing instability, as explained in Appendix A.2, as $r_{ij} \to 0$ (Scüssler and Schmitt, 1981; Thomas and Couchman, 1992; Herant, 1994; Swegle et al., 1995; Lanzafame, 2010a, 2018; Springel, 2010; Dehnen and Aly, 2012; Price, 2012; Valizadeh and Monaghan, 2015; Shuangs et al., 2019). The $-\nabla W_{erf,ij} 4\pi r^2$ radial profile is indeed monotonically increasing in 3D as $r_{ij} \to 0$ and it is free of any repulsive barrier leading to ever-decreasing pressure forces as the particles mutual distance decreases towards zero as it occurs for the other two compact Kernel radial profiles. This is clearly shown in Fig. A.41, where the 3D radial profiles of $-\nabla W_{ij} 4\pi r^2$ for all the discussed Kernels are displayed. The presence of the radial barrier as in Fig. A.41 leads to particle crushing as $r_{ij} \to 0$ but, at the same time, it also leads to an excess of pressure forces for the many farther neighbours. Such problem, instead, does not occur in 1D fluid dynamics. The only difficulty in 1D fluid dynamics comes from the presence of an inflexion point in the 1D Kernel profiles incorrectly decreasing the Kernel first spatial derivative as $r_{ij} \to 0$.

The adoption of $W_{erf,ij}$ makes the numerical simulations at least ∼4–5 times longer compared to compact Kernel SPH simulations working with the previously discussed assigned values of h in so far as the total numbers of disc particles are comparable. It is noteworthy to mention that the incorrect excess of pressure forces of the many neighbours near the edge of the Kernel integration domain is the main reason why no accretion discs appear in the $\gamma = 1.1$ ASPH modelling for the LMCBs here considered, although the total energy of the injected particles from L_1 is negative. The differences in results come out thanks to the set of conditions regarding the low stellar masses and the kinematics of the mass-transfer. Stronger gravitational fields and to a lesser extent also lower velocity of mass-transfer would have unavoidably hidden such important discrepancies.

Moreover, to have a better consistency of SPH numerical solutions, we also refined the integration process by considering Eqs. ((A.37) and (A.39)) (Appendix A.2), without obtaining any significant numerical impact for intermediate gas compressibility. Numerical solutions are, instead, affected in ρ and ϵ refinements in the high compressibility modelling thanks to the disc thickness, more thinned in such compressibility conditions. Indeed, the disc thickness, whose opening angle is also affected by the mass-transfer speed, plays an important role in its interaction with the injected stream flow from L_1. In high-speed conditions of mass-transfer, in the intermediate compressibility modelling, the disc thickness allows only the sliding of the injected stream flow onto disc surfaces, allowing the presence of a cold component along disc surfaces. Instead, at the same kinematic conditions of mass-transfer from L_1, being the entire disc thinner in high compressibility disc models, the flow of injected particles even rains above and below the disc plane, hitting the disc surfaces even at short radial distances. Hence, the surface heating in high compressibility conditions better comes out from such refinements of SPH calculations. Therefore, the larger disc thicknesses and also the larger collisional statistical fluctuations of the lower compressibility thermodynamics involve less sensitivity of results to such numerical refinements. Instead, any numerical refinement contribution on v is irrelevant because of the main role of the gravitational field in the momentum equation (Eq. (A.2)). This description is supported by considering that the refinements involved in Eqs. ((A.37) and (A.39)) do not involve any physical quantity, but only the numerical normalization of each computed scalar value through the $\sum_{j=1}^{N} n_j^{-1} W_{ij}$.

As far as the numerical refinements discussed in Appendix A.2 are concerned, we draw attention to the fact that an analytical equivalence exists between Eq. (A.38) obtained by directly performing the first spatial derivative of Eq. (A.36) with equation

$$\nabla\langle A\rangle(\mathbf{r}) = \frac{\int_D [\mathcal{A}(\mathbf{r}') - \mathcal{A}(\mathbf{r})]\nabla W(\mathbf{r},\mathbf{r}',h)d\mathbf{r}'}{\int_D (\mathbf{r}'-\mathbf{r})\cdot\nabla W(\mathbf{r},\mathbf{r}',h)d\mathbf{r}'}, \tag{3}$$

obtained by performing the Taylor series expansion of Eq. (A.36) truncated to the first derivative term, as reported by Liu and Liu (2006) as for the so-called CSPH framework. Indeed, the term in the denominator in Eq. (3)

$$\int_D \Delta\mathbf{r}'\cdot\nabla W(\mathbf{r},\mathbf{r}',h)d\mathbf{r}' \to_{\mathbf{r}'\to\mathbf{r}} \int_D W(\mathbf{r},\mathbf{r}',h)d\mathbf{r}', \tag{4}$$

and its first spatial derivative are both smooth spatial functions. In the above formulation $\Delta\mathbf{r}'\cdot\nabla W(\mathbf{r},\mathbf{r}',h) = \nabla W(\mathbf{r},\mathbf{r}',h)\cdot\int_D d\mathbf{r}' \approx \int_D \nabla W(\mathbf{r},\mathbf{r}',h)\cdot d\mathbf{r}' = W(\mathbf{r},\mathbf{r}',h)$ in the limit $\mathbf{r}' \to \mathbf{r}$, as long as $W(\mathbf{r},\mathbf{r}',h)$ and its 1st spatial derivative are smooth differentiable functions.

5.2. Physical aspects

In this Subsection, some physical aspects concerning the accretion rates in the most significant disc models addressed in this paper will be discussed. Emission lines will also be numerically provided under restricted physical conditions. Since the topic concerns both their common aspects and differences, it is preferred to combine all of these topics in this Subsection rather than distributing them among the various disc models previously discussed.

From the physical point of view, it is interesting to note how the disc's radial transport mechanism is the slowest by adopting $W_{erf,ij}$, still working with artificial viscosity of Eq. (B.3), compared to disc models working with the other Kernels. Both the handling of free edges and the radial viscous transport mechanism look better because particle flow at the disc's outer edge is more collective and regular than that working with other Kernel formulations. Any significant scattering of particles is the indication of a gradient pressure inadequacy involving the Kernel radial profile, whenever negative total energy should impose well-bound structures. In this regard, any spreading of an initially Keplerian pressure-free annulus ring is due to the viscous radial transport (Frank et al., 2002). In this regard, the SPH viscous radial transport solutions working with $W_{erf,ij}$ are much more comparable to the analytical solutions than those working with other compact radial profile Kernel formulations (Lanzafame, 2010a). Such a discrepancy in the radial transport mechanism mostly happens if working with variable spatial resolution lengths h for compact radial profile Kernel domains, which increases artificial viscosity damping as the shear particle collisions involve ever-farther neighbours in an expanding flow as h increases more and more. This occurs even if artificial viscosity is attenuated by using Eq. (B.5) (Balsara, 1995) or Eq. (B.7) (Morris and Monaghan, 1997). Any combination of both attenuations does not change the outcome. This occurs working in ASPH, because of the

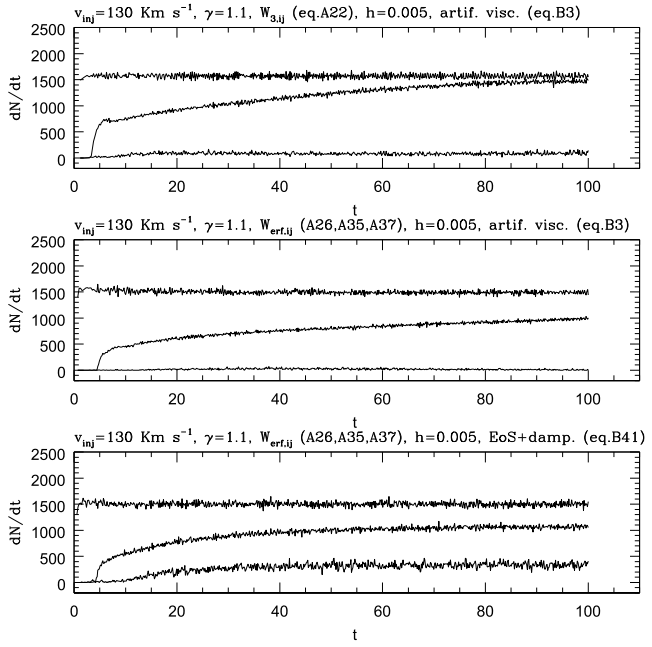

Fig. 34. Mass-transfer rates from L_1, together with accretion and outer edge outflow rates relative to the most significant non-viscous accretion disc models for $\gamma = 1.1$. All rates are reported as dimensionless (particles/time). Data regarding disc modelling are reported in each panel, as well as all common references on top of the entire figure. In each panel, the rates referring to the mass-transfer are the highest, while those referring to the outflow from the outer disc edge are the lowest.

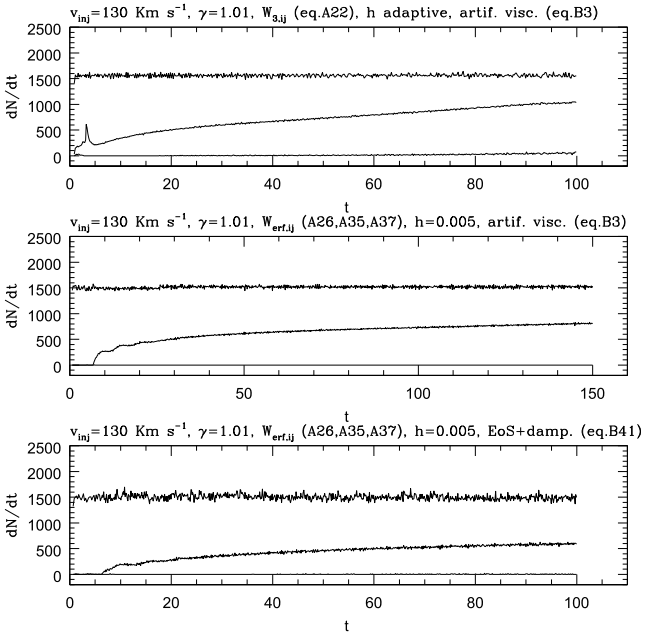

Fig. 35. Mass-transfer rates from L_1, together with accretion and outer edge outflow rates relative to the most significant non-viscous accretion disc models are shown for $\gamma = 1.01$. All rates are reported as dimensionless (particles/time). Data regarding disc modelling are reported in each panel, as well as all common references on top of the entire figure. In each panel, the rates referring to the mass-transfer are the highest, while those referring to the outflow from the outer disc edge are the lowest.

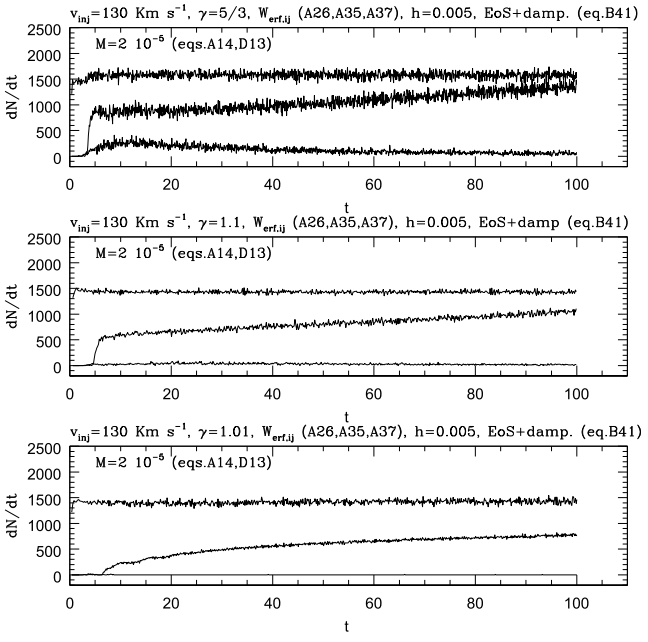

Fig. 36. Mass-transfer rates from L_1, together with accretion and outer edge outflow rates relative to the viscous accretion disc models are shown for $\gamma = 5/3$, 1.1 and 1.01. All rates are reported as dimensionless (particles/time). Data regarding disc modelling are reported in each panel, as well as all common references on top of the entire figure. In each panel, the rates referring to the mass-transfer are the highest, while those referring to the outflow from the outer disc edge are the lowest.

statistical significant increase of h is an effect induced by the SPH formulation of the momentum and energy equations (Eqs. (A.10) and (A.11)), where ∇W_{ij} multiplies a pressure terms also including the artificial viscosity contributions. This detail is shown by looking at the mass accretion rates plotted in Figs. 34 and 35, reporting the mass-transfer rates, together with the mass accretion and the outer edge mass outflow rates as a function of time for the non-viscous disc models regarding $\gamma = 1.1$ and $\gamma = 1.01$. The conversion from particle/time to g s^{-1} is given by $\approx \rho\rho_\circ (hr_\circ)^3 t_\circ^{-1}$, where the normalization values of $\rho_\circ$, $r_\circ$ and $t_\circ$ are discussed in Section 2. Assuming a dimensionless $\rho \approx 10^{-14}$, this conversion term is of the order of $\approx 2.6\ 10^9$ g s^{-1}. However, considering that the physics around L_1 is unknown, all discussed results and conclusions are not affected by considering very different values for ρ_{inj} affecting ρ (Section 2). This is because Eqs. ((A.2) and (A.3)) regard time derivatives of physical quantities per unit mass: ϵ and the momentum per unit mass **v**. So that while the dimensionless ϵ and **v** are not involved, the dimensionless ρ linearly scales since $\rho_\circ$ remains unchanged.

The accretion rates shown in Figs. 34–36 show that in some cases they are increasing so much that the purpose of getting steady disc configurations is fulfilled. Instead, in other cases, especially working with $W_{erf,ij}$, that end can be achieved after a huge extension of calculations. As an example, the extension of non-viscous simulations for $\gamma = 1.01$, from a time $t = 100$ up to $t = 150$ involved 4 more weeks working with a 4 GHz Core I7 Intel platform of the 9000 series. Therefore, we decided to interrupt the calculations because the extrapolation of the accretion rate profile would require far longer computational time to get a complete steady-state configuration considering the slowly increasing number of the total number of particles. The strict comparison of inviscid accretion rates, shown in Figs. 34 and 35, highlights the role of the assumed gas compressibility affecting not only pressure forces but also the mass radial transport at the disc's inner edge. As it is expected, the higher γ, the higher the accretion rate. In the same two figures, it is shown how the assumed Kernel radial profile also affects the accretion rates. Indeed the incorrect pressure force excess, due to the many farther neighbours, incorrectly increases the accretion rates without any algebraic compensation of the $4\pi r^2$ term coming from the vector calculus of $d^3\mathbf{r}$ in the 3D SPH integration in the continuum limit, especially in adaptive conditions. Moreover, such pressure force excess also activates a contextual excess of mass radial transport. What is also

relevant is that the wished spiral structures came out adopting $W_{erf,ij}$ together with artificial viscosity (Eq. (B.3)) and that the progression of the disc's radial extension is slower than adopting the other two Kernels. This aspect solves at least one discrepancy described in Motl et al. (2017) where SPH disc models provide structures comparable to those obtained when working with other numerical approaches, with the flaw of a faster radial evolution. Last, but not least, disc models obtained using $W_{erf,ij}$, Eq. (B.3), and also including the numerical refinement of Eqs. ((A.37) and (A.39)), show a vertical structure along z in which stratification of ϵ occurs, especially in high compressibility conditions. In such a vertical temperature stratification, a peak value of ϵ no longer strictly corresponds to $z = 0$ on the orbital plane at the same radial distance r_{xy}. While particles at $z = 0$ still hold values corresponding to the standard model of Shakura (1973) and Shakura and Sunyaev (1973), instead particles within the disc thickness at larger $|z|$, show a bump in the ϵ values, together with the presence of a population of colder particles. This result particularly affects the high compressibility models in which the reduced disc thickness better allows an almost vertical collision of cold particles flowing from L_1 onto the hotter disc surfaces even at short radial distances. Any collisional deviation by the strictly Keplerian kinematics, mainly involving the disc surfaces, activates any dissipation mechanism. Thus, the dissipative processes in the particle collisions, even activated by the simpler artificial viscosity, provide larger heating in such regions.

In the context of the non-viscous disc modelling, the substitution of any artificial viscosity with a real physical damping within the EoS of ideal gases (Eq. (B.41)), empirically calibrating $\mathcal{K} \approx 2\ 10^3$ (Eq. (B.38)), allows an effective damping activated whenever $\nabla \cdot \mathbf{v} < 0$. That means the damping is ignited whenever a gas compression activates a deviation from the strictly Keplerian velocity in 2D and 3D flows. In this case, a non-viscous disc structure dominated by a steady toroidal ring comes out, which is the first focus of this work. Any activation of artificial viscosity (Eq. (B.3)) – as well as the Hugoniot jump conditions – for the numerical integrations of the Euler equations for solving the Riemann problem indeed always produce a dissipation whenever two Lagrangian particles come closer to each other in inviscid shear flows. The prevention of any steady toroidal ring indeed occurs because of the shearing of contiguous particles approaching each other even if $\nabla \cdot \mathbf{v} = 0$, as in Keplerian kinematics. Disc models, whose damping is insted physically activated by $\nabla \cdot \mathbf{v} < 0$, are also surrounded by a halo of scattered particles due to the excess of heating coming from the non-viscous damping mechanism involving significant compressions, especially the higher are the compressibility conditions.

Lubow and Shu (1975) and Frank et al. (2002) in their simple accretion disc modelling, discussed the presence of a steady toroidal ring structure. As for the disc non-collisional modelling in an LMXRB, Inoue (2021) discussed the presence of a steady toroidal ring providing a hotter accretion flow along the middle plane of the disc together with another flow, colder and subkeplerian, enveloping the first. Our collisional approach provides results where a vertical profile of ϵ exists in the innermost disc's radial regions, together with subkeplerian kinematics on disc surfaces, explaining to each other whatever is the gas compressibility. In this scenario, the two roles of the mass-transfer rate and gas compressibility look much more complicated than expected. From the observational point of view, conclusions of other authors (Churazov et al., 2001; Díaz Trigo et al., 2006; Galis, 2007; Inoue, 2022) lead to a disc, a torus, or an envelope or a mixing of them. Thus, at this point, an unanswered question is what prevents or limits any action of the turbulent physical viscosity in such cases.

In the Navier–Stokes physically viscous approach (Eqs. (A.1)–(A.5)), a bound accretion disc excludes any steady toroidal ring in its native position. A toroidal ring can still be detected closer to the primary star only working with the EoS for ideal gases as Eq. (B.41) in high compressibility conditions. The damping within the EoS and in the bulk component of the stress tensor $\boldsymbol{\tau}$, both working with $\nabla \cdot \mathbf{v}$, favour

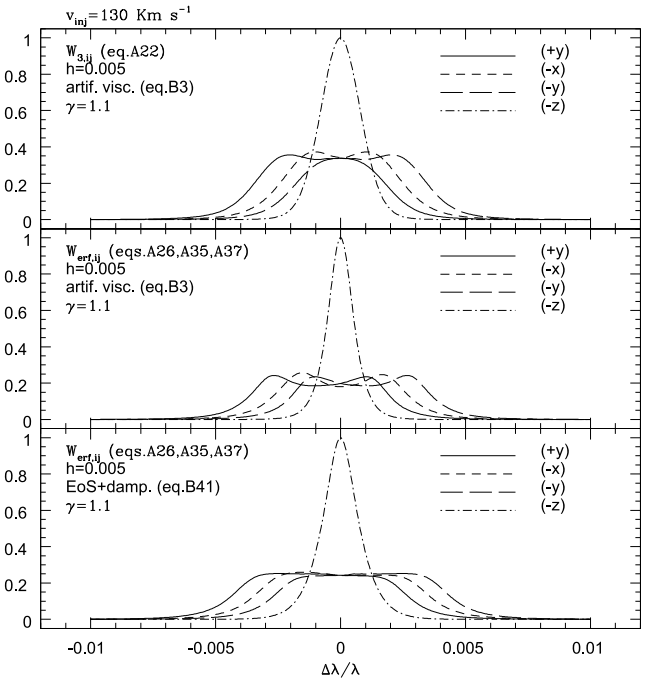

Fig. 37. Theoretical emission line for the non-viscous accretion disc models in the same sequence of Fig. 34 in the simplest case of an optically thin disc. In each panel 4 lines are represented according to the direction of observation. Notice that for each plot, a normalization to the maximum value at $\Delta\lambda = 0$ is taken into account, by looking at the disc along the $-z$ direction. The common value of v_{inj} is reported on top of the entire picture.

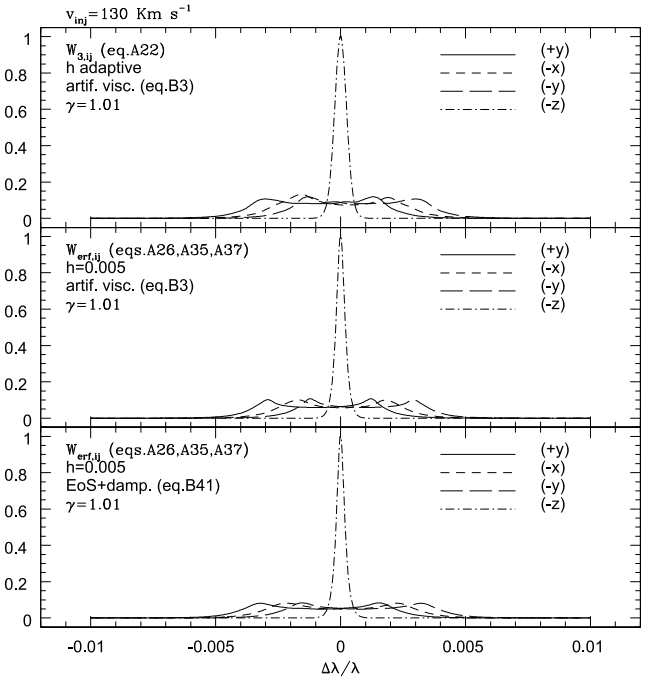

Fig. 38. Theoretical emission line for the non-viscous accretion disc models in the same sequence of Fig. 35 in the simplest case of an optically thin disc. In each panel 4 lines are represented according to the direction of observation. Notice that for each plot, a normalization to the maximum value at $\Delta\lambda = 0$ is taken into account, by looking at the disc along the $-z$ direction. The common value of v_{inj} is reported on top of the entire picture.

the setting of a Keplerian toroidal ring within the disc structure. Instead, any damping coming from shear flow components activates an

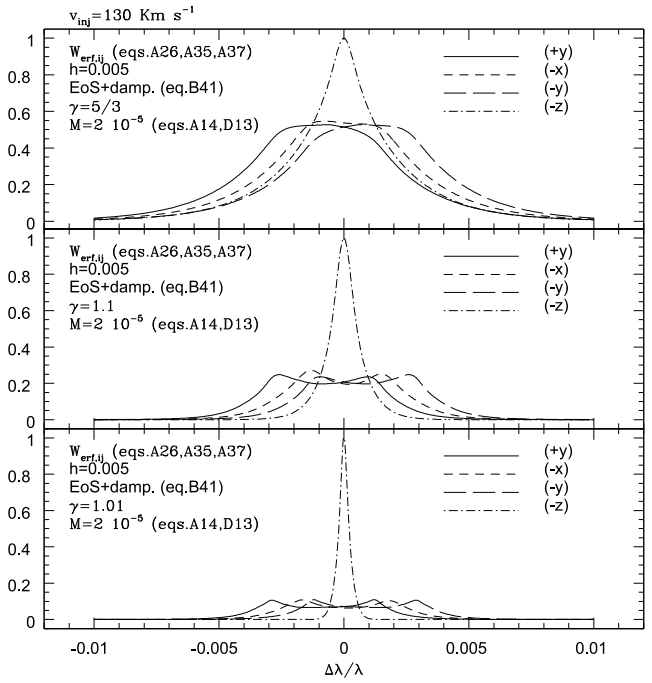

Fig. 39. Theoretical emission line for the viscous accretion disc models in the same sequence of Fig. 36 in the simplest case of an optically thin disc. In each panel 4 lines are represented according to the direction of observation. Notice that for each plot, a normalization to the maximum value at $\Delta\lambda = 0$ is taken into account, by looking at the disc along the $-z$ direction. The common value of v_{inj} is reported on top of the entire picture.

exchange of angular momentum throughout a disc structure, favouring the radial disc stretching. The development of mass-density spirals occurs whenever the disc's radial extension exceeds the tidal truncation radius. Instead, the bulk component of the stress tensor makes easier the formation of flow clumps as long as the viscosity effectively counterbalances the pressure forces. Even though contact forces in fluid dynamics are computed through spatial derivatives, this can be understood taking into account that $p \propto (\gamma - 1)\epsilon$ and that the kinematic viscosity coefficient is $\propto \epsilon^{1/2}$, while the non-viscous damping is $\propto \epsilon^{-1/2}$ (Eq. (B.41)). This explains the presence of clumps in the outer regions of low compressibility viscous discs, as it is shown in Fig. 27 for $\gamma = 5/3$, in an environment whose ρ is rather flat and the dominance of the gravitational field (inducing a Keplerian kinematics) is reduced at so large distances. Therefore, in the innermost disc areas, the Keplerian kinematics mainly activates the shear component of the viscous stress tensor, quenching at the same time the bulk viscosity contribution as well as any other damping working with $\nabla \cdot \mathbf{v}$. Instead, both the shear and the bulk components of the viscous stress tensor work together in the outer disc areas. The flow turbulence characterizes the intermediate compressibility configuration – as also shown in the same Fig. 27 for $\gamma = 1.1$ – without a clear prevalence between pressure and viscous forces. In high gas compressibility, the decrease of overall temperature when $\gamma \to 1$, leads the entire structure controlled by the primary's gravitational field towards a configuration as it were inviscid and pressure-free.

As regards the thermal aspects of the viscous disc models, any subkeplerian shear flow onto the disc surfaces activates a viscous heating, further increasing the local temperature stratification, determining some sort of thermal bumps on disc surfaces. Cold and scattered particles exist above and below the disc surfaces at the same radial distance. They come from the high-speed injected stream whenever the disc thickness is thin enough to allow the direct hitting of disc surfaces in high compressibility flows.

It is noteworthy that the introduced physical viscosity does not significantly affect the mass-transfer rate from L_1. Instead, as it is shown in Fig. 36, the gas compressibility affects the accretion rates because high gas compressibility involving larger $|\nabla \cdot \mathbf{v}|$ values activates the bulk viscosity in a collisional free fall condition at the disc's inner edge despite the prevailing gravitation. This means the lower γ, the faster the mass radial transport at the disc's inner edge. The effectiveness of the physical viscosity on the radial kinematics is shown by comparing viscous accretion rates for the $\gamma = 1.1$ and $\gamma = 1.01$ viscous disc models of Fig. 36 with respect to their inviscid counterparts in Figs. 34 and 35, working with the same $W_{erf,ij}$. In fact, in higher compressibility models, a larger discrepancy exists between the viscous accretion rate to that non-viscous.

From the observational point of view, it is advantageous that the disc kinematics can reasonably be considered almost Keplerian even for the larger velocity collisional fluctuations of the low compressibility and thicker disc models. The comparison of observational data with theoretical ones is possible knowing the geometric inclination θ of the disc orbital plane to the direction of observation, together with the collapsed star mass and the mutual distance between the two stellar components (Casares et al., 2017). Once the observational data lead to the understanding of such parameters, within the observational errors, a comparison can be made among the observational emission lines with a theoretical emission line profile. Theoretical emission lines associated with the most significant disc models of this paper are shown in Figs. 37–39 in the optically thin case for the sake of simplicity. Such profiles are calculated for 4 points of view of the observer, but they are always reproducible for any angle of view. Of course, such a procedure is meaningful as long as the observational errors are larger than the errors made on the attribution of strict Keplerian kinematics to the disc flow. In Figs. 37–39 every emission line is normalized to the height of the peak value for each panel referring to the disc as seen along the $-z$ direction (that is as it is seen from the top). Therefore, any downward shaping of the emission line profiles observed along the orbital plane provides indications on gas compressibility, thermodynamics and kinematics along the line of sight. This is done assuming that the disc angular kinematics is well known although, in reality, it is slightly subkeplerian. This is an aspect that stands out best the stronger the primary's gravitational field and the higher the gas compressibility, reducing the collisional fluctuations of any physical property, and leading the radial distribution of v towards a strictly Keplerian one. In Figs. 37–39, the width of the symmetric central profile deals with two physical contributions: the disc kinematics along the line-of-sight (also related to disc thickness along the same direction) and the gas temperature. Such two contributions mix perfectly with each other in the optically thin cases but inevitably lead to a line asymmetry in the optically thick case (Jackson et al., 2019) which we do not discuss.

Fig. 37 shows at the bottom panel a flattening of emission lines seen along the orbital plane instead of the characteristic double horn profiles shown in all other panels throughout the non-viscous and viscous disc models. Such a line flattening is related to the presence of a toroidal ring within the disc bulk. Any emission from the colder and slower gas flows is indeed strongly limited. Although less evident, the same peculiarity can be seen at the bottom panel in Fig. 38 in cases of greater compressibility. A less pronounced flattening in this case is due to the emission contributions coming from other areas of the disc. These other areas of the disc in fact contain a rather relevant population of particles because of the high compressibility of the gas. Another peculiarity is that the emission line of the viscous disc model whose $\gamma = 5/3$ on the top panel of Fig. 39, does not show any appreciable double horn profile looking along the orbital plane. Indeed, it still holds a one-peak emission line profile. This is due to the emission coming from the many slow gas components of a geometrically thick disc as well as the emission coming from an extended envelope. The difficulty of disentangling either a steady toroidal ring or an envelope, or both has

induced some authors (e.g. Galis, 2007) to argue about the presence of these structures. Lastly, any presence of spirals cannot be distinguished from these kinds of pictures whenever involving small percentages of the entire disc mass.

5.3. Concluding remarks

The current numerical summation of Eq. (A.7) of the SPH integral of Eq. (A.6) is strictly valid only in the 1D SPH fluid dynamics. Any current Kernel analytical formulation involves only the particle mutual radial distance with respect to the assumed smoothing length for the sake of practicality, avoiding time consuming double or triple integrals. Instead, 2D and 3D SPH spatial integration should be strictly written and also considering the neighbour spatial angular distribution. This means that the SPH works well whenever the 2D or 3D spatial distribution of neighbour particles is uniform. Spatial flow discontinuities, involving non-uniform spatial distributions of neighbours, inevitably lead to errors in the numerical integration as expressed by the summation (Eq. (A.7)) (Vaughan et al., 2008; Vaughan, 2009; Zhu et al., 2015). The worst errors come from the 2D and 3D numerical integrations whenever the particle number density n in Eq. (A.7) correctly involves multiplicative $2\pi r$ (in 2D) and $4\pi r^2$ terms (in 3D) in the continuum limit which are responsible for a modification of the radial profile of the integrating function. This implies that in 2D and in 3D SPH flow dynamics, any Kernel radial profile should analytically also take into account of such multiplicative radial terms. Otherwise pressure forces excesses, due to incorrect spatial gradients, affect the entire flow dynamics especially if adaptive spatial approaches involving compact radial profile radial Kernels are considered. In this regard, the higher the number the neighbours, the higher the gradient pressure excesses coming from the many farther neighbours. Hence, the first focus of this paper is to highlight an integration-interpolation Kernel radial profile giving satisfactory interpolation capability, numerical consistency and 2D and 3D correctness of calculations of spatial gradients (Lanzafame, 2010a, 2018). According to such non-adaptive scheme, a satisfactory number of SPH neighbours is obtained by the radial truncation bounding of the spatial integration domain by working with a Gaussian-based Kernel.

Therefore, in this paper, a numerical study is performed by exploiting the complexity of the various phenomenologies of the non-viscous accretion disc modelling in the SPH framework. This is made by assuming high-speed mass-transfer conditions from L_1 for various gas compressibility conditions for an accretion disc in a semi-detached LMCB around a white dwarf primary star. The presence of any other secondary compact star is excluded. These are mass-transfer conditions deliberately contrary to any thin disc formation as it is preferable to identify the thinnest disc among thick discs rather than among thin discs. This choice is made for an in-depth understanding of numerical and physical aspects related to pressure forces computed by Kernel spatial gradients for high-speed flow collisions as long as the total energy of the mass-transfer flow is negative. Such numerical and mathematical investigation has led to better answers than those offered by the simpler dedicated numerical tests, often performed on much shorter times, handling either 1D flow discontinuities or 2D radial flow transport mechanisms (Lanzafame, 2010a, 2018).

Furthermore, in order to get a disc model corresponding to a non-viscous ideal gas, a reformulation of the EoS of a perfect gas is considered including physical non-viscous damping ignited only whenever a local gas compression occurs. A steady toroidal ring should indeed come out still in inviscid conditions as reported in Lubow and Shu (1975) and Frank et al. (2002). Therefore, any artificial viscosity or any mathematical damping coming from some jump conditions of flow discontinuities for the Riemann problem are excluded in a Lagrangian framework, as in Lanzafame (2010b). In this regard, any Lagrangian formulation of damping, igniting a shear dissipation whenever two particles approach each other, inevitably leads to a shear viscosity even in non-viscous conditions (Okazaki et al., 2002) in shear flows. An damping mechanism working as a real physical viscosity is indeed currently deliberately exploited to get a disc's radial transport mechanism in inviscid conditions. For this reason, as long as an artificial viscosity is working in a Lagrangian framework, it is improper any attribution of non-viscous flow dynamics.

Lastly, we included a 3D bulk and shear turbulent physical viscosity, whose formulation compares to Prandtl (1925) formulation as in Lanzafame (2015), deliberately distancing from any formulation more suitable for the 2D disc modelling, like that of Shakura (1973) and Shakura and Sunyaev (1973). The different roles of the bulk and the shear turbulent physical viscosity are also discussed.

The entire mathematical basis is shifted in the Appendices, also including an in-depth discussion regarding all numerical topics of this paper. Thus, in the text the attention is mainly paid to the physical aspects, although both topics are inevitably related to each other.

Results showing interesting convergence with some observational conclusions (Churazov et al., 2001; Díaz Trigo et al., 2006; Galis, 2007; Inoue, 2022) are discussed even for the non-viscous disc models, as well as some differences in disc structures and thermodynamics, according to the compressibility–viscosity combinations.

SPH approach of fluid dynamics are widely used not only in different fields of physics, but also in engineering fields. However, the perception of such integration errors comes out whenever a subsonic kinematics exist, especially in free-edge boundary conditions, as long as external force fields are not dominant. In this regard, such a kinematics could even be just a radial transport mechanism. In this paper, the astrophysical example of accretion discs 3D modelling in LMCBs is discussed, with the clear advantage of performing a computational flow dynamics within a confined spatial environment restricted to the Roche lobe of the primary compact star over long time scales. In this regard, the mass-transfer mechanism could even involve the mass loss from a giant secondary star insted of inner Lagrangian point L_1 (Lanzafame and Belvedere, 1998). Other intriguing astrophysical 2D or 3D topics involving subsonic free-edge flow expansion should be those concerning both stellar winds of Wolf-Rayet stars or of O-B stars and their interaction with circumstellar envelopes or the collision of stellar winds in binary systems. It should also be noteworthy the study of the subsonic outer edge expansion of the rarefaction wave of the envelope of a circumstellar cloud during its gravitational collapse leading to a star formation. Even though heavily affected by the conditions imposed on the boundaries, the numerical simulation of the subsonic–sonic granulation of a portion of a 3D solar photosphere could also be another interesting astrophysical topic where the solutions here proposed regarding SPH deficiencies should be effective.

Declaration of competing interest

The authors declare that they have no known competing financial interests or personal relationships that could have appeared to influence the work reported in this paper.

Data availability

No data was used for the research described in the article.

Appendix A. In-depth study on CFD equations in the SPH framework

In this Appendix, it is discussed how the Kernel analytical formulation affects the results of SPH integration–interpolations in the solution of CFD viscous Navier–Stokes equations and the non-viscous Euler equations whenever the terms including the viscous stress tensor $\boldsymbol{\tau}$ are excluded.

A.1. The CFD Navier–Stokes equations in the SPH framework: The integration-interpolation Kernel role

In the physically viscous flows, the system of equations

$$\frac{d\rho}{dt} = -\rho\nabla\cdot\mathbf{v} \qquad \text{continuity equation} \quad (A.1)$$

$$\frac{d\mathbf{v}}{dt} = -\frac{\nabla p}{\rho} + \mathbf{f} + \frac{1}{\rho}\nabla\cdot\boldsymbol{\tau} \qquad \text{momentum equation} \quad (A.2)$$

$$\frac{d}{dt}\left(\epsilon + \frac{1}{2}\mathrm{v}^2\right) = -\frac{1}{\rho}\nabla\cdot[p\mathbf{v} - \mathbf{v}\cdot\boldsymbol{\tau} + c\nabla(\rho\epsilon)] + \mathbf{f}\cdot\mathbf{v} \qquad \text{energy equation} \quad (A.3)$$

$$p = f(\gamma, \rho, \epsilon, \mathbf{r}, \mathbf{v}) \qquad \text{equation of state} \quad (A.4)$$

$$\frac{d\mathbf{r}}{dt} = \mathbf{v} \qquad \text{kinematic equation.} \quad (A.5)$$

needs to be solved.

In these equations, vectors and tensors are written in bold characters. Most of the adopted symbols have the usual meaning: d/dt stands for the Lagrangian derivative, ρ is the gas density, ϵ is the thermal energy per unit mass, p is the gas pressure (here expressed as a function of local properties). $\mathbf{v}$ and $\mathbf{r}$ are the velocity and position vectors, and $\mathbf{f}$ is the external force field per unit mass. The adiabatic index γ has the meaning of a numerical parameter whose value lies in the range between 1 and 5/3, in principle. Instead, $\rho^{-1}\nabla\cdot[c\nabla(\rho\epsilon)]$ in Eq. (A.3) deals with the thermal conductivity terms. $\boldsymbol{\tau}$ is the viscous stress tensor describing both the shear and the bulk transfer of momentum and the viscous heating among contiguous fluid components.

Notably that the thermal flux term $c\nabla(\rho\epsilon)$ includes two contributions: the first contribution depends on the thermal gradient $\nabla\epsilon$ that is currently used for solids or incompressible fluids. While the second contribution depends on the density gradient $\nabla\rho$ related to the mass diffusivity (here it is excluded in the continuity equation).

The SPH method is a Free Lagrangian scheme (Whitehurst, 1995) that discretizes the fluid into moving interacting and interpolating domains called "particles" and whose convergence has been analytically discussed in Di Lisio et al. (1998). All particles move according to pressure and body forces. The method makes use of a Kernel $W(\mathbf{r}, \mathbf{r}', h)$ useful to smoothing interpolate a physical quantity $A(\mathbf{r})$ related to a gas particle at position $\mathbf{r}$ according to the interpolation–convolution integral:

$$\langle A\rangle(\mathbf{r}) = \int_D \mathcal{A}(\mathbf{r}')W(\mathbf{r}, \mathbf{r}', h)d\mathbf{r}', \quad (A.6)$$

being $\mathcal{A}(\mathbf{r}') = A(\mathbf{r}')$ at the beginning of the SPH numerical calculation, but being $\mathcal{A}(\mathbf{r}') = \langle A\rangle(\mathbf{r}')$ for all subsequent instants. $W(\mathbf{r}, \mathbf{r}', h)$, the interpolation Kernel, is a function – or a combination of contiguous functions – continuously differentiable, defined within a radial extension whose length is of the order of the spatial resolution length: $\sim 1, 2, \ldots, 4h$ etc., and whose limit for $h \to 0$ is the Dirac delta distribution function. All physical quantities are described as extensive properties smoothly distributed in space and computed by interpolation at $\mathbf{r}$. In summation terms Eq. (A.6) is converted as:

$$\langle A\rangle_i = \sum_{j=1}^{N} \frac{\mathcal{A}_j}{n_j} W(\mathbf{r}_i, \mathbf{r}_j, h_i) = \sum_{j=1}^{N} \frac{\mathcal{A}_j}{n_j} W_{ij} \quad (A.7)$$

where subscripts i and j identify the respective particle positions. The summation is extended to all particles included within the domain D. $n_j = \rho_j m_j^{-1}$ is a "smooth" number density relative to the jth particle. In fact, n_j^{-1} is described as a "discrete volume element" (Saitoh and Makino, 2013), or as "continuous estimator of the particle volume" (Hopkins, 2013). These attributions have the meaning that n_j^{-1} is not exactly a defined geometric volume since ρ, n, and even m itself are always smooth properties (Lanzafame, 2013). $W(\mathbf{r}_i, \mathbf{r}_j, h_i)$ is the adopted interpolation Kernel whose value is determined by the relative distance between particles i and j.

Two principles are embedded in the SPH conversion of CFD equations. As a first principle, each SPH particle is an extended, spheroidal domain where any physical quantity A has a density profile $AW(\mathbf{r}_i, \mathbf{r}_j, h_i) \equiv AW(|\mathbf{r}_i - \mathbf{r}_j|, h_i) = AW(r_{ij}, h_i)$. In this formulation, since $W(\mathbf{r}_i, \mathbf{r}_j, h_i) \equiv W(|\mathbf{r}_i - \mathbf{r}_j|, h_i) = W(r_{ij}/h_i)$, the Kernel interpolation function explicitly depends only on the mutual radial distance of particles r_{ij} with respect to the assumed spatial resolution smoothing length h_i. This excludes any Kernel correlation from the choice of the coordinate reference system. As a second principle, A at the position of each SPH particle could be interpreted as a convolution process by filtering $A(\mathbf{r})$ with a single windowing function whose spatial resolution length is of the order of h. In doing so, fluid data are considered isotropically smoothed all around each particle along a length scale h. Thus, according to these two concepts, the SPH value of the physical quantity A is the overlapping of smooth density profiles of A of all particles around. This means that the compactness of the Kernel shape should provide the principal contribution to the interpolation summation for each particle by its closest neighbours, although the smaller contribution of the many farther neighbours is also significant. According to both approaches, the mass is globally conserved in so far as the total particle number is constant. As a further point of view, the statistical meaning of Eq. (A.7) is that any physical property around each fluid particle could also be seen as a weighted average of a statistical computational process, being $W(\mathbf{r}_i, \mathbf{r}_j)n_j^{-1}$ the statistical weight in the summation.

In SPH formalism, Eq. (A.1) takes the form of either:

$$\rho_i = \sum_{j=1}^{N} \frac{\rho_j}{n_j} W_{ij} = \sum_{j=1}^{N} m_j W_{ij}, \quad (A.8)$$

being the mass-density $\rho_i = m_i n_i$, where m_i and n_i are the particle mass and the number density respectively, or the direct SPH conversion of the continuity equation as:

$$\frac{d\rho_i}{dt} = \sum_{j=1}^{N} m_j \mathbf{v}_{ij}\cdot\nabla_i W_{ij}, \quad (A.9)$$

where $\mathbf{v}_{ij} = \mathbf{v}_j - \mathbf{v}_j$. Instead, Eqs. ((A.2) and (A.3)) take the form:

$$\begin{aligned}\frac{d\mathbf{v}_i}{dt} &= -\sum_{j=1}^{N} m_j\left(\frac{p_i^*}{\rho_i^2} + \frac{p_j^*}{\rho_j^2}\right)\nabla_i W_{ij} + \mathbf{f}_i + \\ &\sum_{j=1}^{N} m_j\left(\frac{\boldsymbol{\tau}_i}{\rho_i^2} + \frac{\boldsymbol{\tau}_j}{\rho_j^2}\right)\cdot\nabla_i W_{ij}\end{aligned} \quad (A.10)$$

and

$$\begin{aligned}\frac{dE_i}{dt} &= -\sum_{j=1}^{N} m_j\left(\frac{p_i^*\mathbf{v}_i}{\rho_i^2} + \frac{p_j^*\mathbf{v}_j}{\rho_j^2}\right)\cdot\nabla_i W_{ij} + \mathbf{f}_i\cdot\mathbf{v}_i + \\ &\sum_{j=1}^{N} m_j\left(\frac{\boldsymbol{\tau}_i\cdot\mathbf{v}_i}{\rho_i^2} + \frac{\boldsymbol{\tau}_j\cdot\mathbf{v}_j}{\rho_j^2} + \frac{\rho_j}{\rho_{ij}}c_{ij}\epsilon_j\right)\cdot\nabla_i W_{ij}\end{aligned} \quad (A.11)$$

respectively, on the basis of the hypothesis that

$$\nabla\langle A\rangle(\mathbf{r}) \simeq \int_D \mathcal{A}(\mathbf{r}')\nabla W(\mathbf{r}, \mathbf{r}', h)d\mathbf{r}', \quad (A.12)$$

that is

$$\nabla\langle A\rangle_i \simeq \sum_{j=1}^{N} \frac{\mathcal{A}_j}{n_j}\nabla W(\mathbf{r}_i, \mathbf{r}_j, h_i) = \sum_{j=1}^{N} \frac{\mathcal{A}_j}{n_j}\nabla_i W_{ij} \quad (A.13)$$

since $\mathcal{A}(\mathbf{r}')$ is a smooth function of $\mathbf{r}'$. $E_i = \epsilon_i + \mathrm{v}_i^2/2$, $\rho_{ij} = 0.5(\rho_i + \rho_j)$, while $p_i^* = p_i$ whenever a shock-tracking (also called shocking-fitting) technique, working with a Rankine–Hugoniot Godunov-like scheme, is adopted in solving discontinuities in CFD (Parshikov, 1999; Parshikov et al., 2000; Parshikov and Medin, 2002; Inutsuka, 2002; Imaeda and Inutsuka, 2002; Cha and Whitworth, 2003; Cha and Wood, 2016;

Molteni and Bilello, 2003; Iwasaki and Inutsuka, 2011; Sugiura and Inutsuka, 2017), otherwise p_i^* needs also to include a dissipative small pressure term if working with a shock-capturing technique (LeVeque, 1992; Hirsch, 1997; Fletcher, 1998).

A thermal conductivity numerical term $k_{ij} \propto h_{ij} c_{sij} \rho_{ij}^{-1} (\epsilon_i - \epsilon_j)(r_i - r_j)^{-1}$ is usually added to the pressure terms within the parenthesis in the first summation in the energy equation, useful to smooth out spurious discontinuities in the numerical solutions of Euler equations (Monaghan, 1992).

In the momentum and the energy equations, the viscous stress tensor $\tau_{\alpha\beta}$ includes the positive first and second dynamic viscosity coefficients η and ζ which are velocity independent and describe the tangential shear and the bulk viscous stresses respectively as:

$$\tau_{\alpha,\beta} = \eta \sigma_{\alpha,\beta} + \zeta \nabla \cdot \mathbf{v} \tag{A.14}$$

where

$$\sigma_{\alpha,\beta} = \frac{\partial \mathrm{v}_\alpha}{\partial x_\beta} + \frac{\partial \mathrm{v}_\beta}{\partial x_\alpha} - \frac{2}{3}\delta_{\alpha,\beta} \nabla \cdot \mathbf{v}. \tag{A.15}$$

In these equations α and β are spatial indexes. Defining

$$V_{i\alpha\beta} = \sum_{j=1}^{N} \frac{m_j \mathbf{v}_{ji\alpha}}{\rho_j} \frac{\partial W_{ij}}{\partial x_\beta} \tag{A.16}$$

as the SPH formulation of $\partial \mathrm{v}_\alpha / \partial x_\beta$, the SPH equivalent of the shear is:

$$\sigma_{i\alpha\beta} = V_{i\alpha\beta} + V_{i\beta\alpha} - \frac{2}{3}\delta_{\alpha\beta} V_{i\gamma\gamma} \tag{A.17}$$

A full justification of this SPH formalism can be found in Flebbe et al. (1994a,b).

Some variations of SPH have also been proposed with the aim of improving the fluid dynamics behaviour, especially for the Riemann problem. In one of these, also known as XSPH (Monaghan, 1992), the ith particle position, coming from the integration of Eq. (A.5), is calculated by adding a statistical correction to the particle velocity as

$$\frac{d\mathbf{r}_i}{dt} = \mathbf{v}_i + \Delta \mathbf{v}_i, \tag{A.18}$$

where

$$\Delta \mathbf{v}_i = \sum_{j=1}^{N} m_j \frac{\mathbf{v}_{ji}}{\rho_{ij}} W_{ij}, \tag{A.19}$$

being $\mathbf{v}_{ji} = \mathbf{v}_j - \mathbf{v}_i$, taking into account of the neighbour velocity discrepancies around each ith particle. However, the introduction of a further Kernel-depending equation, makes easier shortcomings coming from any inadequacy of its analytical profile.

A.2. Examples of some SPH Kernels: Analytical radial profiles and quality of integration-interpolations

Several Kernel formulations exist in the literature (e.g. Fulk and Quinn, 1996; Liu et al., 2003; Hongbin and Xin, 2005; Cabezón et al., 2008, 2017; Lanzafame, 2010a, 2018; Dehnen and Aly, 2012; Yang et al., 2014; Valizadeh and Monaghan, 2015; Frontiere et al., 2017), whose common characteristics are that they are all analytical formulations of one spatial variable, whose second spatial derivative is still a continuous function. Such radial profiles also take into account, as a natural consequence of Eqs. ((A.6) and (A.7)), that

$$\int_D W(\mathbf{r}, \mathbf{r}', h) d\mathbf{r}' = 1, \tag{A.20}$$

which numerically becomes

$$\sum_{j=1}^{N} \frac{W(\mathbf{r}_i, \mathbf{r}_j, h)}{n_j} = \sum_{j=1}^{N} \frac{W_{ij}}{n_j} = 1. \tag{A.21}$$

Their plurality is given since a rather common weak side of most SPH Kernels is the problem of particle pairing instability (also known as crushing instability). Such instability comes out in the study of how the Kernel analytical formulation in the interpolation–integration (Eqs. (A.6) and (A.7)) affects the flow hydrodynamics, whenever the mutual distance between two flow particles $r_{ij} < h$ (Scüssler and Schmitt, 1981; Thomas and Couchman, 1992; Herant, 1994; Swegle et al., 1995; Lanzafame, 2010a, 2018; Springel, 2010; Dehnen and Aly, 2012; Price, 2012; Valizadeh and Monaghan, 2015; Shuangs et al., 2019).

One of the most adopted Kernel analytical formulations makes use of the cubic spline profile as a function of $q = r_{ij} h_i^{-1}$ (Monaghan, 1992) that is:

$$W_{3,ij} = \frac{1}{h^n} C \begin{cases} \left(1 - \frac{3}{2}q^2 + \frac{3}{4}q^3\right) & \text{for} \quad 0 \le q \le 1 \\ \frac{1}{4}\left(2 - q\right)^3 & \text{for} \quad 1 \le q \le 2 \end{cases} \tag{A.22}$$

In these expressions, $C = 2/3$, $10/(7\pi)$ or $1/\pi$ whenever the number of dimensions $n = 1$, 2 or 3, respectively. Further, more recent formulations (Wendland, 1995; Dehnen and Aly, 2012), still based on compact polynomial functions have also been proposed. Among these formulations, one of the simplest is

$$W_{1,ij} = \begin{cases} \frac{1}{h}\frac{5}{4}\left(1 - q\right)^3\left(1 + 3q\right) \\ \frac{1}{h^n} C \left(1 - q\right)^4\left(1 + 4q\right) \end{cases} \tag{A.23}$$

for $0 \le q \le 1$. The first expression is adopted in 1D. Among the several Wendland functions adopted in SPH (Dehnen and Aly, 2012), Eq. (A.23) in 3D has an integration domain strictly comparable to that of the B-Spline function Eq. (A.22) simply doubling the assigned h whenever it is assumed constant. This ensures the same extension of the integration domain in the two cases. Of course, whenever adaptive criteria are considered, any Kernel radial profile can be considered because the variability criteria on the smoothing length prevail on ensuring the same extension to the integration domain. Instead, $C = 7/\pi$ or $C = 21/(2\pi)$ whenever the number of dimensions $n = 2$ or 3, respectively. These are quite similar to Fulk and Quinn (1996)

$$W_{2,ij} = \begin{cases} \frac{1}{h}\frac{5}{32}\left(2 - q\right)^3\left(1 + \frac{3}{2}q\right) \\ \frac{1}{h^n} C \left(2 - q\right)^4\left(1 + 2q\right) \end{cases} \tag{A.24}$$

for $0 \le q \le 2$. The first expression is adopted in 1D. Instead, $C = 7/(16(102\pi))$ or $C = 21/(64(4\pi))$ whenever the number of dimensions $n = 2$ or 3, respectively. Instead, in the original SPH formulation Gaussian Kernel profiles were adopted:

$$W_{G,ij} = \frac{1}{(\pi^{1/2} h)^n} e^{-q^2} \tag{A.25}$$

with $n = 1$, 2 or 3, referring to the number of dimensions, but whose integral equals 1 for $-\infty \le q \le +\infty$. Starting from the original approach (Monaghan, 1992), a Kernel calculation (Lanzafame, 2010b, 2018) can be formulated as

$$W_{erf,ij} = \begin{cases} \frac{2}{\pi^{1/2} h} e^{-q^2} & \text{in 1D}, \\ \frac{1}{\pi^{3/2} hq} e^{-q^2} & \text{in 2D}, \\ \frac{1}{2\pi^{3/2} hq^2} e^{-q^2} & \text{in 3D}, \end{cases} \tag{A.26}$$

for $0 \le q \le +\infty$. The origin of such Kernel functions is in the Error Function:

$$erf(z) = \frac{2}{\sqrt{\pi}} \int_0^z e^{-q^2} dq, \tag{A.27}$$

whose Complementary Error Function is:

$$erfc(z) = 1 - erf(z) = \frac{2}{\sqrt{\pi}} \int_z^\infty e^{-q^2} dq. \tag{A.28}$$

For $z = 0$,

$$erfc(0) = 1 - erf(0) = \frac{2}{\sqrt{\pi}} \int_0^\infty e^{-q^2} dq = 1. \tag{A.29}$$

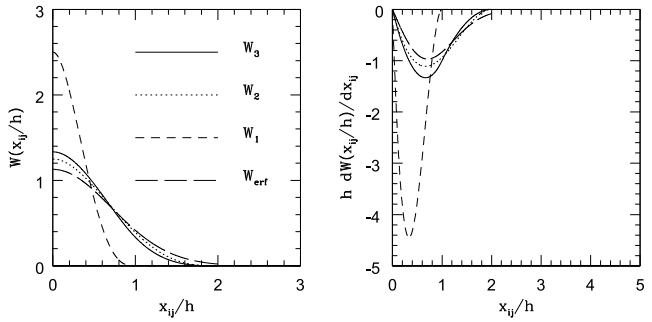

Fig. A.40. Radial profiles of 1D $W_{3,ij}$, $W_{1,ij}$, $W_{2,ij}$ and $W_{erf,ij}$ Kernels, as well as of their respective radial gradients. The $W_{erf,ij}$ profile is plotted only up to $x_{ij}h^{-1} = 2$ for a restricted comparison.

For $z = 0$, $erfc(0)$ equals the zero order Gaussian integral:

$$I_0 = \int_0^\infty e^{-vq^2} dq = \frac{1}{2}\frac{\sqrt{\pi}}{v}. \tag{A.30}$$

In performing 3D integral,

$$\int W_{erf,ij} d^3 r_{ij} = 4\pi \int_0^\infty \frac{1}{2\pi^{3/2} h r_{ij}^2} e^{-r_{ij}^2/h^2} r_{ij}^2 dr_{ij}$$
$$= \frac{2}{\sqrt{\pi}} \int_0^\infty e^{-q^2} dq = 1. \tag{A.31}$$

The formulation is based on the analytical expression of a typical 1D Gaussian profile, but also pays attention to the mathematical integration process in 2D and 3D naturally introducing geometric analytical terms: $2\pi r_{ij}$ and $4\pi r_{ij}^2$ which modify the entire radial profile of the "filtering function". That means, that in reality the working Kernel is no longer W_{ij} only (as in 1D), but $W_{ij}2\pi r_{ij}$ in 2D and $W_{ij}4\pi r_{ij}^2$ in 3D. In the conversion (Eq. (A.7)) of the integral (Eq. (A.6)) this means that n_j also plays a key role and that attention should be paid to the entire ratio $W_{ij}n_j^{-1}$.

Two things are relevant:

- Any correct $\nabla W_{ij} \to -\infty$ as $r_{ij} \to 0$, so that pressure forces physically correctly increase towards infinity, whenever the mutual spatial radial separation of two SPH particles reduces to zero. Whenever pressure forces are numerically too high in extreme accretion conditions in 2D and in 3D, the particle merging option is a practical solution to any numerical shortcoming.
- Even though the particle resolution length h is constant, any number of assigned companions can be accounted for, thanks to the fact that the Gaussian-based Kernel extension is theoretically unlimited. This is a widely used feature in a lot of 1D SPH exponential Kernels also working with a Gaussian profile (Fulk and Quinn, 1996; Liu et al., 2003; Hongbin and Xin, 2005; Cabezón et al., 2008). By adopting such a form of Kernels, all companions within a distance of $r_{ij} \sim 2h$ up to $r_{ij} \sim 3h$ are usually considered. However, if their number is smaller than the established assigned number, the radial extension is possible up to collect the wished number of companions to accomplish a satisfactory accuracy of integration.

These conclusions are shown in Figs. A.40 and A.41, where the radial profiles of $W_{3,ij}$, $W_{2,ij}$, $W_{1,ij}$ and $W_{erf,ij}$ Kernels are reported in 1D and in 3D, respectively, together with their radial spatial gradients. In particular, for the 3D integrations, their profiles multiplicated by $4\pi r_{ij}^2 h^{-2}$ are also shown.

The key role of $4\pi r_{ij}^2 h^{-2}$ is highlighted in Fig. A.41, where it is shown not only that the radial profile of $4\pi r_{ij}^2 h^{-2} W_{ij} \to 0$ as $r_{ij} \to 0$, but also their respective radial gradients behave the same way. This incorrect behaviour is at the origin of one of the reasons for 2D and 3D

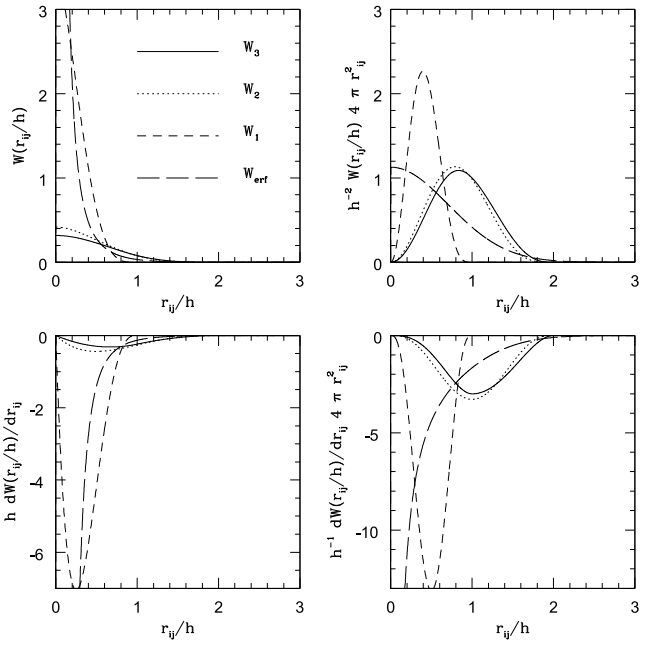

Fig. A.41. Radial profiles of 3D $W_{3,ij}$, $W_{2,ij}$, $W_{1,ij}$ and $W_{erf,ij}$ Kernels, as well as of their respective radial gradients in the two left-side panels. The same profiles multiplied by $4\pi r_{ij}^2 h^{-2}$ are also shown in the two right-side panels. The $W_{erf,ij}$ profile is plotted up to $r_{ij}h^{-1} = 2$ for a restricted comparison.

particle pairing instability, which is, instead, excluded in the case of a $W_{erf,ij}$ Kernel. This problem still exists in the 1D case, which means that the 1D simpler modelling cannot be physically correct whenever any adopted interpolation Kernel has an inflexion point in its radial profile since all closer particle companions show a non-physical behaviour.

The choice of the Error Function $W_{erf,ij}$ in Lanzafame (2010a, 2018) is strictly based only on physical bases (Monaghan, 1992) despite, any 1D Kernel could still be adopted as long as it could be multiplied by $(2\pi r_{ij})^{-1}$ in 2D and by $(4\pi r_{ij}^2)^{-1}$ in 3D. However, this implies a too large unphysical arbitrariness in the Kernel choice.

It is worth noting that any Kernel, like the Gaussian one, whose radial profile has an unlimited extension up to $+\infty$ needs a spatial truncation on how far extending the SPH spatial integration-interpolation is for convenience reasons. This inevitably introduces a truncation error, whose features have been discussed in Monaghan (1992), Quinlan et al. (2006), Vaughan et al. (2008), Vaughan (2009) and Liu and Liu (2010). Such an error decreases the consistency order of calculations. This is the ability of the SPH interpolation in reproducing both an analytical function describing the radial profile of some physical property and its first spatial derivative within the integration-interpolation domain extension (Amicarelli et al., 2011a,b). In such papers, it is shown that SPH polynomial Kernels show in the bulk flow a consistency whose order is 1–2 units less than the degree of the polynomial, as long as the particle distribution is uniform. This is accomplished without any discussion regarding any numerical aspect of physical conservation laws and numerical stability. Of course, the polynomial should be free of any exponential function. The order of such a consistency further decreases by one more unit at the boundaries (Amicarelli et al., 2011a,b; Sibilla, 2015). So, in the case of $W_{3,ij}$, $W_{2,ij}$ and $W_{1,ij}$, the order of consistency is 1–2 (that means a convergence and an accuracy of order $O(h^3)$ - $O(h^2)$) in the bulk of the fluid flow. Instead, they have a order of consistency of 0–1 (i.e. a convergence and an accuracy of order $O(h^2)$ - $O(h)$) at the boundaries. Instead, SPH Gaussian Kernels show an order of consistency of 0–1 throughout as long as the radial extension of integration is limited up to $2h$. This difficulty means that SPH results, obtained working with Gaussian Kernels or low-degree

Table A.1
$1-h_i^{-1}\sum_{j=1}^{N} W_{ij}n_j^{-1}\big|_{1D} \equiv 1-h_i^{-1}\sum_{j=1}^{N} W_{ij}\Delta x_j\big|_{1D}$ 1D numerical error computed for a uniform distribution of particle neighbours, according to the adopted SPH Kernel (Eqs. (A.22), (A.23), (A.24) and (A.26)). The particle spatial separation $\Delta x_j h_j^{-1} = (x_j - x_{j-1})h_j^{-1}$ is also shown, as well as the $x_j h_j^{-1}$ spatial window where each Kernel works. In 1D, it is here assumed that $\Delta x_j \equiv x_{ij} = x_j - x_i$. 0.0000000 values refer to numerical errors below 10^{-8}.

$1-h_i^{-1}\sum_{j=1}^{N} W_{ij}\Delta x\big\|_{1D}$					
	$W_{3,ij}\big\|_{1D}$	$W_{2,ij}\big\|_{1D}$	$W_{1,ij}\big\|_{1D}$	$W_{erf,ij}\big\|_{1D}$	$W_{erf,ij}\big\|_{1D}$
	$0 \le x_j h_j^{-1} \le 2$	$0 \le x_j h_j^{-1} \le 2$	$0 \le x_j h_j^{-1} \le 1$	$0 \le x_j h_j^{-1} \le 2$	$0 \le x_j h_j^{-1} \le 4$
$\Delta x_j h_j^{-1} = 0.5$	0.0000000	$-9.7656250\ 10^{-4}$	$-1.5625000\ 10^{-2}$	$1.1616349\ 10^{-3}$	$1.1920929\ 10^{-7}$
$\Delta x_j h_j^{-1} = 0.2$	0.0000000	$-2.4914742\ 10^{-5}$	$-4.0006638\ 10^{-4}$	$2.8848052\ 10^{-3}$	$5.9604645\ 10^{-8}$
$\Delta x_j h_j^{-1} = 0.1$	$1.7881393\ 10^{-7}$	$-1.5497208 \cdot 10^{-6}$	$-2.4914742\ 10^{-5}$	$3.7131906\ 10^{-3}$	$5.9604645\ 10^{-8}$
$\Delta x_j h_j^{-1} = 0.05$	$-1.1920929\ 10^{-7}$	$-1.1920929\ 10^{-7}$	$-1.5497208\ 10^{-6}$	$4.1782260\ 10^{-3}$	0.0000000
$\Delta x_j h_j^{-1} = 0.0\bar{3}$	$1.1920929\ 10^{-7}$	$1.1920929\ 10^{-7}$	$-1.1920929\ 10^{-7}$	$4.3407679\ 10^{-3}$	0.0000000
$\Delta x_j h_j^{-1} = 0.025$	$1.7881393\ 10^{-7}$	0.0000000	$-1.1920929\ 10^{-7}$	$4.4238567\ 10^{-3}$	$4.1723251\ 10^{-7}$
$\Delta x_j h_j^{-1} = 0.01$	$2.3841858\ 10^{-7}$	0.0000000	0.0000000	$4.4740438\ 10^{-3}$	$5.9604645\ 10^{-7}$

polynomials, are physically meaningful if working with small h, at the cost of large particle number density n as long as it is possible and at the cost of a longer computational time. This is, of course, unpractical! Indeed, a too-large mathematical arbitrariness in the choice of Kernel profiles disqualifies any physical aspect. Hence, it is important to discuss how far extending the SPH integration-interpolation Gaussian domain to find a reasonable practical radial extension for such a class of SPH Kernels, so that the consequences of such a truncation error are negligible. In order to do this, we analytically calculate the integral of Eq. (A.28) from $z = 2$ or from $z = 4$ up tp $+\infty$, to evaluate how much the dimensionless numerical error is in defect of the exact numerical value of the entire SPH integral (Eq. (A.28)) calculated from $z = 0$. This can be done using the asymptotic expansion of $erfc(z)$ as:

$$erfc(z) = \frac{e^{-z^2}}{z\sqrt{\pi}}\left[1 + \sum_{n=1}^{\infty}(-1)^n \frac{(2n)!}{n!(2z)^{2n}}\right] \tag{A.32}$$

which gives us

$$\begin{cases} erfc(2) \simeq 4.744\ 10^{-3} \\ erfc(4) \simeq 2.769\ 10^{-9} \end{cases} \tag{A.33}$$

limiting the summation in Eq. (A.32) up to the first four terms only. These errors have to be compared, at least in 1D, with the numerical errors computed by performing numerical integrations $1 - h_i^{-1}\sum_{j=1}^{N} W_{ij}n_j^{-1}\big|_{1D}$ for the adopted Kernels. This is made better considering a uniform spatial distribution of SPH companions, since a disordered spatial distribution provides statistically larger numerical errors (Amicarelli et al., 2011a,b; Sibilla, 2015). Such data errors, together with the spatial separation $\Delta x_j h_j^{-1} = (x_j - x_{j-1})h_j^{-1}$ of neighbours, are shown in Table A.1, whose irregular behaviour, especially for the smallest values, is due to the unavoidable numerical fluctuations coming out by each contribution in the summation.

Assuming as, free of any truncation error the three 1D polynomial Kernels here considered in Eqs. ((A.22), (A.23) and (A.24)), $erfc(2)$ and $1 - h_i^{-1}\sum_{j=1}^{N} W_{erf,ij}n_j^{-1}\big|_{1D}$ are comparable with each other for $0 \le x_{ij}h_i^{-1} \le 2$. In Table A.1, it is shown that the numerical integration is quite satisfactorily for $\Delta x_j h_j^{-1} \le 0.05$, in spite of its numerical limitations. Besides, we also highlight that their values are comparable with the highest values among those here shown in the same Table. This shows that the choice of a Gaussian Kernel whenever $0 \le x_{ij}h_i^{-1} \le 2$ is not the best as far as the truncation errors and the decrease of consistency are concerned. However, $erfc(4)$ is one or two order of magnitude smaller than $1 - h_i^{-1}\sum_{j=1}^{N} W_{erf,ij}n_j^{-1}\big|_{1D}$ for $0 \le x_j h_j^{-1} \le 4$. Therefore, the error relative to the truncation counterpart is much smaller than that relative to the numerical integration which, in turn, is comparable with the smallest errors among those shown in the same Table. Thus, as long as $0 \le x_{ij}h_i^{-1} \le 4$, SPH results obtained assuming $W_{erf,ij}$ are competitive against those obtained working with polynomial Kernels. Moreover, working with $W_{erf,ij}$, it is also possible to extend the upper limit of the integration without any further increase of h whenever the number of particle neighbours is considered low, improving the consistency of SPH calculations.

Kernels with compact support are resistant to particle pairing instability in so far as low compressibility flow models are considered. Instead, as long as dominant external force fields exist they contribute in hiding any Kernel shortcomings. The appearance of such particle crushing instability is strongly related to the point where the Fourier transform of the Kernel becomes negative (Dehnen and Aly, 2012). This mathematical reasoning takes its cue since the interpolation integral of Eq. (A.6) is a convolution integral. In this case, attention is paid to the Fourier Transform of the Kernel because in the continuum limit the interpolation integral coincides with the product of the Fourier Transforms of the two functions $A(r_{ij})$ and $W(r_{ij})$ of Eq. (A.6). As for 1D Gaussian Kernel $W_{erf,ij} \sim W(x_{ij}) = e^{-x_{ij}^2}$, its Fourier Transform leads to another Gaussian function as

$$F(k_{ij}) = \frac{1}{2\pi}\int_{-\infty}^{\infty} e^{-x_{ij}^2} e^{-ix_{ij}k_{ij}}\, dx_{ij} = \frac{1}{4\pi} e^{-k_{ij}^2/4}, \tag{A.34}$$

being k_{ij} and x_{ij} a Fourier couple. So that, no negative terms exist. In 2D, as well as in 3D, the 3D vectorial form of the Fourier Transform needs to be considered. As an example, in 3D, suppressing at the moment the subscripts ij, the Fourier Transform of W_{erf} is:

$$\begin{aligned} F(\mathbf{k}) &= \int W_{erf} e^{i\mathbf{k}\cdot\mathbf{r}} d\mathbf{r} \sim \int e^{-r^2} r^{-2} e^{i\mathbf{k}\cdot\mathbf{r}} d\mathbf{r} \\ &= \int_{-\infty}^{\infty} r^2 dr \int_0^{2\pi} d\phi \int_{-\pi/2}^{\pi/2} sin\theta e^{-r^2} r^{-2} e^{ikrcos\theta} d\theta \\ &= 2\pi \int_{-\infty}^{\infty} e^{-r^2} dr \int_{-\pi/2}^{\pi/2} sin\theta e^{ikrcos\theta} d\theta \end{aligned} \tag{A.35}$$

as the 1st integral is covariant under rotation. The volume element is covariant under rotation. The $\mathbf{k}\cdot\mathbf{r}$ and the e^{-r^2} exponent of W_{erf} are also covariant under rotation. Therefore, even if $\mathbf{k}$ is not oriented along the z axis, it is always possible to rotate the axis so that $\mathbf{k}$ is parallel to the z axis.

Thus, the Gaussian $r^2 W_{erf}$ radial component in Eq. (A.35) always leads to positive amplitudes in the 3D Fourier Transform calculations. Instead, the $\int sin\theta e^{ikrcos\theta} d\theta$ contribution involves phase and frequency terms.

The Wendland $-\nabla W_{1,ij} 4\pi r_{ij}^2$ shows a gradient pressure barrier in 3D (2D) much more compressed towards shorter radial distances in the continuum limit as shown in Fig. A.41. This is the first explanation concerning their better resistance to particle pairing instability than other compact radial profile Kernels. However, a depression in the same $-\nabla W_{1,ij} 4\pi r_{ij}^2$ radial profile anyway exists towards very short radial distances r_{ij}, as shown in the same picture. This happens because Wendland Kernels do not analytically diverge at $r_{ij} \to 0$ simulating a correctly ever-increasing pressure force as particle mutual separation goes to zero. This numerically prevents ever-increasing pressure forces as $r_{ij} \to 0$, which, instead, is a physically correct divergence. The analytical study of Fourier Transform of Kernels is not always analytically

possible being far more complicated by also considering in 3D and 2D the contributions coming from the vector calculus of $d^3\mathbf{r}_{ij}$ and $d^2\mathbf{r}_{ij}$ in the continuum limit. Indeed, the effective interpolation function in reality is not the Kernel alone, but the entire radial function $4\pi r_{ij}^2 W(r_{ij})$ in 3D and $2\pi r_{ij} W(r_{ij})$ in 2D. The interpolating radial profiles in the continuum limit should also include these modifications in 2D and in 3D even as far as the spatial gradients are concerned. This important aspect gives more relevance to the many farther neighbours existing near the edge of the computational interpolation-integration domain, whose pressure force excess could impact results in subsonic conditions.

However, in the case of Kernel $W_{erf,ij}$, whatever the numerical simulation concerns 1D, 2D or 3D fluid dynamics, the effective integral function of the interpolation integral deals with a Gaussian radial profile as $4\pi r_{ij}^2 W_{erf,ij}$ in 3D and $2\pi r_{ij} W_{erf,ij}$ in 2D always give the Gaussian function. Further mathematical details concerning the full Fourier Transform algebra of other Kernel radial profiles and their first spatial derivatives, together with either r_{ij}^2 or r_{ij} coming from $d^3\mathbf{r}_{ij}$ and $d^2\mathbf{r}_{ij}$ in the continuum limit, are not analytically possible. Not all functions have analytical Fourier Transforms. Thus, they are not considered since all arguments here exposed are more than enough.

Since any numerical deviation from the exact value shown in Eqs. ((A.20) and (A.21)) makes worse the SPH interpolation quality, a way of improving one unit the numerical consistency of SPH calculations is a renormalization of Eqs. ((A.6) and (A.7)) (Shepard, 1968; Libersky et al., 1993) as:

$$\langle A\rangle(\mathbf{r}) = \frac{\int_D \mathcal{A}(\mathbf{r}')W(\mathbf{r},\mathbf{r}',h)d\mathbf{r}'}{\int_D W(\mathbf{r},\mathbf{r}',h)d\mathbf{r}'} \tag{A.36}$$

and

$$\langle A\rangle_i = \frac{\sum_{j=1}^N \mathcal{A}_j n_j^{-1} W_{ij}}{\sum_{j=1}^N n_j^{-1} W_{ij}} \tag{A.37}$$

respectively. This renormalization process directly involves the mass-density ρ as long as Eq. (A.8) is used. It can also correctly be used whenever terms in the $\nabla\cdot\mathbf{v}$ occur (e.g. the continuity and the energy equations) since the divergence of a vector is a scalar. However, a further improvement in the numerical consistency can be obtained by correcting the SPH conversion of equations including spatial gradients and in particular the spatial gradients of gas pressure as in the momentum equation (Eq. (A.2)) as:

$$\nabla\langle A\rangle(\mathbf{r}) = \frac{\int_D [\mathcal{A}(\mathbf{r}') - \mathcal{A}(\mathbf{r})]\nabla W(\mathbf{r},\mathbf{r}',h)d\mathbf{r}'}{\int_D W(\mathbf{r},\mathbf{r}',h)d\mathbf{r}'}, \tag{A.38}$$

that is:

$$\nabla_i\langle A\rangle_i = \begin{cases} \dfrac{\sum_{j=1}^N (\mathcal{A}_j - \mathcal{A}_i) n_j^{-1} \nabla_i W_{ij}}{\sum_{j=1}^N n_j^{-1} W_{ij}} \\ \text{or} \\ \dfrac{\sum_{j=1}^N \left[\left(n_j^{-1}\mathcal{A}_j - n_i^{-1}\mathcal{A}_i\right)\nabla_i W_{ij}\right]}{\sum_{j=1}^N n_j^{-1} W_{ij}} \end{cases} \tag{A.39}$$

instead of Eqs. ((A.12) and (A.13)). Eqs. ((A.38) and (A.39)) are obtained by performing the 1st spatial derivative of Eqs. ((A.36) and (A.37)). Therefore, taking into account of both renormalizations of Eqs. ((A.37) and (A.39)) the consistency working with $W_{erf,ij}$ should improve throughout: up to $2-3$ in the bulk and up to $1-2$ at the boundaries or wherever the particle distribution is not uniform.

Even though some numerical tricks have been proposed with the aim of improving the SPH numerical consistency (Liu et al., 1995; Bonet and Lock, 1999; Dilts, 1999; Chen et al., 1999a,b,c; Chen and Beraun, 2000; Chen et al., 2001; Zhang and Batra, 2004; Liu and Liu, 2006; Fatehi and Manzari, 2011; Stranex and Wheaton, 2011; Sibilla, 2015; Gabbasov et al., 2017; Hu et al., 2017; Korzilius et al., 2017; Islam et al., 2018), those recipes, as well as Eqs. ((A.37) and (A.39)), fit as long as both the Kernel and its spatial gradient are both "smooth" spatial functions. Such a condition is still true for $W_{erf,ij}$ when working with 2D-3D Kernels. However, such a condition is no longer true in 2D-3D for ∇W_{erf} because of its divergence as $\lim_{\mathbf{r}\to\mathbf{r}'} \nabla W_{erf} = -\infty$ (Appendix A.1).

A still undiscussed aspect of any refinement is whether it correctly works only if the spatial neighbour distribution is uniform, which is peculiarity beyond the scope of this paper. A uniform neighbour spatial distribution is a condition better fulfilled whenever particles can easily come close to each other, a particular better achieved in high compressibility conditions. Instead, in the low compressibility conditions, whenever gas pressure forces prevent the approaching of particles, the radial distribution of neighbours is mainly concentrated on the tail of the integration-interpolation domain.

Some other Kernel profiles have more recently been proposed (Shuangs et al., 2019) as well as polynomial functions, based on hyperbolic-shaped (Yang et al., 2014) or double cosine profiles (Yang and Peng, 2014). However, even though some of these formulations for W_{ij} do not show any inflection point in their radial profile, a trick always possible is the shifting of any 1D analytic function by horizontally shifting its inflection point towards zero abscissae. However, in doing so, in 2D–3D modelling an incorrect radial profile of the interpolating function still occurs in the interpolation–integration process due to $d\mathbf{r}'$. As an example, considering the inner part of a hyperbolic Kernel (Yang et al., 2014) $W_{ij} \propto q^3 - 6q + 6$ for $0 \le q \le 1$, $W_{ij} 2\pi q \propto (2\pi q)(q^3 - 6q + 6)$ in 2D and $W_{ij} 4\pi q^2 \propto (4\pi q^2)(q^3 - 6q + 6)$ in 3D, both going to zero as $q \to 0$, as well as their first spatial derivative. Thus, neglecting this aspect, SPH integrations inevitably leads to the particle pairing instability as $q = r_{ij} h_i^{-1} \to 0$ and to spatial gradients excesses at the edge of the integration domain. The occurrence of such non-physical behaviours increases towards the desired continuum limit, the greater the number of neighbours.

Appendix B. Dissipation within the non-viscous CFD Euler equations in SPH

In its first formulation, SPH has been coded as a shock-capturing method since the stability of inviscid CFD solutions of strictly hyperbolic Euler equations (LeVeque, 1992; Hirsch, 1997; Fletcher, 1998) is obtained by introducing an artificial viscosity as a pressure fluid term if flow discontinuities must be solved (i.e. the Riemann problem). This approach is largely used for CFD problems, like transport phenomena or flow shearing instabilities. Such artificial viscosity terms are often written in terms of the Mach number that is the ratio of the macroscopic speed of mechanical propagation of perturbations within the fluid ($\mathrm{v}_l - \mathrm{v}_r = \Delta\mathrm{v}_{lr} \sim \mathrm{v}_{shock} \sim \mathrm{v}_{sig}$) to the sound speed c_s. v_l and v_r are the two speeds relative to the two left–right sides of the 1D Riemann problem. v_{sig} and c_s are respectively related to the square roots of the flow dynamical pressure ($\rho\mathrm{v}_{sig}^2/2$) and of the gas static pressure p. In doing so, any role of the choice of the reference frame is excluded since only thermodynamic characteristics are involved by considering macroscopic compression involving relative motions within the fluid itself. More recently, some SPH codes have also been written by using some shock fitting (also called shock tracking) Godunov schemes (Parshikov, 1999; Parshikov et al., 2000; Parshikov and Medin, 2002; Inutsuka, 2002; Imaeda and Inutsuka, 2002; Cha and Whitworth, 2003; Cha and Wood, 2016; Molteni and Bilello, 2003; Iwasaki and Inutsuka, 2011; Sugiura and Inutsuka, 2017). This other approach is, instead, specifically developed for better solving the Riemann problem in the CFD, suffering as less as possible from the so-called Gibbs effect (Gibbs, 1898, 1899), appearing mainly at the corners of the discontinuity velocity profiles.

B.1. Basic forms of artificial viscosity for ideal gases non-viscous SPH flows

As far as the SPH conversion of momentum and the energy equations (Eqs. (A.10) and (A.11)) are concerned, the effective pressure p^* also includes an additional small pressure term related to artificial

viscosity dissipation (Appendix A.1). Standing the State Equation for ideal gases

$$p = \overline{\mu}^{-1}(\gamma - 1)\rho\epsilon, \tag{B.1}$$

where $\overline{\mu}$ is the mean molecular weight, four fundamental formulations have been written in the past for p^* which inspired further recent variants as (Springel, 2005; Cullen and Dehnen, 2010; Hu et al., 2014; Gabbasov et al., 2017).

In the most popular and first in order of time of these basic contributions p_i^* for the ith particle is written as (Gingold and Monaghan, 1982a; Lattanzio et al., 1985; Monaghan, 1985, 1992):

$$p_i^* = p_i(1 + \eta_{ij}), \tag{B.2}$$

being $\eta_{ij} \ll 1$ and expressed as

$$\eta_{ij} = \alpha_* \mu_{ij} + \beta_* \mu_{ij}^2, \tag{B.3}$$

where

$$\mu_{ij} = \begin{cases} \frac{h\mathrm{v}_{ij}\cdot\mathbf{r}_{ij}}{c_{sij}(r_{ij}^2+\xi^2)} & \text{if } \mathbf{v}_{ij}\cdot\mathbf{r}_{ij} < 0 \\ 0 & \text{otherwise} \end{cases} \tag{B.4}$$

$c_{sij} = 0.5(c_{si} + c_{sj})$ and c_{si} is the sound speed of the ith particle, $\mathbf{r}_{ij} = \mathbf{r}_i - \mathbf{r}_j$, $\mathbf{v}_{ij} = \mathbf{v}_i - \mathbf{v}_j$, $\xi^2 \ll h^2$, $\alpha_* \approx 1$, $\beta_* \approx 2$ and $\rho_{ij} = 0.5(\rho_i + \rho_j)$. These α_* and β_* parameters of the order of the unity are usually adopted to damp oscillations past high Mach number shock fronts developed by non-linear instabilities (Boris and Book, 1973). While the linear term α_* is based on the gas viscosity, instead the Von Neuman–Richtmier β_* quadratic term is necessary to handle strong shocks. Even smaller α_* and β_* values was adopted by Meglicki et al. (1993) specifically for developing more turbulence. According to this approach, in the physically inviscid SPH gas dynamics, the angular momentum transport is mainly due to the artificial viscosity included in the pressure terms. This dissipation reduces shock fluctuations, together with an appropriate numerical thermal diffusivity contribution $\propto (U_j - U_j)c_{sij}\rho_{ij}^{-1}$, included in the right-side of Eq. (A.11) for $d\epsilon/dt$, where $U_i = \rho_i\epsilon_i$ (Monaghan, 1985, 1992; Monaghan and Lattanzio, 1985).

Working with the above-mentioned dissipation, since the SPH modelling of non-viscous shear flows (Price, 2008) and of inviscid accretion discs showed flow dynamics considerably affected by spurious effects of the viscous transport, a 2nd contribution in the form of a correction has been proposed to Eq. (B.5) by Balsara (1995) as:

$$\mu_{ij} = \begin{cases} \frac{h\mathrm{v}_{ij}\cdot\mathbf{r}_{ij}}{c_{sij}(r_{ij}^2+\xi^2)}(f_i + f_j) & \text{if } \mathbf{v}_{ij}\cdot\mathbf{r}_{ij} < 0 \\ 0 & \text{otherwise} \end{cases} \tag{B.5}$$

where the form function

$$f_i = \frac{|\nabla\cdot\mathbf{v}|_i}{|\nabla\cdot\mathbf{v}|_i + |\nabla\times\mathbf{v}|_i + 10^{-4}c_{si}h^{-1}} \tag{B.6}$$

takes into account both the local compression and the vorticity around the ith particle. $f_i \to 1$ wherever the compression is relevant, while $f_i \to 0$ wherever the vorticity is prevailing. This approach decreases the unphysical spread of the angular momentum in galactic discs (Steinmetz, 1996) up to 20 times and improves results for oblique shocks hitting density discontinuities, but it does not improve results on planar shocks. Further modifications have been proposed, paying attention to even quadratic forms of the artificial viscosity algebra (Gabbasov et al., 2017).

In Morris and Monaghan (1997) a 3rd fundamental SPH approach is that still considering the η_{ij} as shown in Eq. (B.3), where the parameter α_*, now calculated for each ith particle, is instead evolving according to a decay law as:

$$\frac{d\alpha_{*i}}{dt} = -\frac{\alpha_{*i} - \alpha_{*i}^\circ}{\tau_i} + S_i, \tag{B.7}$$

with $\alpha_{*i}^\circ \simeq 10^{-1}$. The characteristic time-scale of decay

$$\tau_i = hC^{-1}c_{si}^{-1}, \tag{B.8}$$

where $C \sim 0.1 - 0.5$ is a nondimensional parameter related to the reduction of the explicit Friedrichs–Courant–Lewy time-step (Courant et al., 1928), and the source term

$$S_i = \max(-\nabla\cdot\mathbf{v}, 0). \tag{B.9}$$

In the 4th fundamental contribution (Monaghan, 1997), specifically written for handling shock fronts in the CFD according to the Riemann problem, artificial viscosity is reformulated by considering the ith and the jth particles as the left and right states of the intermediate mutual contact interface so that the 1D Riemann problem is treated along the line joining them. Being the 1D CFD Euler equations written in a conservative form as:

$$\frac{\partial\mathbf{s}}{\partial t} + \frac{\partial\mathbf{f}}{\partial x} = 0, \tag{B.10}$$

and being the simplest Euler technique of integration

$$\mathbf{s}_i^{n+1} = \mathbf{s}_i^n - \frac{\Delta t}{\Delta x}[\mathbf{f}^*(\mathbf{s}_i - \mathbf{s}_{i-1}) - \mathbf{f}^*(\mathbf{s}_{i-1} - \mathbf{s}_i)], \tag{B.11}$$

the numerical fluxes (Martí et al., 1991) are given by

$$\mathbf{f}^*(\mathbf{s}_i, \mathbf{s}_j) = 0.5\left(\mathbf{f}_i^* + \mathbf{f}_j^* - \sum_{k=1}^{3}|\lambda_k^*\Delta\omega_k^*\mathbf{e}_k|,\right) \tag{B.12}$$

where $\mathbf{e}_k$ are the eigenvectors of the Jacobian matrix $\mathbf{J} = \partial\mathbf{f}/\partial\mathbf{s}$, λ_k^* is an average of $(\lambda_i^*, \lambda_j^*)$ and $\Delta\omega_k^*$ are the discontinuity jumps of $\mathbf{s}$ across the characteristics. The discontinuity jumps are written as

$$\mathbf{s}_j - \mathbf{s}_i = \sum_{k=1}^{3}\Delta\omega_k^*\mathbf{e}_k. \tag{B.13}$$

For 1D ideal flows the eigenvalues are v, v$-c_s$ and v$+c_s$ as far as the velocity is concerned. Assuming that the jump in the velocity across the characteristics could physically be $(\mathbf{v}_i - \mathbf{v}_j)\cdot(\mathbf{r}_i - \mathbf{r}_j)|\mathbf{r}_i - \mathbf{r}_j|^{-1} = \mathbf{v}_{ij}\cdot\mathbf{r}_{ij}r_{ij}^{-1}$ and that a signal velocity v_{sig} corresponds to the above eigenvalues, $|\lambda_k^*|\Delta\omega_k^*$ equals $\mathrm{v}_{sig}\mathbf{v}_{ij}\cdot\mathbf{r}_{ij}r_{ij}^{-1}$. Therefore, according to this approach similar to the Riemann problem,

$$\eta_{ij} = -\frac{K\mathrm{v}_{sig}\mathbf{v}_{ij}\cdot\mathbf{r}_{ij}}{\rho_{ij}r_{ij}}, \tag{B.14}$$

with the arbitrary constant $K \approx 1$. This formulation for η_{ij} should be used only for the SPH momentum equation. Instead, as far as the SPH energy equation is concerned, it should be written as

$$\begin{aligned}\frac{dE_i}{dt} = &-\sum_{j=1}^{N} m_j\left(\frac{p_i\mathbf{v}_i}{\rho_i^2} + \frac{p_j\mathbf{v}_j}{\rho_j^2}\right)\cdot\nabla_i W_{ij} + \mathbf{f}_i\cdot\mathbf{v}_i \\ &-\frac{K\mathrm{v}_{sig}e_{ij}^*\mathbf{r}_{ij}}{\rho_{ij}r_{ij}}\cdot\nabla_i W_{ij} + \\ &\sum_{j=1}^{N} m_j\left(\frac{\boldsymbol{\tau}_i\cdot\mathbf{v}_i}{\rho_i^2} + \frac{\boldsymbol{\tau}_j\cdot\mathbf{v}_j}{\rho_j^2}\right)\cdot\nabla_i W_{ij}\end{aligned} \tag{B.15}$$

instead of Eq. (A.11), with $e_{ij}^* = e_i^* - e_j^*$, where $e_i^* = 0.5(\mathbf{v}_i\cdot\mathbf{r}_{ij}r_{ij}^{-1})^2$.

Calculations of v_{sig} for the 1D Riemann problem in ideal flows are reported in Whitehurst (1995) based on results of Gottlieb and Groth (1988) and Toro (1992). By performing some numerical experiments, formulations such as

$$\begin{aligned}\mathrm{v}_{sig,i\to j} &= c_{si} - \mathbf{v}_i\cdot\mathbf{r}_{ij}r_{ij}^{-1} \\ \mathrm{v}_{sig,j\to i} &= -c_{sj} - \mathbf{v}_j\cdot\mathbf{r}_{ij}r_{ij}^{-1} \\ \mathrm{v}_{sig} &= \mathrm{v}_{sig,i\to j} - \mathrm{v}_{sig,j\to i} \\ &= c_{si} + c_{sj} - \mathbf{v}_{ij}\cdot\mathbf{r}_{ij}r_{ij}^{-1}\end{aligned} \tag{B.16}$$

are reported in Monaghan (1997) having considered the versus going from i to j.

B.2. Is a dissipative form for the state equation of ideal gases justified?

The solution of the Riemann problem in SPH deals with the Lagrangian calculations of flow discontinuity p and $\mathbf{v}$ at the interparticle contact surface among particles. This is also clearly shown in Parshikov (1999), Parshikov et al. (2000), Parshikov and Medin (2002), Inutsuka (2002), Imaeda and Inutsuka (2002), Cha and Whitworth (2003), Cha and Wood (2016), Molteni and Bilello (2003), Iwasaki and Inutsuka (2011) and Sugiura and Inutsuka (2017), where the new pressure p^* and velocity v^* are introduced in the Euler equations instead of p and v to obtain the new solutions compatible with inviscid flow discontinuities. Thus, a question arises on the particle pressures p_i and p_j in the formulation of the momentum and energy equations. The question is if their substitution with the Lagrangian solutions of the Riemann problem p_i^* and p_j^* (Eqs. (A.10) and (A.11)) is enough for interfacing SPH with a CFD Lagrangian Godunov-type technique, excluding any artificial viscosity adoption. That means whether a real physical dissipation could correctly be accounted for within the EoS for perfect gases. In a non-viscous CFD, such a physical dissipation is originated only from those irreversible time-reversal-free physical phenomena involving entropy, like the propagation of perturbations within the ideal fluid, occurring in the fluid dynamics. Molecular collisions are responsible for the propagation of signals to which we pay attention. However, any explicit reference to physical friction phenomena (Lanzafame, 2010b) is excluded.

Such a physical interpretation of dissipation in the pressure terms corresponds to a reformulation of the EoS for inviscid ideal gases, whose equation (Eq. (B.1)) should strictly be applied in the CFD when the gas components macroscopically do not collide with each other. Even better, gas components should macroscopically be static. In the case of macroscopic gas collisions, Eq. (B.1) modifies in:

$$p^\star = \overline{\mu}^{-1}(\gamma-1)\rho\epsilon + \text{other}. \tag{B.17}$$

The further term taking into account the velocity of perturbation propagation (Monaghan, 1997). This velocity equals the ideal gas sound velocity c_s for non-collisional gases in equilibrium or for rarefaction waves. Instead, it includes the compression velocity: $\mathbf{v}_{ij}\cdot\mathbf{r}_{ij}r_{ij}^{-1}$ in the occurrence of shocks ((B.16)). In the first case, we write the EoS for inviscid ideal gases as:

$$p = \frac{\rho}{\gamma}c_s^2, \tag{B.18}$$

where $c_s^2 = \gamma\overline{\mu}^{-1}(\gamma-1)\epsilon$. Instead, in the second case, the new formulation for the EoS is obtained squaring v_{sig}, so that $c_s^2(1-\mathrm{v}_{shock}c_s^{-1})^2$ is always an energy per unit mass in the case of a shock compression, with $\mathrm{v}_{shock} \equiv \mathbf{v}_i\cdot\mathbf{r}_{ij}r_{ij}^{-1} < 0$ involving the relative speed of a flow discontinuity of the Riemann problem between two close fluid particles i and j. The ratio $\mathrm{v}_{shock}c_s^{-1}$ is the necessary Mach number characterizing such a reformulation of damping . Hence:

$$p^\star = \begin{cases} \frac{\rho}{\gamma}c_s^2\left(1-\frac{\mathrm{v}_{shock}}{c_s}\right)^2 & \text{if } \mathrm{v}_{shock} < 0 \\ \frac{\rho}{\gamma}c_s^2 & \text{if } \mathrm{v}_{shock} \geq 0 \end{cases} \tag{B.19}$$

In the SPH scheme, being:

$$p_i^\star = \frac{\rho_i}{\gamma}c_{si}^2\left(1-\frac{\mathrm{v}_{shock,i}}{c_{si}}\right)^2, \tag{B.20}$$

$$\mathrm{v}_{shock,i} = \begin{cases} \frac{\mathbf{v}_{ij}\cdot\mathbf{r}_{ij}}{r_{ij}} & \text{if } \mathbf{v}_{ij}\cdot\mathbf{r}_{ij} < 0 \\ 0 & \text{otherwise.} \end{cases} \tag{B.21}$$

This formulation introduces the shock pressure term: $\rho(\mathrm{v}_{shock}^2 - 2\mathrm{v}_{shock}c_s)\gamma^{-1}$, whose linear and quadratic power dependence on $\mathbf{v}_{ij}\cdot\mathbf{r}_{ij}r_{ij}^{-1}$ is similar to the corresponding components of artificial viscosity terms of Eqs. ((B.2), (B.3) and (B.4)) necessary to handle flow discontinuities in the Riemann problem. Such damping terms, related to the macroscopic flow kinematics (as mentioned in Eqs. ((A.4) and (B.17))), are missing in static equilibrium flow conditions as shown in Eqs. ((B.1) and (B.18)). The linear term $\propto c_s\mathrm{v}_{shock}$ is based on the viscosity of a gas. The quadratic Von Neumann–Richtmyer-like term $\propto (c_s\mathrm{v}_{shock})^2$ is necessary to handle strong shocks. These contributions involve a dissipative power, whose effect corresponds to an increase in the gas pressure. Therefore, the formulation (Eq. (B.20)) can be used for $p_i^\star$ and $p_j^\star$ in the SPH formulation of the momentum and energy equations (Eqs. (A.10) and (A.11)).

It is noteworthy that this simple reformulation allows to keep the same Courant–Friedrichs–Lewy condition (Courant et al., 1928) as for the time-step computation, simply using $c_s - \mathrm{v}_{shock}$ instead of the sound velocity c_s.

By comparing the physically dissipative shock pressure term $\rho(\mathrm{v}_{shock}^2 - 2\mathrm{v}_{shock}c_s)\gamma^{-1}$ with $p_i\eta_{ij}$, relative to the SPH artificial viscosity, a physical equivalence for α^* and β^* parameters is:

$$\alpha^* = 2\frac{c_{sij}r_{ij}}{c_{si}h} \tag{B.22}$$

$$\beta^* = \frac{c_{sij}^2 r_{ij}^2}{c_{si}^2 h^2} = \left(\frac{\alpha^*}{2}\right)^2. \tag{B.23}$$

The linear and the quadratic dependence of α^* and β^* on $c_{sij}r_{ij}(c_{si}h)^{-1}$ perfectly correlates the physical dissipation of a perfect gas both to a bulk viscosity and to a quadratic Von Neumann–Richtmyer-like dissipation, able to handle strong shocks. Any dependence on the spatial resolution length h_i, contrary to the above-shown formulations for the SPH artificial viscosity, is avoided. In fact, both h_i and r_{ij} algebraically erase with each other applying Eqs. ((B.3), (B.4)). Compared to those SPH versions where $\alpha^* \sim 1$ and $\beta^* \sim 2$, such correlations show that α^* and β^* equal zero for $r_{ij} = 0$ and that $\alpha^* = 2$ and $\beta^* = 1$ in a homogeneous and isotropic gas in which the particle mutual spatial radial separation $r_{ij} = h$. Both parameters linearly and quadratically variate, respectively, varying either $r_{ij}h^{-1}$, or $c_{sij}c_{si}^{-1}$, or both. Thus, both α^* and β^* decrease for closer particle neighbours and/or for colder particle neighbours, whose $c_{sj} < c_{si}$.

This first step shows that a necessary dissipation, free of any dependence on the spatial resolution length, is still possible in the form of either Eq. (B.20), or as shown (Monaghan, 1997) in the 4th formulation reported at the end of Appendix B.1. But this is a result that, as it is, could only be mathematically meaningful. Therefore, the next step is the understanding of whether a real physical reformulation of the EoS for perfect gases, including the dissipation produced by the propagation of perturbations, is physically meaningful or not (Lanzafame, 2010b).

In order to do this, it is necessary to evaluate the consequences of the physical dissipation of a shock wave on the Maxwell–Boltzmann statistical thermodynamics of a system whose thermodynamic properties in thermal equilibrium are described by the partition function Z (Reif, 1965; McLelland, 1973):

$$Z = \sum_i^{energy-levels} G_i e^{-\beta U_i} = \sum_j^{shock-quantum-state} e^{-\beta U_j} = \sum_j^{complexions} e^{-\beta U_j}. \tag{B.24}$$

The most probable distribution in the ensemble with energies U_i and with quantum states of the system given by the Maxwell–Boltzmann law, are:

$$\overline{n}_i = G_i e^{-\alpha}e^{-\beta U_i} \tag{B.25}$$

and

$$\overline{m}_j = e^{-\alpha}e^{-\beta U_j} \tag{B.26}$$

respectively, where $e^{-\alpha} = ZN^{-1}$, being $N = \sum_i n_i$ the total number of systems in the ensemble, $U = \sum_i n_i U_i$ the total energy of the ensemble and being G_i the degeneracy of the energy level U_i. Physically meaningful Z involves the parameter $\beta > 0$. $\beta = (\mathcal{K}_B T)^{-1}$, where $\mathcal{K}_B$ is

the Boltzmann constant and T is the temperature. Being ($U_i \propto \mathrm{v}_i^2$) for having classically non-interacting free atoms, without considering their internal energy levels, each exponential in the summations is related to a Gaussian distribution function.

Since fluid dynamics equilibrium conditions are a special case, the application of thermodynamic laws is an evident approximation, in particular whenever not reversible events occur like shock waves. We assume the hypothesis that even in conditions of a fluid motion, the Maxwell–Boltzmann Law still holds, where the net effect of any physical dissipation is to reduce the peak value of the Maxwell–Boltzmann distribution, widening its spread, conserving both N and U. Hence, any physical dissipation is introduced as a $0 < D \leq 1$ term ($D = 1$ involves no dissipation) multiplying βU_i or βU_j in the above exponentials as $\beta D U_i$ or $\beta D U_j$, so that:

$$Z = \sum_{i}^{energy-levels} G_i e^{-\beta D U_i} = \sum_{j}^{shock-quantum-state} e^{-\beta D U_j} = \sum_{j}^{complexions} e^{-\beta D U_j}. \tag{B.27}$$

This is necessary to determine the wished result, without any alteration of the system's degeneracy, which cannot be considered as long as we are dealing with an ideal gas. In a microscopic description, physical dissipation irreversibly converts ordered kinetic energy into chaotic kinetic energy, that is the conversion of macroscopic kinetic energy into thermal energy, as long as the thermodynamic system is always in thermal equilibrium, obeying Markovian statistics. Atoms or molecules do not interact with each other, and their internal quantum energies do not affect global thermodynamics. In the Maxwell–Boltzmann distribution hypothesis, this implies a transition from one Maxwell–Boltzmann statistical distribution to another one, whose half weight at half height is larger. This transition occurs during the shock crossing, while the whole thermodynamic system makes an instantaneous transition between two thermodynamic equilibrium states. Hence, the larger the half weight at half height of the statistical distribution the larger the physical dissipation. Thus, writing $\beta^\star = D(\mathcal{K}_B T^\star)^{-1}$ or, that is the same:

$$\beta^\star = D\beta = D(\mathcal{K}_B T)^{-1}, \tag{B.28}$$

$$Z = \sum_{i}^{energy-levels} G_i e^{-\beta^\star U_i} = \sum_{j}^{shock-quantum-state} e^{-\beta^\star U_j} = \sum_{j}^{complexions} e^{-\beta^\star U_j}. \tag{B.29}$$

The net effect of such dissipation is the wished widening of the width at half height of each Gaussian distribution of Z, conserving both N and U. Thermodynamic properties are obtained (Reif, 1965; McLelland, 1973) in the same way as they are currently given using $\beta^\star$ instead of β as:

- Internal Energy:

$$U^\star = -\frac{\partial \ln Z/\partial T|_V}{\partial \beta^\star/\partial T|_V} = \left(\frac{\mathcal{K}_B T}{D} - \frac{1}{\beta}\frac{\mathcal{K}_B T}{\partial D/\partial T|_V}\right)\frac{\partial \ln Z}{\partial T}\Big|_V \tag{B.30}$$

keeping fixed the volume V;

- Entropy:

From the Boltzmann law,

$$S^\star = -\frac{\mathcal{K}_B N}{D}\ln Z + \frac{U^\star}{T}; \tag{B.31}$$

- Free Helmholtz Energy:

$$F^\star = U^\star - TS^\star = -\frac{N\mathcal{K}_B T}{D}\ln Z; \tag{B.32}$$

- Pressure:

In the hypothesis that dissipation does not explicitly depend on V,

$$p^\star = -\frac{\partial F^\star}{\partial V}\Big|_T = \frac{N\mathcal{K}_B T}{D}\frac{\ln Z}{V}\Big|_T. \tag{B.33}$$

In the classical case of free, non-interacting atoms, $\partial \ln Z/\partial V|_T = 1/V$, hence

$$p^\star = \frac{N}{\beta^\star}\frac{1}{V}. \tag{B.34}$$

Thus, by Eq. (B.28),

$$p^\star = N\frac{\mathcal{K}_B T}{V}\frac{1}{D}. \tag{B.35}$$

Assuming $D = (1 - \mathrm{v}_{shock,i} c_{si}^{-1})^{-2} \leq 1$, $\mathrm{v}_{shock,i} = \mathbf{v}_{ij}\cdot\mathbf{r}_{ij} r_{ij}^{-1}$ if $\mathbf{v}_{ij}\cdot\mathbf{r}_{ij} < 0$ and $\mathrm{v}_{shock,i} = 0$, otherwise we write an expression that does not depend on volume V and corresponding to a function that, even depending on T, it can be easily handled by considering the derivatives in Eq. (B.33). Thus, the EoS is:

$$p^\star = \begin{cases} \frac{N\mathcal{K}_B T}{V}\left(1 - \frac{\mathrm{v}_{shock,i}}{c_{si}}\right)^2 & \text{if } \mathrm{v}_{shock} < 0, \text{ i.e. } D < 1 \\ \frac{N\mathcal{K}_B T}{V} & \text{if } \mathrm{v}_{shock} \geq 0, \text{ i.e. } D = 1 \end{cases} \tag{B.36}$$

physically corresponding to the EoS for ideal flows, even taking into account a shock occurrence. Enthalpy and Gibbs free energy are given by: $H^\star = U^\star + p^\star V$ and $G = U^\star + p^\star V - TS^\star$.

In order to generalize, we need only one general EoS and not a splitting of the EoS according to the kinematic of the flow. In that regard, we can generalize the EoS: $p^\star = \rho c_s^2 (1 - \mathrm{v}_{shock} c_s^{-1})^2 \gamma^{-1}$ as:

$$p^\star = \frac{\rho}{\gamma} c_s^2 \left(1 - C\frac{\mathrm{v}_R}{c_s}\right)^2, \tag{B.37}$$

where $C \to 1$ for $\mathrm{v}_R = \mathbf{v}_{ij}\cdot\mathbf{r}_{ij}|\mathbf{r}_{ij}|^{-1} < 0$, whilst $C \to 0$ otherwise. A simple empirical formulation can be,

$$C = \frac{\mathcal{K}}{\pi}\mathrm{arccot}\left(R\frac{\mathrm{v}_R}{c_s}\right), \tag{B.38}$$

where $R \gg 1$ is a large number describing how much the flow description corresponds to that of an ideal gas. In this regard, $R \approx \lambda/d$, being $\lambda \propto n^{-1/3} = (\rho \mathcal{N}_\mathcal{A} \overline{\mu}^{-1})^{-1/3}$ the molecular mean-free-path, d the mean linear dimension of gas molecules and $\mathcal{K}$ is a free dimensionless parameter to be tuned so that $p^* p^{-1} - 1 \sim 10^{-6}$-$10^{-5}$ or less.

Although the physical meaning of v_R in the field of a free Lagrangian particle technique is clear, it could be controversial in an Eulerian description. In this case, the local physical properties have to be considered because it is necessary to correlate the approaching of two particles to a local compression. In order to convert Eq. (B.37) to a more general form (Lanzafame, 2010b), we pay attention to the continuity equation regarding the numerical concentration n as:

$$\frac{dn}{dt} = -n\nabla\cdot\mathbf{v} \tag{B.39}$$

to get v_R as:

$$\mathrm{v}_R = \frac{dn^{-1/3}}{dt} = -\frac{1}{3}n^{-4/3}\frac{dn}{dt} = \frac{1}{3}n^{-1/3}\nabla\cdot\mathbf{v}, \tag{B.40}$$

so that Eq. (B.37) can also be written as:

$$p^\star = \frac{\rho}{\gamma} c_s^2 \left(1 - C\frac{n^{-1/3}\nabla\cdot\mathbf{v}}{3c_s}\right)^2, \tag{B.41}$$

where

$$C = \frac{\mathcal{K}}{\pi}\mathrm{arccot}\left(R\frac{n^{-1/3}\nabla\cdot\mathbf{v}}{3c_s}\right). \tag{B.42}$$

EoS for ideal gases written as Eqs. ((B.36), (B.37) or (B.41)) are equivalent and effective strictly in order to solve the Riemann problem (Lanzafame, 2010b). However working with Eq. (B.41), even in a Lagrangian description, the physical dissipation is activated only

whenever a local compression occurs even for the inviscid ideal shear flows, despite the lack of any shock. In a Lagrangian framework, this is a significantly different mechanism of ignition of dissipation than the activation by the approaching of two particles with each other.

Looking at the correlation of physical dissipation with α^* and β^* SPH parameters, a dissipation still occurs even though dissipation depends on local thermodynamic conditions. This is an advantage compared with classical SPH. Such a difficulty, more limited than that rising in SPH whatever is the shock-capturing technique adopting a Lagrangian collisional approach for dissipation, is absent in the form of Eq. (B.41), because it is free of any dissipation whenever $\nabla \cdot \mathbf{v} \geq 0$. As an example, any non-viscous Keplerian isothermal annular ring flow fictitiously free of any gas static pressure, where $\nabla \cdot \mathbf{v} = 0$, shows a very slow radial spreading (Lanzafame, 2010b) with a statistically negligible deviation from the strictly Keplerian kinematics because of a very poor numerical dissipation.

In the form of Eq. (B.41), the reformulated EoS for non-viscous ideal gases includes a dissipation having also a physical motivation, depending on the general local kinematic conditions, which is activated only when a local compression occurs. A dissipation in SPH-based techniques, also depending on the local kinematic conditions around each ith particle, has also been proposed by Cullen and Dehnen (2010), but still in the key of artificial viscosity.

According to Eq. (B.41), also right for shear flows, the algebraic relations determining the α^* and β^* parameters are:

$$\alpha^* = 2\frac{c_{sij}}{c_{si}}\frac{n_i^{-1/3}}{h}\frac{\nabla \cdot \mathbf{v}_i}{\mathbf{v}_{ij} \cdot \mathbf{r}_{ij}} r_{ij}^2 \tag{B.43}$$

$$\beta^* = \frac{c_{sij}^2}{c_{si}^2}\frac{n_i^{-2/3}}{h^2}\left(\frac{\nabla \cdot \mathbf{v}_i}{\mathbf{v}_{ij} \cdot \mathbf{r}_{ij}}\right)^2 r_{ij}^4 = \left(\frac{\alpha^*}{2}\right)^2. \tag{B.44}$$

Such relations compare with Eqs. ((B.21) and (B.23)), respectively, in the case of a pure Riemann problem in fluid dynamics (Siegler and Riffert, 2000), being $\nabla \cdot \mathbf{v}_i \sim \mathbf{v}_{ij} \cdot \mathbf{r}_{ij} h r_{ij}^{-2}$.

In this Subsection it has been discussed the rationale leading to the physical inclusion of flow damping within the perfect gas EoS. Such a flow damping is used within an artificial viscosity formulation suitable for handling the Riemann problem, starting from Eq. (B.16) for v_{sig} in the occurrence of shocks. Such effort led to the formulation of an inactive damping in shear flows free of any local compression and activated in a Lagrangian framework only wherever head-to-head particle collisions locally occur as $\nabla \cdot \mathbf{v} < 0$. Therefore, as a rough conclusion, it is as if an artificial viscosity formulated for handling the Riemann problem is physically incorporated in the EoS excluding any inadequacy coming from single collisions in the Lagrangian approach.

Appendix C. A conservative form of compressible adaptive SPH

C.1. Some generalities on compressible adaptive SPH

In the SPH compressible CFD, the Kernel spatial derivatives are necessary for the computation of the Lagrangian time derivatives of ρ, ϵ, and $\mathbf{v}$ through a spatial interpolation-integration process, followed by a temporal integration procedure. The usefulness of an adaptive SPH (ASPH) arises from the need of counting a sufficiently adequate number of companions to calculate a significant interpolation integral (Eqs. (A.6) and (A.7)), whenever a compact spatial support Kernel is adopted.

Through a physical approach (Monaghan, 1992; Fulbright et al., 1995; Shapiro et al., 1996; Owen et al., 1998; Liu et al., 2006) the smoothing length h_i has been considered as a function of time by relating it to the local particle number density as:

$$h_i^{n+1} = h_i^n \left(\frac{\rho_i^n}{\rho_i^{n+1}}\right)^{1/3} \tag{C.1}$$

in 3D, where index n refers to time-step (Hernquist and Katz, 1989; Nelson and Papaloizou, 1993, 1994; Fulbright et al., 1995; Shapiro et al., 1996; Owen et al., 1998; Liu et al., 2006). Such a choice is widely considered better than:

$$h_i^n = h_i^\circ \left(\frac{\rho_i^\circ}{\rho_i^n}\right)^{1/3} \tag{C.2}$$

where h_i° and ρ_i° refer to initial values at time zero. Such a preference is because of non-linear instabilities occurring in anisotropic volume changes and flow distortions (Miyama et al., 1984). Equivalently, a further equation able to compute the new h_i at time-step $n+1$ from the old h_i at time-step n in 3D (Fulbright et al., 1995; Shapiro et al., 1996; Owen et al., 1998; Liu et al., 2006) is:

$$h_i^{n+1} = h_i^n \left[1 + \frac{1}{3}(\nabla \cdot \mathbf{v})_i \Delta t^n\right] \tag{C.3}$$

or, by considering the continuity equation:

$$h_i^{n+1} = h_i^n \left[1 + \frac{1}{3}\left(-\frac{1}{\rho_i}\frac{d\rho_i}{dt}\right)\Delta t^n\right]. \tag{C.4}$$

A spatial and temporal smoothing length, together with an appropriate symmetrization concerning particle pairs, have also been proposed (Evrard, 1988; Hernquist and Katz, 1989; Nelson and Papaloizou, 1993, 1994; Fulbright et al., 1995; Shapiro et al., 1996; Owen et al., 1998; Liu et al., 2006).

Instead, according to a different path (e.g. Benz et al., 1990), several authors adopted a criterion where the number of neighbours for each time-step calculation is an assigned number, decoupling the calculation of h_i for each time-step by any physical quantity. In that regard, it is always possible the exact counting of an assigned number of companions based on the calculation of their radial distance. This is a procedure that involves some computational time. However, it is also possible a more practical statistical algorithm as:

$$\begin{cases} h_i = \frac{N_p}{n_i} l^{-1} & \text{in 1D,} \\ h_i = \left(\frac{N_p}{\pi n_i}\right)^{1/2} l^{-1} & \text{in 2D,} \\ h_i = \left(\frac{3N_p}{4\pi n_i}\right)^{1/3} l^{-1} & \text{in 3D,} \end{cases} \tag{C.5}$$

where N_p is the assigned number of neighbours and l is the ratio between the full radial extension of the Kernel domain to h_i. The assigned number of neighbours in the 3D modelling has steadily increased from 30–50 in the 90s, up to 200–300 with the aim of improving the accuracy of SPH integrations at the cost of much longer computational times and excessive damping due to artificial viscosity (Eq. (B.3)).

In the ASPH, it is customary to make the averaging of i, j indexes, where the evaluation of a symmetrized

$$W_{ij} = W(r_{ij}, h_{ij}), \tag{C.6}$$

where

$$h_{ij} = 0.5 \cdot (h_i + h_j) \tag{C.7}$$

Evrard (1988) (the most frequently adopted), or

$$W_{ij} = 0.5 \cdot (W(r_{ij}, h_i) + W(r_{ij}, h_j)) \tag{C.8}$$

Hernquist and Katz (1989) are considered to compute the SPH spatial derivatives in Eq. (A.8) and in the Euler equations (Eqs. (A.9)–(A.11)). As those equations clearly show, the spatial resolution length h_i has a role through W_{ij}, in the calculation of the evolutionary explicit time-step through the Courant–Friedrichs–Lewy condition (Courant et al., 1928; Monaghan, 1992). Moreover, it also locally affects the necessary artificial dissipation playing a role in the particle collisions (Monaghan, 1992; Whitehurst, 1995).

The Kernel spatial derivatives, for the same particle configuration, on the same ith particle, differ from each other according to the adopted interpolation Kernel and according to the spatial resolution length adaptivity criterion. This occurs as much as farther from the

continuum limit is the distribution of companions because the SPH integration errors depend on three components: h_i, the neighbour number N_n and their spatial distribution (Vaughan et al., 2008; Vaughan, 2009; Zhu et al., 2015). So, in principle, for a Kernel profile free of any Gaussian relationship, it is not sure whether the greater it is N_n, the smaller the interpolation-integration errors because $N_n \to \infty$ as $h_i \to \infty$, while errors ($\propto N_n^{-1/2}$) should decrease to zero even as $N \to \infty$ while $h_i \to 0$ in the continuum limit. On this aspect, the continuum limit should be fulfilled as $N_n \to \infty$ whatever is h_i, that is in the limit of a very high particle number density, not increasing h_i indefinitely.

Non-isotropic ASPH (Shapiro et al., 1996; Owen et al., 1998; Liu et al., 2006) adopt an anisotropic algorithm to compute ellipsoid particle deformation and the anisotropic smoothing length, according to the local particle concentration. Such a scheme is mainly used in simulations of 2D and 3D oblique shocks and of contact fluid surfaces. The algorithm computes the element $h_{\alpha\beta i}$, where $\alpha, \beta = x, y, z$, of the 3×3 symmetric matrix:

$$h_{\alpha\beta i}^{n+1} = h_{\alpha\beta i}^{n} \left[1 + \frac{0.5}{3} \left(\frac{\partial \mathrm{v}_{i\alpha}}{\partial x_\beta} + \frac{\partial \mathrm{v}_{i\beta}}{\partial x_\alpha} \right) \Delta t^n \right], \tag{C.9}$$

where $h_{\alpha\beta i} = h_{\beta\alpha i}$, is the projection of the ellipsoid characteristic semiaxes on the Cartesian axes. The eigenvectors of the matrix are the directions along the three axes of the ellipsoid, and the corresponding eigenvalues are the dimensions of the ellipsoid along each axis. The determinant of the same matrix determines the normalization volume of each particle.

The SPH conversion of Eq. (C.4), similar to the SPH expression of the $\nabla \cdot \mathbf{v}$ (Monaghan, 1985, 1992) is:

$$h_{\alpha\beta i}^{n+1} = h_{\alpha\beta i}^{n} \left[1 + \frac{0.5 \Delta t^n}{3} \sum_{j=1}^{N} \frac{m_j}{\rho_i} \left(\mathrm{v}_{\alpha ij} \nabla_{i\beta} W_{ij} + \mathrm{v}_{\beta ij} \nabla_{i\alpha} W_{ij} \right) \right]. \tag{C.10}$$

C.2. Conservative ASPH formulation

Nelson and Papaloizou (1993, 1994) showed that the energy conservation improves if $\partial/\partial h$ are introduced into both SPH momentum and energy equations. The inclusion of such terms significantly modifies such equations in an unpractical form. The formal difficulties were overcome by Springel and Hernquist (2002) who derived an effective ASPH conversion of the pressure gradient contribution in the momentum equation (Eq. (A.10)), conserving energy and entropy, according to the conservative ASPH equation:

$$\frac{d\mathbf{v}_i}{dt} = -\sum_{j=1}^{N} m_j \left(f_i \frac{p_i}{\rho_i^2} \nabla_i W_{ij,i} + f_j \frac{p_j}{\rho_j^2} \nabla_j W_{ij,j} + \Pi_{ij} \nabla_i W_{ij} \right) + \sum_{j=1}^{N} m_j \left(\frac{\boldsymbol{\tau}_i}{\rho_i^2} + \frac{\boldsymbol{\tau}_j}{\rho_j^2} \right) \cdot \nabla_i W_{ij} + \mathbf{f}_i, \tag{C.11}$$

where $f_i = \left(1 + \frac{h_i}{3\rho_i} \frac{\partial \rho_i}{\partial h_i} \right)^{-1}$, $W_{ij,i} = W(r_{ij}, h_i)$ and Π_{ij} refers to the shock capturing dissipative contributions (Appendix B). Smoothing length h_i is computed requiring that a fixed mass is contained within a "smoothing volume": $(4\pi/3) h_i^3 \rho_i = M_{i,j}$ where $M_{i,j} = m_j N_{i,j}$ refers to the global mass of $N_{i,j}$ neighbours related to the ith particle. Each particle neighbour has a m_j mass. No further modifications to the energy equation are required. In a further paper (Monaghan, 2002) similar conclusions were reached to achieve better energy and entropy conservation.

The $\partial \rho_i / \partial h_i$ term is easily connected to the $\partial W_{ij}/\partial h_i$ by the simple relation:

$$\frac{\partial \rho_i}{\partial h_i} = \sum_{j=1}^{N} m_j \frac{\partial W_{ij}}{\partial h_i}, \tag{C.12}$$

where the derivative $\partial W_{ij}/\partial h_i$ also involves the derivative of the h_i^{-3} in 3D as: $\partial (W_{ij} h_i^{-3})/\partial h_i$. As far as the conservative ASPH energy balance equation for the total energy E is concerned,

$$\frac{dE_i}{dt} = -\sum_{j=1}^{N} m_j \left(f_i \frac{p_i \mathbf{v}_i}{\rho_i^2} \cdot \nabla_i W_{ij,i} + f_j \frac{p_j \mathbf{v}_j}{\rho_j^2} \cdot \nabla_j W_{ij,i} + \boldsymbol{\Omega}_{ij} \cdot \nabla_i W_{ij} \right) + \mathbf{f}_i \cdot \mathbf{v}_i + \sum_{j=1}^{N} m_j \left(\frac{\boldsymbol{\tau}_i \cdot \mathbf{v}_i}{\rho_i^2} + \frac{\boldsymbol{\tau}_j \cdot \mathbf{v}_j}{\rho_j^2} \right) \cdot \nabla_i W_{ij}, \tag{C.13}$$

where $\boldsymbol{\Omega}_{ij}$, includes shock-capturing dissipative terms (Appendix B).

C.3. ASPH lights and shadows

Adaptive techniques are used in compressible CFD whenever the spatial resolution length needs a reorganization to have local numerical solutions better describing both the fine structures and the temporal evolution of the flow. In this regard, even the SPH is no exception whenever spatially finite interpolation-integration Kernel domains are adopted. However, looking at the formulation of CFD equations in the SPH framework, the key role of both h and of the Kernel profile is undoubted, as well as the influence of how many companions are accounted for in the SPH integrations and their spatial distributions. Therefore, any adaptivity of h inevitably leads to both improvements and worsening of results.

- The good
  Working with a spatially finite interpolation-integration domain Kernel, the accounting of an adequate number of neighbours in ASPH gives a better quality of interpolations than in an SPH working with a constant h, especially whenever a particle rarefaction occurs. In such events, those particles, representing either a rarefaction wave or an expanding free surface towards the vacuum space, still interact with each other in ASPH. Instead, this no longer happens in SPH from a certain point onward, so that those noninteracting SPH particles wrongly adiabatically keep their heat. Moreover, whenever a particle compression occurs, the reduction of h in ASPH still allows a satisfactory interpolation-integration mitigating the problem of particle crushing instability, affecting the closest neighbours, because of their statistical reduction.
- The bad
  h_i-depending damping are involved within the SPH-ASPH formulation of energy and momentum equations. This happens either explicitly as a shock-capturing method or implicitly through the adoption of a Godunov-type scheme (Appendix B.1). Therefore, either an incorrect too-low damping works as $h_i \to 0$ or a too viscous flowing occurs as $h_i \to \infty$. In these two cases, the effect of damping of artificial dissipation could even be negligible in the first case, leading to unstable wrong numerical solutions, or it could even alter the inviscid fluid condition itself in the second case. In such extreme situations, either the clumping of the closest particles or the splitting particles in daughter particles are made in a refinement process. In the first case, the particle clumping occurs whenever the particle number density n_i exceeds an arbitrary threshold, limiting at the same time the particle crushing instability. In the second case, the particle splitting occurs in low-density regions whenever the accounting of neighbours reaches a low (and arbitrary) threshold, avoiding a too large swelling of their interaction radial domains (Meglicki et al., 1993; Børve et al., 2001, 2005; Lastiwka et al., 2005; Feldman and Bonet, 2007; Reyes López et al., 2013; Barcarolo et al., 2014; Spreng et al., 2014; Khorasanizade and Sousa, 2016; Vacondio et al., 2013, 2016; Liu et al., 2018; Wang et al., 2019). Although such

numerical algorithms are formulated to be mass, momentum, and energy conservative, unavoidable, however small, errors in the conservation laws are made. This happens because for the new particles coming out from the particle refinements, the only exact values of energy are those of their respective potential energies, assigned by their position coordinates. Instead, the spatial distributions of their kinetic and thermal energies are not uniquely established. These errors cumulate with those coming numerically from the corrective terms f_i, f_j (Eqs. (C.11) and (C.13)). In the case of particles coalescing, instead, the conservation of mass, momentum, and energy are better handled, despite a small variation of the new local physical properties, at the same time-step, after the coalescence of particles.

Nowadays damping can even be enforced by empirically tuning some arbitrary free parameters that regulate the dissipation as a function of the local physical conditions of the fluid. But, more importantly, such switches do not distinguish between binary head-to-head particle collisions and binary shear-particle collisions in a 2D-3D Lagrangian description.

- The ugly

Two are the main difficulties occurring working with an ASPH by using a polynomial Kernel within a spatial finite interpolation domain.

The first deals with the symmetrization required by Eqs. ((C.11), (C.12) and (C.13)) needed to ensure the conservation laws; otherwise the mutual interaction between the particle pair (i, j) is ruled by different Kernel spatial derivatives, giving an imbalance in the calculation of ∇p and $\nabla\cdot\mathbf{v}$. An unsolved conflict exists between this assignment and the calculation of h_i for each particle, according to those algorithms shown in Appendix C.1, especially if such a symmetrization involves very different h_i values for the particle pair. Indeed, the Friedrichs–Courant–Lewy condition, calculating the evolutionary explicit time-step (Courant et al., 1928; Monaghan, 1992), takes into account the effective h_i values, not of those symmetrized values occurring in binary interaction among pairs of particles which are instead working in the conservation equations. This implies that the used Friedrichs–Courant–Lewy condition is no more strictly linked to the working equations.

The second difficulty deals with the errors in the interpolation-integration process coming out from the spatial distribution of neighbours (Vaughan et al., 2008; Vaughan, 2009; Zhu et al., 2015) as well as on h_i. Any radial expansion of h_i, either at the boundary or close to a densely populated local region of space, leads to a population of companions strongly anisotropic and uneven. It is true that if a refinement of SPH-ASPH through a particle splitting approach can reduce that component of error at the cost of introducing other errors in the energy and momentum of daughter particles (Meglicki et al., 1993; Børve et al., 2001, 2005; Lastiwka et al., 2005; Feldman and Bonet, 2007; Reyes López et al., 2013; Barcarolo et al., 2014; Spreng et al., 2014; Khorasanizade and Sousa, 2016; Vacondio et al., 2013, 2016; Liu et al., 2018; Wang et al., 2019). However, this trick cannot be unlimited, increasing dramatically the number of particles beyond the actual practical limits of computing, cumulating such errors whenever a general refinement is performed. Moreover, since the newly-formed daughter particles are created in positions too close to the mother particles, the unpleasant particle pair instability in the pressure forces arises in such circumstances, if the particle mutual radial distance is much smaller than h_i.

These two difficulties highlight the fact that gradients of particle density lead to worse interpolations, as long as such compact support Kernels are used. The adoption of a constant smoothing length often does make the problem worse. This is due to the inadequacy of the assigned spatial resolution length for high compression problems as well as to the lack of accuracy for high rarefaction problems. But in a few cases it is the opposite. Indeed, in this paper, it is shown at least one low compressibility accretion disc model in an LMCB (Section 3.1), where compact profile Kernels develop a minimal disc structure with less neighbours in no adaptive conditions, while adaptive disc models with more neighbours do not. Instead, things are the opposite in high compressibility accretion disc modelling, with the exception of disc thickness. Any speculation about the improvement of results for adaptive models based on many more neighbours is out of place in this case. The number of neighbours involving the accuracy of the integration-interpolation, together with the set of related problems, determines the result also on the basis of the physical characteristics and boundary conditions. In some circumstances results could improve, but in other cases they could be worse.

Appendix D. Turbulent physical viscosity in terms of collective molecular interactions

Physical dissipation in the Navier–Stokes fluid dynamics is a mechanism for the momentum-transfer and the conversion of mechanical energy into heat. Molecular interactions on microscopic scale lengths are responsible for such a damping mechanism. In such equations, macroscopic scales are related to the molecular viscosity as the momentum of equations in the τ-relaxation approach (Pitaevskii and Lifshits, 1981). In this approach, the kinematic viscosity coefficient ν_k, calculated on a microscopic basis, is justified at least for laminar flows in the so-called "classical model" scheme where $\nu_k \equiv \nu_{cl} \propto c_s(sn)^{-1}$, being s the scattering cross section and ν_{cl} the kinematic viscosity coefficient.

Whenever the CFD equations deal with turbulent flows, the viscous standard model, adopting the microscopic kinematic viscosity, does not correctly work. Therefore, the kinematic viscosity coefficient cannot be correctly used in the nonlinear Navier–Stokes equations for macroscopic chaotic turbulent viscous flows, because it is necessary to take into account the macroscopic spatial resolution lengths of contiguous moving fluid components.

Thus, a macroscopic viscosity is used in the Navier–Stokes equations as a tensorial viscous dissipation term, relative to mutual interactions among moving contiguous macroscopic flow parts, determining flow braking and fluid heating. A macroscopic turbulent viscosity coefficient is characterized by a macroscopic scale length multiplied by a characteristic velocity in the Von Kármán formulation to describe a repeating pattern of swirling vortices caused by the unsteady separation of flow of a fluid over bluff bodies. As for the spatial component, a mixing length l is often required in the formulation of the macroscopic turbulent viscosity coefficient ν in the viscous stress tensor describing the nonlinear turbulent eddy viscosity. Such a scale length, as it is, is determined in the case of turbulent flows without any reference to the fluid chemical composition and the molecular dimensions. Besides, current analytic formulations of the turbulent dynamic viscosity η always include a direct linear dependence on the mass-density ρ together with other arbitrary parameters, to be set case by case.

D.1. The macroscopic viscosity coefficient: actual approaches

Typical kinematic laboratory viscosities are of the order of $\nu = 10^{-3} - 1\ \mathrm{cm}^2\ \mathrm{s}^{-1}$, to be compared with inertial forces in the ratio expressing the Reynolds number

$$Re = \frac{\text{inertial forces}}{\text{viscous forces}} \equiv \frac{l_{flow}\mathrm{v}_{flow}}{\nu} \tag{D.1}$$

where l_{flow} and v_{flow} are the characteristic length and velocity scales of the flow. Laboratory experiments shows that for $Re > Re_{crit} \approx 10^2$–$10^3$, the flow becomes turbulent. Re_{crit} is the critical Reynolds number, as observed so far, identifying a threshold beyond which the flow is turbulent.

In the full nonlinear approach, the spatial derivatives of the entire velocity field are used and the full Navier–Stokes equations working with spatial gradients of the mean velocity field are considered (as in the nonlinear Boussinesq approach) (Schmitt, 2007). In doing so, any Reynolds average of the Navier–Stokes equations in boxes of intermediate size (as in the linear approach), is excluded.

A nonlinear macroscopic viscosity coefficient ν is usually described by an unknown characteristic length l and by an unknown scale velocity v to be evaluated.

Typically (Prandtl, 1925), a mixing length model can be used, where

$$\mathrm{v} \sim l \left| \frac{\partial \mathrm{v}}{\partial x} \right|, \tag{D.2}$$

$$\nu \sim l^2 \left| \frac{\partial \mathrm{v}}{\partial x} \right|, \tag{D.3}$$

or, more generally, for a better statistical evaluation,

$$\frac{\nu^2}{l^4} \sim \left(\frac{\partial \mathrm{v}_x}{\partial y} + \frac{\partial \mathrm{v}_x}{\partial z} \right)^2 + \left(\frac{\partial \mathrm{v}_y}{\partial x} + \frac{\partial \mathrm{v}_y}{\partial z} \right)^2 + \left(\frac{\partial \mathrm{v}_z}{\partial x} + \frac{\partial \mathrm{v}_z}{\partial y} \right)^2. \tag{D.4}$$

The problem is in the evaluation of l, being $h \le l \le L$, where h is the computational spatial resolution and L the scale length of the entire computational domain. Without any data on geometric scale lengths, the only physical scale lengths to be used are those relative to the hydrostatic equilibrium (in the presence of an external force field) f: $\int (\rho f)^{-1} dp$, as well as $p|\nabla p|^{-1}$, $\rho|\nabla \rho|^{-1}$, $|\mathbf{v}||\nabla \cdot \mathbf{v}|^{-1}$, $|\mathbf{v}||\nabla \times \mathbf{v}|^{-1}$, $|\nabla \times \mathbf{v}||\nabla \times (\nabla \times \mathbf{v})|^{-1}$.

In 3D, the natural tendency is the development of smaller structures in a direct cascade process (Kolmogorov, 1941a,b). For this reason, some authors (Trampedach and Stein, 2011) calculate for each time-step

$$l = \left(\sum_i l_i^{-1} \right)^{-1}. \tag{D.5}$$

where l_i refers to various scale lengths as $(\partial \ln \rho / \partial r)^{-1}$, $(\partial \ln V / \partial r)^{-1}$, $(\partial \ln p / \partial r)^{-1}$, $(\nabla \cdot \mathbf{v}|\mathbf{v}|^{-1})^{-1}$.

Instead, v is unknown, because macroscopically we only know v_{flow} and c_s.

In the viscous accretion disc modelling, the parametrization of Shakura (1973), Shakura and Sunyaev (1973) of turbulent viscosity is largely adopted. In this approach, the kinematic viscosity coefficient is given by

$$\nu = \frac{1}{3} l \mathrm{v}, \tag{D.6}$$

where both l and v are unknown. Assuming the flow isotropy, a Keplerian tangential kinematics, and the vertical hydrostatic equilibrium,

$$l = \alpha_l H, \tag{D.7}$$

where $H \simeq r c_s \mathrm{v}_{Kepl}^{-1}$ is the local disc thickness, and it is the shortest local macroscopic scale length. $\alpha_l \le 1$ is a scaling quantity. Without any isotropy assumption, $\alpha_l > 1$. At the same time,

$$\mathrm{v} = \alpha_v c_s, \tag{D.8}$$

where $\alpha_v \le 1$. Whenever $\mathrm{v} > c_s$, shocks would dissipate the energy, reducing the velocity to subsonic. Hence, in the Shakura and Sunyaev approach,

$$\nu = \frac{1}{3} \alpha_l \alpha_v c_s H = \alpha_{SS} c_s H, \tag{D.9}$$

with $\alpha_{SS} < 1$ to be found.

An $10^{-2} \le \alpha_{SS} \le 3\ 10^{-2}$ was found as a lower limit for active galactic nuclei (AGN) for a luminosity $\mathcal{L} \le \mathcal{L}_E$, in the ratio $10^{-1} \le \mathcal{L}/\mathcal{L}_E \le 1$, where $\mathcal{L}_E$ is the Eddington luminosity (Pringle, 1981). However, for numerical simulations of AGN, $\alpha_{SS} \approx 10^{-4}$–$10^{-3}$ is often also adopted (Lanzafame et al., 1998, 2008). Values for $\alpha_{SS} \approx 10^{-2}$ have also been found for the observed protostellar objects (Hartmann et al., 1988), while $\alpha_{SS} \approx 10^{-3}$–$3\ 10^{-3}$ for a fit of FU Orionis observed outbursts (Clarke et al., 1990; Bell and Lin, 1994; Lodato and Clarke, 2004). In fully ionized discs in dwarf novae, the best-observed evidence suggests a typical $\alpha_{SS} \sim 10^{-1}$–$4\ 10^{-1}$, whilst the many numerical MHD simulations evaluate $\alpha_{SS} \approx$ 10-times smaller. This discrepancy is attributed to shortcomings due to incorrect evaluations of magnetic and boundary layer conditions in the computations (King et al., 2007). Nevertheless, this does not solve the problem because a bound viscous accretion disc structure modelling strongly depends on several conditions: the kinematic of the mass-transfer, γ, α_{SS} and so on (Lanzafame, 2008, 2009). For isothermal or for quasi-isothermal thermodynamics, a disc is structurally gravitationally bound even for $\alpha_{SS} = 0$ because even the numerical dissipation alone is enough to get a disc in shock events (Sawada et al., 1987; Spruit et al., 1987), a result also discussed in its physical sense (Lanzafame, 2010b).

D.2. The macroscopic viscosity coefficient ν as collective molecular damping

Each of the above-mentioned formulations for macroscopic physical dissipation applies to specific problems and rarely converges with each other. It often includes at least one arbitrary parameter, to be tuned case by case. The nature of such formulations is mathematical since any correlation to microscopic molecular, atomic, or nuclear physical properties is excluded.

In order to determine the viscous stress tensor $\boldsymbol{\tau}$ in the Navier–Stokes equations (Eqs. ((A.1)–(A.5))), an evaluation of the macroscopic viscosity coefficient ν can be made on a physical basis. This is possible whenever the macroscopic characteristic evolutionary time is much longer than the microscopic characteristic time of molecular collisions. In such conditions, the collective collisional action of molecules on macroscopic spatial and time scales can be significant (Lanzafame, 2015).

Microscopic molecules, atoms and nuclei have known experimental or theoretical impact cross sections s, useful to compute ν. Free of any consideration of the involvement of internal energy levels, physical dissipation transfers macroscopic kinetic energy flows into heat, which means the conversion of ordered macroscopic kinetic energy in microscopic Brownian motions. So that the elastic scattering collisional cross sections for an ideal gas are right for a reformulation of ν. For a gas mixture, the mean value of the elastic scattering impact cross-section

$$\overline{s} = \sum_i X_i s_i \tag{D.10}$$

should be considered, where $X_i = n_i (\sum_i n_i)^{-1}$ is the relative numerical abundance of the ith chemical species.

However, it is necessary to take into account the combined action of the union of the total number of microscopic molecules-atoms within the macroscopic cross section determined by the mixing length. A mixing length l, as expressed by Eq. (D.5), unfortunately arithmetically gives an extraneous value, because smaller than the smallest scale length in the summation. For this reason, it should be better the calculation of l for each time-step as

$$l = \min(l_1, l_2, l_3, \ldots, l_n), \tag{D.11}$$

whenever local flow inhomogeneities and/or anisotropies occur, the various l_i referring to $p|\nabla p|^{-1}$, $\rho|\nabla \rho|^{-1}$, $|\mathbf{v}||\nabla \cdot \mathbf{v}|^{-1}$, $|\mathbf{v}||\nabla \times \mathbf{v}|^{-1}$, $|\nabla \times \mathbf{v}|$ $|\nabla \times (\nabla \times \mathbf{v})|^{-1}$. From the physical point of view, l is thus determined in absolute fashion, only from known macroscopic flow physical parameters. Instead, from the numerical point of view, an indirect correlation exists to the local spatial resolution length h, since it quantitatively affects the spatial derivatives.

The total number of microscopic particles contained within the 3D mixing mass ρl^3 is $\rho l^3 \overline{\mu}^{-1} \mathcal{N}_{\mathcal{A}}$.

On a statistical basis, the spatial mixing length l in the expression for ν can be replaced with $S\lambda^{-1}$, that is the effective braking surface

divided by a length on a molecular scale. It is worth noting that the effective surface S represents the union of the molecular cross-sections within the mixing mass ρl^3. So, the mixing length l is split in the union of a collection of molecular components. Thus, in 3D it is necessary to compute $(\rho l^3 \overline{\mu}^{-1}\mathcal{N}_{\mathcal{A}})^{\frac{2}{3}}$, that is the number of molecules within the volume l^3, powered to 2/3. This term statistically corresponds to the effective number of microscopic molecules within the mixing mass ρl^3, as externally counted by an observer. This number has to be multiplied by $\overline{s}$ to get a statistically effective collisional surface composed of a multitude of microscopic cross sections:

$$S = (\overline{\mu}^{-1}\mathcal{N}_{\mathcal{A}}\rho l^3)^{\frac{2}{3}}\overline{s}. \tag{D.12}$$

In order to calculate ν, we need to divide this arithmetic term by a length λ decreasing whenever the local number density $n = \overline{\mu}^{-1}\mathcal{N}_{\mathcal{A}}\rho$ increases. Therefore $\lambda \sim n^{-\frac{1}{3}}$.

The logic of this description foresees that Eq. (D.12) represents the effective impact surface of a random distribution of molecules within the l size box whilst the mean molecular cross-section is $\overline{s}$. Fluids are not continuous on a microscopic scale, but they are a chaotic distribution of microscopic atoms, and molecules, so that the collisional effective surface of the moving $l \times l$ box is not l^2, but that calculated by Eq. (D.12).

Alternatively, this conclusion can also be explained as follows. On the geometric $l \times l$ surface, the effective number density of the fluid in purely statistical terms is $n^{2/3}$. Then, $n^{2/3}l^2$ is statistically the effective number of molecules on this surface. Hence, the effective collisional (braking) surface is obtained as $n^{2/3}l^2\overline{s}$, that is exactly Eq. (D.12), as long as s_i in Eq. (D.10) are elastic collisional cross sections, since the gas is ideal.

As far as the velocity contribution for ν is concerned, any dependence either on v_{flow} or on $\epsilon^{1/2}$ are inadequate. Kinematic velocities of extraneous bodies moving in the fluid, as in the original Von Kármán formulation, are not considered, as well as chemically different flows in unmixed fluids. In doing so, v_{flow} is excluded. Instead, $\epsilon^{1/2}$ does not take into account the ratio of specific heats γ, affecting the speed of signals. Therefore, its exclusion is a consequence of the fact that the macroscopic viscosity coefficient, the thermal conductivity, and the diffusivity coefficients – all mutually correlated – are expressions of the intrinsic physical property of the fluid. So, the sound velocity c_s remains the best compromise as regards the velocity component for the macroscopic viscosity coefficient, representing not only the characteristic velocity of signal propagation but also a reference velocity affecting the heat conductivity speed. Thus, to conclude, the macroscopic kinematic viscosity coefficient ν is

$$\nu \simeq \mathcal{M}\varsigma = \mathcal{M}(\overline{\mu}^{-1}\mathcal{N}_{\mathcal{A}}\rho l^3)^{\frac{2}{3}}\overline{s}n^{\frac{1}{3}}c_s = \mathcal{M}\overline{\mu}^{-1}\mathcal{N}_{\mathcal{A}}\rho l^2\overline{s}c_s, \tag{D.13}$$

whose 2D counterpart, according to the same algebraic logical steps is:

$$\nu \simeq \mathcal{M}\varsigma = \mathcal{M}(\overline{\mu}^{-1}\mathcal{N}_{\mathcal{A}}\Sigma l^2)^{\frac{1}{2}}\overline{s}n^{\frac{1}{3}}c_s = \mathcal{M}\overline{\mu}^{-1}\mathcal{N}_{\mathcal{A}}\Sigma l\overline{s}c_s. \tag{D.14}$$

Both formulations provide the first and the second dynamic macroscopic viscosity coefficients η and ζ reported in Eq. (A.14). $\Sigma = (\rho^2\overline{\mu}\mathcal{N}_{\mathcal{A}}^{-1})^{1/3}$ is the 2D mass density and $\mathcal{M}$ is a parameter to be tuned only once for both the shear and the bulk viscosities, assigning $\mathcal{M}\overline{\mu}^{-1}\mathcal{N}_{\mathcal{A}}\rho\overline{s}r_\circ \sim 10^{-2} \div 1$ or $\mathcal{M}\overline{\mu}^{-1}\mathcal{N}_{\mathcal{A}}\Sigma\overline{s} \sim 10^{-2} \div 1$ in dimensionless units, respectively, where $r_\circ \sim L$ is the reference length. Whenever the flow is homogeneous and isotropic, no macroscopic viscosity is locally activated without any relative motion among contiguous flow portions.

In these expressions, both the molecular/atomic $\overline{\mu}\mathcal{N}_{\mathcal{A}}^{-1}$ and $\overline{s}$ are included, as well as other macroscopic physical quantities like c_s, l, Σ or ρ for each time-step. For this reason, these two formulations show hybrid characters. $\nu \propto \varsigma$ refers to a macroscopic viscosity coefficient, different to the microscopic kinematic viscosity coefficient because $\varsigma \propto \overline{s}n$, instead of being $\propto (\overline{s}n)^{-1}$.

In Eqs. ((D.13) and (D.14)) $\mathcal{M}\rho\overline{\mu}^{-1}\mathcal{N}_{\mathcal{A}}l\overline{s}$ and $\mathcal{M}\Sigma\overline{\mu}^{-1}\mathcal{N}_{\mathcal{A}}\overline{s}$ are pure numbers both < 1, otherwise the density of the fluid would be comparable to or greater than the atomic density. This means that, although depending on geometric and intrinsic thermodynamic factors, like formulations (Eqs. (D.13) and (D.14)), $\nu = \mathcal{M}\varsigma$ cannot have an exact quantitative comparison concerning the other two simpler and conceptual expressions: $\nu = c_s h$ and $\nu = c_s l$.

In the classical model approach, where $\nu_k \equiv \nu_{cl} \propto c_s/(\overline{s}n)$, the microscopic kinematic viscosity coefficient is proportional to the molecular mean-free-path, so that $\nu_k \propto \lambda$. Hence, the viscosity pays attention to the molecular diffusion on microscopic scales, conserving kinetic energy and momentum components through elastic collisions, converting ordered macroscopic momenta into heat, that is into microscopic chaotic momenta. Instead, as far as the hybrid macroscopic $\nu = \mathcal{M}\varsigma$ is concerned, especially in its formulation (Eq. (D.13)), being $\varsigma \propto \lambda^{-1}$, it pays attention to the frequency of collision. So that in Eq. (D.13), $\varsigma \propto l\lambda^{-1}c_s$ deals with the rate of collective collisions within the macroscopic mixing scale length l. The background of the two viscosities is, thus, conceptually very different, and it is impossible to give relevance either to the rate of collisions or to the microscopic mean-free-path λ in formulations where both dependencies are simultaneously taken into account.

It is noteworthy that Eqs. ((D.13) and (D.14)) are not exactly equivalent. In Eq. (D.13) $\nu \propto l^2$ in its spatial dependence, as Prandtl's Eqs. ((D.3) and (D.4)). In Eq. (D.14) $\nu \propto l$ in the same spatial contribution, as Shakura and Sunyaev's Eq. (D.9). Eqs. ((D.13) and (D.14)) should be considered strictly correlated either to a 3D or to a 2D modelling. Indeed, densities ρ and Σ are formally correlated by the equivalence of their number densities as $(\Sigma\overline{\mu}^{-1}\mathcal{N}_{\mathcal{A}})^3 = (\rho\overline{\mu}^{-1}\mathcal{N}_{\mathcal{A}})^2$. So that $\Sigma \equiv \rho l$ would correspond to a very specific case.

In 3D modelling the choice of l as the smallest macroscopic fluid scale length in Eq. (D.11) is due to the development of smaller structures in a direct cascade process (Kolmogorov, 1941a,b), without any drift towards molecular scales, where the flow structure changes from fluid to Brownian chaotic molecules. This argument seems strictly no longer valid in 2D, where larger structures develop in an inverse cascade process (Kraichnan, 1967, 1971). Instead, even in a strictly 2D modelling, relations like Eqs. ((D.5) or (D.11)) still holds because

- numerical results for a strictly 2D modelling need to converge with those for a 3D flow modelling of flat flow structures where the 3rd dimension is not used. In Magnetohydrodynamics (MHD), the 2D limit could be singular. 2D+1/2 MHD turbulence is expected to display very different features from 2D MHD turbulence (Montgomery and Turner, 1981). Free of any magnetic field presence any 2D – 2D and a half – MHD solution discrepancy does not have to concern us even in a purely fluid dynamic approach;
- in 2D, in the limit of a static flow, $l \to \infty$ and the flow becomes too viscous according to expressions where smaller spatial derivatives involve larger mixing lengths like Eqs. ((D.5) or (D.11));
- l is mathematically computed through Eq. (D.11), even in 2D. The physical increase of l in 2D turbulence is a consequence of the inverse cascade kinematics, not the cause, despite l being macroscopically chosen according to the same criteria. The growing-up of larger structures in 2D increases the values of all the characteristic lengths included in the expressions (either Eq. (D.5) or Eq. (D.11)).

D.3. The physical origin of ς: comparison with the classical kinematic viscosity coefficient ν_{cl}

In the Navier–Stokes momentum and energy equations (Eqs. (A.2) and (A.3)), the viscous stress tensor τ takes into account the shear and the bulk transfer of momentum and the viscous heating among contiguous fluid components, through the 1st and the 2nd dynamic viscosity coefficients η and ζ. The shear dynamic viscosity coefficient

$\eta = \rho\nu_{shear} = \rho\mathcal{M}_1\varsigma$, whilst the dynamic bulk viscosity coefficient is $\zeta = \rho\nu_{bulk} = \rho\mathcal{M}_2\varsigma$, where $\mathcal{M}_1$ and $\mathcal{M}_2$ not necessarily equals with each other. In the Newtonian approach $\tau_{\alpha,\beta}$ is expressed as it is shown in Eqs. ((A.14) and (A.15)).

As far as the microscopic kinematic viscosity coefficient ν_k is concerned, we can write that

$$\tau_{\alpha,\beta} = S^{-1}\frac{\partial q_\alpha}{\partial t}\frac{\partial r}{\partial x_\beta} \simeq S^{-1}\frac{\partial m}{\partial t}\overline{\mathrm{v}}_\alpha\frac{\partial r}{\partial x_\beta}, \tag{D.15}$$

where the shear stress equals the rate of momentum variation $\mathbf{q}$ per unit area at the contact surface S between two contiguous fluid components, being the direction β of their relative motion perpendicular to S.

In this relation, $\overline{\mathrm{v}}$ is the mean molecular collisional velocity, whose spatial component α is:

$$\overline{\mathrm{v}}_\alpha = \frac{1}{2}\lambda\frac{\partial \mathrm{v}_\alpha}{\partial x_\beta}\frac{\partial x_\beta}{\partial r}, \tag{D.16}$$

being λ the molecular mean-free-path. In a not collisional approach, the rate of mass change equals the mass flow through S:

$$\frac{\partial m}{\partial t} \simeq \rho c_s S. \tag{D.17}$$

Thus, from Eqs. ((D.15), (D.16) and (D.17)),

$$\tau_{\alpha,\beta} \simeq \frac{1}{2}\rho\lambda c_s\frac{\partial \mathrm{v}_\alpha}{\partial x_\beta}, \tag{D.18}$$

therefore, in this approach the role of collisions is based only on $\overline{\mathrm{v}}$, both in ν_k and in $\boldsymbol{\tau}$ (that means η and ζ through Eq. (A.14)) which are all $\propto \lambda$.

As for the macroscopic hybrid viscosity coefficient ς, in 3D we associate the rate of mass collisions $\partial m/\partial t$ on the contact surface S, to the contextual rate of molecular elastic collisions, involving the conservation of kinetic energy and momentum components along the macroscopic scale length l. For this reason,

$$\frac{\partial m}{\partial t} \simeq \rho c_s\lambda^{-1} lS \tag{D.19}$$

instead of Eq. (D.17). In this expression, $c_s\lambda^{-1}$ is the molecular collisional frequency, whilst lS is the volume of adjacent flow elements, whose mass is ρlS. In doing so, the rate of mass variation $\partial m/\partial t$ is strictly related to the rate of mass collisions from the contact surface S. At the same time, macroscopically, as far as the mean flow velocity is concerned,

$$\overline{\mathrm{v}}_\alpha \simeq l\frac{\partial \mathrm{v}_\alpha}{\partial x_\beta}\frac{\partial x_\beta}{\partial r}. \tag{D.20}$$

Therefore, from Eqs. ((D.15), (D.19) and (D.20)),

$$\tau_{\alpha,\beta} = c_s\lambda^{-1}\rho l^2\frac{\partial \mathrm{v}_\alpha}{\partial x_\beta}, \tag{D.21}$$

thus, in this approach, $\boldsymbol{\tau}$ and ς are both $\propto \lambda^{-1}$.

Being the expression (D.20) too direct, as far as the macroscopic flow mean velocity component is concerned, the theoretical rationale for $\nu = \varsigma$ mainly deals with the expression (D.19), leading to Eq. (D.21). In this regard, since $\varsigma \sim \nu_k(l\lambda^{-1})^2$, formulation (D.13) compares to that relative to the microscopic kinematic viscosity coefficient ν_k whenever $l \sim \lambda$, while Eq. (D.20) compares to Eq. (D.16) in an extreme non-fluid condition where the fluid dynamics reduces to a molecular kinematics. This is determinant to understand the physical meaning of $\nu \propto \varsigma$ as tightly linked to that of $\nu \propto \nu_k$. In the same fashion, Eq. (D.21) equals its kinematic viscosity counterpart when $l = \lambda$.

In so far as $l\nu^{-1} \gg \lambda c_s^{-1}$, a macroscopic time-lapse is longer than the characteristic microscopic collisional times, In these conditions, it is possible to assume the mixing length l as a collection of molecular mean-free-paths during, as:

$$l = \sum_{i=1}^{N}\lambda_i = N\overline{\lambda}, \tag{D.22}$$

being N an integer number, corresponding to the total number of averaged mean-free-paths to which l is splitted and being $\overline{\lambda} = N^{-1}\sum_{i=1}^{N}\lambda_i$.

$\lambda_i n_i^{1/3}$ is the number of molecules in a row within the spatial range $[\lambda_i, \lambda_{i+1}]$. In doing so, Eq. (D.19) becomes:

$$\frac{\partial m}{\partial t} \simeq \rho S c_s N, \tag{D.23}$$

while Eq. (D.21) becomes:

$$\tau_{\alpha,\beta} = c_s\overline{\lambda}^{-1}\rho l^2\frac{\partial \mathrm{v}_\alpha}{\partial x_\beta} = \rho N^2\nu_k\frac{\partial \mathrm{v}_\alpha}{\partial x_\beta}. \tag{D.24}$$

So that, through the flow mass within the volume $N\overline{\lambda}S$, the term $\rho N\overline{\lambda}S$ determines the rate of mass collisions, whilst the term $N^2\nu_k$ characterizes the viscosity stress tensor.

Being the entire spatial characteristic length l geometrically involved in the computation of $\nu = \mathcal{M}\varsigma$, the macroscopic damping process affects all N short components whose l is made of. Of course, microscopic molecular kinematics exists within l. However, since we only deal with macroscopic velocity fields, any molecular Brownian motion is not taken into account. Hence, despite the mean-free-path concept involving microscopic molecular motions, we need to shift the same statistics on a larger scale length. So that only one macroscopic collision occurs for a group of molecules in a row, ideally forming a parcel, covering the microscopic mean-free-path λ. A statistical group of $\lambda n^{1/3}$ molecules determines a parcel. In this view, it is as if one collision of a macroscopic body involves the contextual microscopic collisions of all its exposed molecular components. Each of the N macroscopic molecular parcels (MMP) statistically covers N mean-free-paths, in the mixing of macroscopic and microscopic views. Thus, N arrays of macroscopic molecular parcels (MMPs), within l, give N macroscopic collisions for each, in turn consisting of $\lambda n^{1/3}$ microscopic molecular collisions.

For simplicity, let us assume that $\lambda_i = \overline{\lambda}_i = \overline{\lambda}$, which means that l is split in equal mean-free-paths in a row and that $l = \overline{\lambda}_1 + \overline{\lambda}_2 = 2\overline{\lambda}$. Those molecules within the first MMP $[0, \overline{\lambda}_1]$ in a row along l, covering the full path $\sim\overline{\lambda}$, statistically collectively collide once at the sound velocity c_s when crossing the surface S. This means two collisions altogether, also considering the statistical collective collision of the second group of molecules within $[\overline{\lambda}_1, \overline{\lambda}_1+\overline{\lambda}_2]$ in a row along l. Then, two more collisions occur as soon as the second MMP in a row along l crosses the same surface S. That statistically means four macroscopic collisions at all.

Similarly, if $l = \overline{\lambda}_1 + \overline{\lambda}_2 + \overline{\lambda}_3 = 3\overline{\lambda}$ in a row along l, MMP within $[0, \overline{\lambda}_1]$, $[\overline{\lambda}_1, \overline{\lambda}_1+\overline{\lambda}_2]$ and $[\overline{\lambda}_1+\overline{\lambda}_2, \overline{\lambda}_1+\overline{\lambda}_2+\overline{\lambda}_3]$ in a row along l statistically collectively collide three times for each group. This statistically means nine macroscopic collisions at all, when all molecules in a row along l cross the surface S at the sound speed, and so on.

For $i = 1, 2, \ldots, N$, all $\overline{\lambda}_i n_i^{1/3}$ molecules within the ith MMP $[\sum_{j=1}^{i}\overline{\lambda}_j, \sum_{j=1}^{i+1}\overline{\lambda}_j]$, located in a row along l, statistically perform i macroscopic collisions when in turn entirely crossing the surface S, because the path covered by the ith MMP is $\sim\sum_{j=1}^{i}\overline{\lambda}_j \simeq i\overline{\lambda}$. Therefore, notating for simplicity $\lambda = \overline{\lambda}$, the essence of $l^2\lambda^{-1}$ in Eq. (D.21), coupling the mass variation rate to the macroscopic mean velocity field justifies the $\nu = \mathcal{M}\varsigma$ formulation also showing how it is linked to ν_k, because a rate of collision $\propto l^2\lambda^{-1}$ means that,

$$\varsigma \simeq \frac{l^2}{\overline{\lambda}^2}\nu_k = N^2\nu_k = N\sum_{i=1}^{N}\nu_{k,i}, \tag{D.25}$$

where $\nu_{k,i} \simeq \lambda_i c_s$ is the microscopic kinematic viscosity coefficient relative to the ith mean-free-path. N^2 is the total number of collisions of N averaged mean-free-paths crossing S and collectively located in a row along l, coming from both the rate of mass collision and the macroscopic mean velocity field formulations. These conclusions hold even considering the more complicated splitting of l in different mean-free-paths $l = \sum_{i=1}^{N}\lambda_i$, without any reference to their average $\overline{\lambda}$, because it is noteworthy that algebraically $N\nu_k = \sum_{i=1}^{N}\nu_{k,i}$.

Hence, apart the statistical computation of $\nu = \mathcal{M}\varsigma$ shown in Appendix D.2, this approach shows that a similarity exists between ς and ν_k, despite $\nu = \mathcal{M}\varsigma$ deals with macroscopic flows. This shows that any theoretical motivation for $\nu = \mathcal{M}\varsigma$ deals with that relative to ν_k and further explains the hybrid nature of ς.

It is also noteworthy that in a purely non collisional macroscopic approach, Eqs. ((D.17) and (D.20)) lead to a simple expression where

$$\tau_{\alpha,\beta} = \rho c_s l \frac{\partial \mathrm{v}_\alpha}{\partial x_\beta}, \tag{D.26}$$

thus the macroscopic kinematic viscosity coefficient $\nu = c_s l$.

Similarly, considering

$$\frac{\partial m}{\partial t} \simeq \rho l \left| \frac{\partial \mathrm{v}}{\partial x} \right| S, \tag{D.27}$$

together with Eqs. ((D.19) and (D.20)), give the Prandtl formulation (Eq. (D.3)). This inevitably shows that any reasonable physical formulation leads to equations that are physically very different where either a direct dependence on λ, l, $l^2\nabla$ or $l^2\lambda^{-1}$ are possible.

D.4. Macroscopic viscosity and thermal conductivity coefficient for dilute gases

The macroscopic viscosity coefficient ν and the thermal conductivity coefficient c are dimensionally identical. Both are characterized by a scale length multiplied by a scale speed. Thus, both coefficients deal with transport mechanisms. The viscosity is activated only whenever relative motions occur among contiguous flow elements. Instead, thermal conductivity is an always-existing energy transport mechanism whenever a temperature gradient occurs even in static macroscopic conditions. However, the two coefficients are always related to each other because both explain the tendency of thermodynamic systems towards the homogeneity and isotropy status, smoothing out kinematic (ν) and thermal (c) local spatial discrepancies. The ratio of coefficients $c\nu^{-1}$ is (Reif, 1965):

$$\frac{c}{\nu} = \frac{c_V}{\epsilon \overline{\mu}}, \tag{D.28}$$

where c_V is the molar specific heat of the gas at a constant volume which, for an ideal (monoatomic) gas is $c_V = 3\mathcal{R}T/2 = 3\mathcal{N}_A\mathcal{K}_B T/2$, where $\mathcal{R}$ is the perfect gases constant. Experimentally $c\nu^{-1}\epsilon\overline{\mu}c_V^{-1} \approx 1.3-2.5$, instead of 1. The discrepancy is largely explained by the fact that theoretically c is evaluated considering a uniform molecular velocity distribution instead of local molecular kinematic differences related to the presence of a temperature spatial gradient. As a consequence, considering $\nu = \mathcal{M}\varsigma$, for an ideal gas,

$$c = 2\nu \frac{c_V}{\epsilon\overline{\mu}} \simeq 2\mathcal{M}\varsigma \frac{c_V}{\epsilon\overline{\mu}} = 3\mathcal{M}\varsigma \frac{\mathcal{N}_A\mathcal{K}_B T}{\epsilon\overline{\mu}} \tag{D.29}$$

so that,

$$c \simeq 2\mathcal{M}\left(\frac{l}{\overline{\mu}}\right)^2 \rho c_s \overline{s} \mathcal{N}_A \frac{c_V}{\epsilon} = 3\mathcal{M}\frac{\rho c_s \overline{s}\mathcal{K}_B T}{\epsilon}\left(\frac{l\mathcal{N}_A}{\overline{\mu}}\right)^2 \tag{D.30}$$

in 3D, and

$$c \simeq 2\mathcal{M}\left(\frac{1}{\overline{\mu}}\right)^2 \Sigma l c_s \overline{s} \mathcal{N}_A \frac{c_V}{\epsilon} = 3\mathcal{M}\frac{\Sigma l \overline{s} c_s \mathcal{K}_B T}{\epsilon}\left(\frac{\mathcal{N}_A}{\overline{\mu}}\right)^2 \tag{D.31}$$

in 2D. Since coefficients ν and c are comparable for dilute gases, then the time-scales of the viscous and thermal conductivities are also comparable. This means that the inertia of matter tends towards a uniform kinematic and thermal configuration within the same time-scales.

In the viscous computational fluid dynamics, currently ν and c (c_{ij} in Eq. (A.11)) are not only arbitrarily parametrized, but they are also unrelated to each other. In spite of the fact that results could still be significant in isothermal or in nearly isothermal conditions, the lack of any correlation between ν and c is free of any physical meaning, especially for diffusive fluid dynamics.

In this paper, we mainly pay attention to macroscopic viscosity. However, from now onwards, any conclusion referring to the role of the macroscopic viscosity will also refer to the thermal conductivity in a close cause–effect correlation. In doing so, any significant local spatial derivative, involving a relative motion among contiguous flow parts, will involve braking and viscous heating. Any local heating will involve higher pressure and temperature spatial gradients and consequently a transport of energy and mass within comparable time-scales. Any heat-transfer will involve variations in temperature and pressure spatial gradients.

References

Amicarelli, A., Marongiu, J.C., Leboeuf, F., Leduc, J., Caro, J., 2011a. C & F 44 (279).
Amicarelli, A., Marongiu, J.C., Leboeuf, F., Leduc, J., Neuhauser, M., Fang, L., Caro, J., 2011b. Int. J. Numer. Meth. Eng. 87 (677).
Balsara, D.S., 1995. JCoPh 121 (357).
Barcarolo, D.A., Touzé, D.Le., Oger, G., de Vuyst, F., 2014. JCoPh 273 (640).
Bell, K.R., Lin, D.N.C., 1994. Astrophys. J. 427 (987).
Benz, W., Bowers, R.L., Cameron, A.G.W., Press, W.H., 1990. Astrophys. J. 348 (647).
Bisikalo, D.V., Boyarchuk, A.A., Kutzetsov, O.A., Chechetkin, V.M., 2000. ARep 44 (26).
Bonet, J., Lock, T.-S.L., 1999. Comput. Meth. Appl. Mech. Eng. 180 (97).
Boris, J.P., Book, D.L., 1973. JCoPh 11 (38).
Børve, S., Omang, M., Trulsen, J., 2001. Astrophys. J. 562 (81).
Børve, S., Omang, M., Trulsen, J., 2005. JCoPh 208 (345).
Boyarchuk, A.A., Bisikalo, D.V., Kutzetsov, O.A., Chechetkin, V.M., 2002. Mass transfer in close binary stars. In: Advances in Astronomy and Astrophysics, Vol. 6. Taylor & Francis, London.
Busegnies, Y., François, J., Paulus, G., 2007. Sh. Wav. 16 (359).
Cabezón, R.M., García-Senz, D., Figueira, J., 2017. Astron. Astrophys. 606 (1).
Cabezón, R.M., García-Senz, D., Relaño, A., 2008. JCoPh 227 (8523).
Cabezón, R.M., Pan, K.-C., Lieberdörfer, M., Kuroda, T., Ebinger, K., Heinimann, A., Thielemann, F.-K., 2018. Astron. Astrophys. 619 (1).
Casares, J., Jonker, P.G., Israelian, G., 2017. X-ray binaries. In: Handbook of Supernovae. Springer, Berlin, pp. 1499–1526.
Cha, S.-H., Whitworth, A.P., 2003. Mon. Not. R. Astron. Soc. 340 (73).
Cha, S.-H., Wood, M.A., 2016. Mon. Not. R. Astron. Soc. 458 (480).
Chen, J.K., Beraun, J.E., 2000. Comput. Meth. Appl. Mech. Eng. 190 (225).
Chen, J.K., Beraun, J.E., Carney, T.C., 1999a. Int. J. Numer. Meth. Eng. 46 (231).
Chen, J.K., Beraun, J.E., Jih, C.J., 1999b. Comp. Mech. 23 (279).
Chen, J.K., Beraun, J.E., Jih, C.J., 1999c. Comp. Mech. 24 (273).
Chen, J.K., Beraun, J.E., Jih, C.J., 2001. Comp. Mech. 27 (177).
Churazov, E., Gilfanov, M., Revnivtsev, M., 2001. Mon. Not. R. Astron. Soc. 321 (759).
Clarke, C.J., Lin, D.L.C., Pringle, J.E., 1990. Mon. Not. R. Astron. Soc. 242 (439).
Courant, R., Friedrichs, K., Lewy, H., 1928. Math. Ann. 100 (32).
Cullen, L., Dehnen, W., 2010. Mon. Not. R. Astron. Soc. 408 (669).
Dehnen, W., Aly, H., 2012. Mon. Not. R. Astron. Soc. 425 (1068).
Deng, H., Mayer, L., Meru, F., 2017. ApJ 847 (43).
Di Lisio, R., Greiner, E., Pulvirenti, M., 1998. Comput. Math. Appl. 35 (95).
Díaz Trigo, M., Parmar, A.N., Boirin, L., Méndez, M., Kaastra, J.S., 2006. Astron. Astrophys. 445 (179).
Dilts, G.A., 1999. Int. J. Numer. Meth. Eng. 44 (1115).
Evrard, A.E., 1988. Mon. Not. R. Astron. Soc. 235 (1911).
Fatehi, R., Manzari, M.T., 2011. CaMwA 61 (482).
Feldman, J., Bonet, J., 2007. Int. J. Numer. Meth. Eng. 72 (295).
Flebbe, O., Münzel, S., Herold, H., Riffert, H., Ruder, H., 1994a. Astrophys. J. 431 (754).
Flebbe, O., Münzel, S., Riffert, H., Herold, H., 1994b. MmSAI 65 (1049).
Fletcher, C.A.J., 1998. Computational Techniques for Fluid Dynamics. Springer, Berlin.
Fortin, P., Athanassoula, E., Lambert, J.-C., 2011. Astron. Astrophys. 531 (1).
Frank, J., King, A., Raine, D., 2002. Accretion Power in Astrophysics. Cambridge, UK.
Frontiere, N., Raskin, C.D., Owen, J.M., 2017. JCoPh 332 (160).
Fulbright, M.S., Benz, W., Davies, M.B., 1995. Astrophys. J. 440 (254).
Fulk, D.A., Quinn, D.W., 1996. JCoPh 126 (165).
Gabbasov, R., Sigalotti, G., Cruz, F., Klapp, J., Ramíred-Velazquez, J.M., 2017. Astrophys. J. 835 (287).
Galis, R., 2007. MmSAI 78 (400).
Gibbs, J.W., 1898. Nature 59, 200.
Gibbs, J.W., 1899. Nature 59, 606.
Gingold, R.A., Monaghan, J.J., 1977. Mon. Not. R. Astron. Soc. 181 (375).
Gingold, R.A., Monaghan, J.J., 1978. Mon. Not. R. Astron. Soc. 184 (481).
Gingold, R.A., Monaghan, J.J., 1979a. Mon. Not. R. Astron. Soc. 188 (39).
Gingold, R.A., Monaghan, J.J., 1979b. Mon. Not. R. Astron. Soc. 188 (45).
Gingold, R.A., Monaghan, J.J., 1980. Mon. Not. R. Astron. Soc. 191 (897).
Gingold, R.A., Monaghan, J.J., 1981. Mon. Not. R. Astron. Soc. 197 (461).
Gingold, R.A., Monaghan, J.J., 1982a. Artificial viscosity and the simulation of fragmentation. In: Proceedings of the Astronomical Society of Australia - Proc. ASA. Vol. 4. University Press - Astronomical Society of Australia, Cambridge, pp. 378–379.

Gingold, R.A., Monaghan, J.J., 1982b. JCoPh 46 (429).
Gingold, R.A., Monaghan, J.J., 1983. Mon. Not. R. Astron. Soc. 204 (715).
Gottlieb, J.J., Groth, C.P.T., 1988. JCoPh 78 (437).
Hartmann, L., Calvet, N., Gullbring, E., D'Alessio, P., 1988. Astrophys. J. 495 (385).
Hayasaki, K., Okazaki, A.T., 2004. Mon. Not. R. Astron. Soc. 350 (971).
Herant, M., 1994. MmSAI 65 (1013).
Hernquist, L., Katz, N., 1989. ApJSS 70 (419).
Hirsch, C., 1997. Numerical Computation of Internal and External Flows. Wiley, New York.
Hongbin, J., Xin, D., 2005. JCoPh 202 (699).
Hopkins, P.F., 2013. Mon. Not. R. Astron. Soc. 428 (2840).
Hu, C., Naab, T., Walch, S., Moster, B.P., 2014. Mon. Not. R. Astron. Soc. 443 (173).
Hu, W., Pan, W., Rakhsha, M., Tian, Q., Hu, H., Negrut, D., 2017. Comput. Methods Appl. Mech. Eng. 324 (278).
Ichikawa, S., Osaki, Y., 1992. PASJ 44 (15).
Ichikawa, S., Osaki, Y., 1994. PASJ 46 (621).
Imaeda, Y., Inutsuka, S., 2002. Astrophys. J. 569 (501).
Inoue, H., 2021. PASJ 73 (795).
Inoue, H., 2022. PASJ 74 (R1).
Inutsuka, S., 2002. JCoPh 179 (238).
Islam, M.R.I., Chakraborty, S., Shaw, A., 2018. Int. J. Numer. Meth. Engng 116 (601).
Iwasaki, K., Inutsuka, S., 2011. Mon. Not. R. Astron. Soc. 418 (1668).
Jackson, J.M., Whitaker, J.S., Rathborne, J.M., Foster, J.B., Contreras, Y., Sanhueza, P., Stephens, I.W., Longmore, S.N., Allingham, D., 2019. Astrophys. J. 870 (1).
Khorasanizade, S., Sousa, J.M.M., 2016. Int. J. Numer. Meth. Eng. 106 (397).
King, A.R., Pringle, J.E., Livio, M., 2007. Mon. Not. R. Astron. Soc. 376 (1740).
Kley, W., Papaloizou, J.C.B., Lin, D.N.C., 1993.
Kolmogorov, A.A.N., 1941a. Dissipation of energy in the locally isotropic turbulence. In: Proceedings: Mathematical and Physical Science 434 N. 1890, Turbulence and Stochastic Process: Kologorov's Ideas 50 Years On. The Royal Society, London, pp. 15–17.
Kolmogorov, A.A.N., 1941b. C. R. Acad. Sci. URSS 30 (301).
Korzilius, S.P., Schilders, W.H.A., Anthonissen, M.J.H., 2017. JAMP 5 (168).
Kraichnan, R.H., 1967. PhFl 10 (1417).
Kraichnan, R.H., 1971. JFM 47 (525).
Lanzafame, G., 2003. Astron. Astrophys. 403 (593).
Lanzafame, G., 2008. PASJ 60 (259).
Lanzafame, G., 2009. AN 330 (843).
Lanzafame, G., 2010a. Mon. Not. R. Astron. Soc. 408 (1551).
Lanzafame, G., 2010b. Mon. Not. R. Astron. Soc. 408 (2336).
Lanzafame, G., 2013. CPC 184 (671).
Lanzafame, G., 2015. Int. J. Mod. Phys. D 24, 1550028.
Lanzafame, G., 2018. JComS 28 (101).
Lanzafame, G., Belvedere, G., 1998. Mon. Not. R. Astron. Soc. 295 (618).
Lanzafame, G., Belvedere, G., 2005. Astrophys. J. 632 (499).
Lanzafame, G., Belvedere, G., Molteni, D., 1992. Mon. Not. R. Astron. Soc. 258 (152).
Lanzafame, G., Belvedere, G., Molteni, D., 2006. Astron. Astrophys. 453 (1027).
Lanzafame, G., Cassaro, P., Schilliró, F., Costa, V., Belvedere, G., Zappalá, R.A., 2008. Astron. Astrophys. 482 (473).
Lanzafame, G., Molteni, D., Chakrabarti, S.K., 1998. Mon. Not. R. Astron. Soc. 299 (799).
Lastiwka, M., Quinlan, N., Basa, M., 2005. Int. J. Numer. Meth. Fluids 47 (1403).
Lattanzio, J.C., Monaghan, J.J., Pongracic, H., Schwarz, M.P., 1985. Mon. Not. R. Astron. Soc. 215 (125).
LeVeque, R.J., 1992. Numerical methods for conservation laws. In: Lectures in Matematics - ETH.
Libersky, L.D., Petschek, A.G., Carny, T.C., Hipp, J.R., Allahdadi, F.A., 1993. JCoPH 109 (67).
Liu, W.K., Jun, S., Zhang, Y.F., 1995. Int. J. Numer. Meth. Eng. 20 (1081).
Liu, M.B., Liu, G.R., 2006. Appl. Numer. Math. Eng. 56 (19).
Liu, M.B., Liu, G.R., 2010. Arch. Comput. Meth. Eng. 17 (25).
Liu, M.B., Liu, G.R., Lam, K.Y., 2003. JCoAM 155 (263).
Liu, M.B., Liu, G.R., Lam, K.Y., 2006. Sh. Wav. 15 (21).
Liu, W.T., Sun, P.N., Ming, F.R., Zhang, A.M., 2018. Acta Mech. Sinica 34 (601).
Lodato, C., Clarke, C.J., 2004. Mon. Not. R. Astron. Soc. 353 (841).
Lubow, S.H., Shu, F.H., 1975. Astrophys. J. 198 (383).
Lucy, L.B., 1977. AnJ 82 (1013).
Martí, J.M., Ibánez, J.M., Miralles, J.A., 1991. Phys. Rev. D 43 (3794).
McLelland, B.J., 1973. Statistical Thermodynamics. Chapman & Hall, London.
Meglicki, Z., Wickramasinghe, D., Bicknell, G., 1993. MNRAS 264 (691).
Miyama, S.M., Hayashi, C., Narita, S., 1984. ApJ 279 (621).
Molteni, D., Bilello, C., 2003. MmSAIS 1 (36).
Molteni, D., Lanzafame, G., Belvedere, G., 1991. Mon. Not. R. Astron. Soc. 249 (748).
Monaghan, J.J., 1985. CoPhR 3 (71).
Monaghan, J.J., 1992. ARA A 30 (543).
Monaghan, J.J., 1997. JCoPh 136 (298).
Monaghan, J.J., 2002. Mon. Not. R. Astron. Soc. 335 (843).
Monaghan, J.J., Gingold, R.A., 1983. JCoPh 52 (374).
Monaghan, J.J., Lattanzio, J.C., 1985. A A 149 (135).
Montgomery, D., Turner, L., 1981. PhFl 24 (825).
Morris, P.M., Monaghan, J.J., 1997. JCoPh 135 (41).
Motl, J.P., Frank, J., Staff, J., Clayton, G.C., Fryer, C.L., Even, W., Diehl, S., Tohline, J.E., 2017. ApJSS 229 (27).
Murray, J.R., 1996. Mon. Not. R. Astron. Soc. 279 (402).
Murray, J.R., 1998. Mon. Not. R. Astron. Soc. 297 (323).
Murray, J.R., Armitage, P.J., 1998. Mon. Not. R. Astron. Soc. 300 (561).
Nelson, R.P., Papaloizou, J.C.B., 1993. Mon. Not. R. Astron. Soc. 265 (905).
Nelson, R.P., Papaloizou, J.C.B., 1994. Mon. Not. R. Astron. Soc. 270 (1).
Okazaki, A.T., Bate, M.R., Ogilvie, G.I., Pringle, J.E., 2002. Mon. Not. R. Astron. Soc. 337 (967).
Omang, M., B/orve, S., Trulsen, J., 2005. Sh. Wav. 14 (293).
Owen, J.M., Villumsen, J.V., Shapiro, P.R., Martel, H., 1998. ApJSS 116 (155).
Paczynsky, B., 1977. Astrophys. J. 216 (822).
Papaloizou, J.C.B., Pringle, J.E., 1977. Mon. Not. R. Astron. Soc. 181 (441).
Parshikov, A.N., 1999. Comp. Math. Math. Phys. 39 (1216).
Parshikov, A.N., Medin, S.A., 2002. JCoPh 180 (358).
Parshikov, A.N., Medin, S.A., Loukashenko, I.I., Milekhin, V.A., 2000. Int. J. Impact Eng. 24 (779).
Pitaevskii, L.P., Lifshits, E.M., 1981. Course of Theoretical Physics, Vol. 10. Pergamon Press, Oxford.
Prandtl, L., 1925. Math. Mech. 5 (136).
Price, D.J., 2008. JCoPh 227 (10040).
Price, D.J., 2012. JCoPh 231 (759).
Priest, E.R., 1984. Solar Magnetohydrodynamics. Reidel Publ. Co. Dordrecht.
Pringle, J.E., 1981. ARA A 19 (137).
Quinlan, N.J., Basa, M., Lastiwka, M., 2006. Int. J. Numer. Meth. Eng. 66 (2064).
Read, J.I., Hayfield, T., 2012. Mon. Not. R. Astron. Soc. 422 (3037).
Reif, F., 1965. Fundamentals of Statistical and Thermal Physics. McGraw Hill Co, New York.
Reyes López, Y., Roose, D., Recarey Morfa, C., 2013. Comp. Mech. 51 (731).
Saitoh, T.R., Makino, J., 2013. Astrophys. J. 768 (44).
Sawada, K., Matsuda, T., Inoue, M., Hachisu, I., 1987. Mon. Not. R. Astron. Soc. 224 (307).
Schmitt, F.G., 2007. C. R. Mec. 335 (617).
Scüssler, S., Schmitt, S., 1981. Astron. Astrophys. 97 (373).
Sedov, L.I., 1946. JoAMM 10 (241).
Shakura, N.I., 1973. SvA 16 (756).
Shakura, N.I., Sunyaev, R.A., 1973. Astron. Astrophys. 24 (337).
Shapiro, P.R., Martel, H., Villumsen, J.V., Owen, J.M., 1996. ApJSS 103 (269).
Shepard, D., 1968. A two-dimensional interpolation function for irregulary-spaced data. In: ACM '68: Proceedings of the 1968 23rd ACM National Conference, ACM Proceedings. New York, pp. 517–524.
Shuangs, M., Frissane, H., Taddei, L., Lebaal, N., Roth, S., 2019. The study on instability of different kernels in solid dynamic problems by smoothed particle hydrodynamics. In: COMPDYN 2019-7th ECCOMAS Thematic Conference on Computational Methods in Structural Dynamics and Earthquake Engineering, ECCOMAS Proceedia, Crete. pp. 4675–4689.
Sibilla, S., 2015. C F 118 (148).
Siegler, S., Riffert, H., 2000. Astrophys. J. 531 (1053).
Spreng, F., Schnabel, D., Mueller, A., Eberhard, B., 2014. Comp. Part. Mech. 1 (131).
Springel, V., 2005. Mon. Not. R. Astron. Soc. 364 (1105).
Springel, V., 2010. ARA A 48 (391).
Springel, V., Hernquist, L., 2002. Mon. Not. R. Astron. Soc. 333 (649).
Spruit, H.C., Matsuda, T., Inoue, M., Sawada, K., 1987. Mon. Not. R. Astron. Soc. 229 (649).
Steinmetz, M., 1996. Mon. Not. R. Astron. Soc. 278 (1005).
Stix, M., 1989. The Sun. Springer Verlag, Berlin.
Stranex, T., Wheaton, S., 2011. Comput. Meth. Appl. Mech. Eng. 200 (392).
Sugiura, K., Inutsuka, S., 2017. JCoPH 333 (78).
Swegle, J.W., Hicks, D.L., Attaway, S.W., 1995. JCoPh 116 (123).
Taddei, L., Lebaal, N., Roth, S., 2017. CaMwA 74 (3161).
Thomas, P.A., Couchman, H.M.P., 1992. Mon. Not. R. Astron. Soc. 257 (11).
Toro, E.F., 1992. Phil. Trans. R. Soc. London Ser. A.: Phys. Sci. Eng. 338 (43).
Trampedach, R., Stein, R.F., 2011. Astrophys. J. 731 (78).
Vacondio, R., Rogers, B.D., Stansby, P.K., Mignosa, P., 2016. Comput. Methods Appl. Mech. Eng. 300 (442).
Vacondio, R., Rogers, B.D., Stansby, P.K., Mignosa, P., Feldman, J., 2013. Comput. Methods Appl. Mech. Eng. 256 (32).
Valizadeh, A., Monaghan, J.J., 2015. Eur. J. Numer. Mech. B/Fluids 51 (44).
Vaughan, G.L., 2009. Int. J. Numer. Meth. Eng. 79 (1392).
Vaughan, G.L., Healy, T.R., Bryan, K.R., Sneyd, A.D., Gorman, R.M., 2008. Int. J. Numer. Meth. Eng. 56 (37).
Vazza, F., Dolag, K., Ryu, D., Brunetti, G., Gheller, C., Hang, K., Pfrommer, C., 2011. Mon. Not. R. Astron. Soc. 418 (960).
Wang, L., Xu, F., Yang, Y., Wang, J., 2019. Eng. An. Bound. Elem. 100 (140).
Wendland, H., 1995. Adv. Comp. Mat. 4 (389).

Whitehurst, R., 1995. Mon. Not. R. Astron. Soc. 277 (655).
Wood, D., 1981. Mon. Not. R. Astron. Soc. 194 (201).
Wood, D., 1982. Mon. Not. R. Astron. Soc. 199 (331).
Yang, X.F., Peng, S.L., 2014. C F 92 (199).
Yang, X.F., Peng, S.L., Liu, M.B., 2014. Appl. Math. Mod. 38 (3822).
Zel'dovich, Y.A., Raizer, Y.P., 1966. Physics of Shock Waves and High-Temperature Phenomena. Academic Press, London.
Zhang, G.M., Batra, R.C., 2004. Comput. Mech. 34 (137).
Zhang, Z.Y., Chen, J.S., 1992. Astron. Astrophys. 261 (493).
Zhu, Q., Hernquist, L., Li, Y., 2015. Astrophys. J. 800 (1).